UTRECHT UNIVERSITY

Open heavy-flavour production in high-energy proton-proton and nucleus-nucleus collisions at CERN-LHC energies

by

Luuk Vermunt

Supervised by

dr. André Mischke

dr. Alessandro Grelli

in the

Faculty of Sciences

Institute for Subatomic Physics

August 2017

Abstract

The field of relativistic heavy-ion collisions focuses on the study of matter under extreme temperatures and/or densities. Understanding the predicted quark matter phase is a necessary step in understanding the origin of our Universe. Cross-section measurements in proton-proton collisions are, besides providing an important test for perturbative quantum chromodynamic calculations, essential as a baseline for the heavy-ion analyses. Furthermore, correlation observables hold great promise for the study of final-state radiation and the dynamical properties of the hot strongly interacting matter phase. This thesis consists of both parts: a measurement of the D^{*+}-meson invariant production cross-section with the ALICE experiment and a theoretical model study using EPOS3+HQ on a new observable based on heavy-flavour correlations.

First of all, the D^{*+}-meson production cross-section in proton-proton collisions at a centre-of-mass energy of $\sqrt{s} = 5.02$ TeV is reported. The D^{*+} meson is reconstructed in the exclusive hadronic decay channel using the invariant mass method: $D^{*+} \rightarrow D^0\pi^+ \rightarrow K^-\pi^+\pi^+$. The reconstruction was performed in the transverse momentum (p_T) range 1-24 GeV/c, using 116 million minimum-bias events. A heavy-flavour enriched Monte-Carlo sample was used to compare the results and extract the reconstruction efficiencies. The p_T-differential cross-sections are compared with Fixed Order plus Next-to-Leading Logarithm calculations. The overall production is well described, however, the data is on the higher side of the theoretical uncertainty band. The results were approved by the ALICE Collaboration as preliminary results for the Quark Matter conference in 2017.

The influence of final-state radiation of heavy quarks in high-energy proton-proton collisions is studied using a new proposed transverse momentum correlation observable. The transverse momentum correlation of D and $\overline{D}$ mesons, which have been emitted with an azimuthal difference angle close to 180 degrees, is identified as an observable which is sensitive to the final-state radiation. This is demonstrated performing calculations with the event generator Pythia 6 and the EPOS3+HQ model. The initial symmetric $p_T = p_T{}'$ correlation in proton-proton collisions is not completely vanished, neither for the final $D\overline{D}$ nor for the $c\bar{c}$ and $b\bar{b}$ before hadronisation. Also a difference in the shape of the distribution for EPOS3+HQ and Pythia 6 is found. The use of the new observable to differentiate between collisional and collisional+radiative in-medium energy loss mechanisms in Pb-Pb collisions is limited. Different centrality classes have been studied, but no significant difference in the distribution for both energy loss mechanisms was found. The work for this part of the thesis has been done during an internship for three months at Subatech in Nantes. The results of this theoretical study are presented in a paper, which will be submitted soon.

Contents

Chapter 1

Introduction

In this thesis, an experimental and a theoretical study on open heavy-flavour production in high-energy proton-proton and nucleus-nucleus collisions are presented. Heavy-flavour production is a good probe to study a new phase of matter, the so-called quark-gluon plasma, predicted by the theory of strong interaction. This phase transition is expected to occur at extremely high temperatures and/or high densities. It is therefore believed that the Early Universe and the inner part of neutron stars consist of this phase of matter. One way to study this state experimentally is by colliding heavy-ions in particle accelerators at relativistic energies.

In the first part of this thesis, a measurement of the invariant cross-section of D^{*+} mesons is performed in the QGP-ALICE group of dr. André Mischke at Utrecht University. This group focuses on the measurement of heavy-flavour production in collisions of high energetic atomic nuclei in the ALICE experiment at the CERN Large Hadron Collider. A good collaboration exists between this group and the High-Energy Theory group of Subatech in Nantes, lead by Prof. dr. Pol-Bernard Gossiaux. The second part of this thesis was performed there, during an internship of three months. The results for this theoretical study, following from a newly proposed transverse momentum correlation observable for heavy quarks, will be published soon.

The D^{*+}-meson cross-section measurement in proton-proton collisions is important, as it is performed at the same energy as the LHC heavy-ion data. So besides putting constraints on theoretical model calculations, it will also function as a baseline for measurements in heavy-ion collisions. The theoretical model study will be very interesting in the near future, when correlation measurements will become feasible in the LHC experiments. Transverse momentum correlation measurements hold great promise for studying the dynamical properties of the quark-gluon plasma.

First, a brief theoretical introduction will be given in Chapter 2. In Chapter 3, the experimental part of this thesis is described. The invariant cross-section of D^{*+} mesons in pp collisions at $\sqrt{s} = 5.02$ TeV is measured with the ALICE detector. The full analysis, starting from the ALICE detector itself, to the final systematic uncertainties on the measurement will be presented. The results have been accepted by the ALICE Collaboration as preliminary results for the Quark Matter 2017 conference. In Chapter 4, a theoretical study with the EPOS3+HQ model is discussed. A new transverse momentum correlation observable is proposed that will be sensitive to final-state radiation and in-medium energy loss models. A conclusion and outlook are given in Chapter 5.

Chapter 2

Theoretical background

In the search for the fundamental degrees of freedom of matter, numerous new particles have been found at particle colliders in the last decades. These particles, and additionally three of their four interaction mechanisms, are described by the Standard Model of particle physics. This model includes the electromagnetic, weak and strong force and uses the Higgs mechanism to explain the masses of the particles. Although the Standard Model is known to be incomplete[1], no significant deviations have been found so far at particle colliders like the Large Hadron Collider. On the contrary, the Standard Model has demonstrated to be very successful in providing experimental predictions, like the Higgs Boson [1, 2].

In this thesis, we are interested in the strong interaction of the Standard Model, which is discussed in detail in section 2.1. This interaction is the least understood of the four, but has very interesting properties. One of them is the prediction of a quark-gluon plasma (QGP), which is a hot and dense state of matter with (quasi-)free partons (quarks and gluons). It is believed that the Early Universe consisted of this state of matter a few microseconds after the Big Bang. A more detailed description of the QGP is given in section 2.2. In the last section of this chapter, the use of heavy quarks in the study of the QGP is explained. Heavy-flavour observables are very good probes to study the quark-gluon plasma. This is the case for current measurements, as is shown in Chapter 3, but also for new measurements that will become feasible in the future, see Chapter 4.

In this chapter, a general theoretical background is given. For the second part of this thesis, a theoretical study into heavy-flavour correlation observables, a more detailed theoretical introduction is needed. This will be given in Chapter 4.

2.1 Quantum Chromodynamics

Quantum Chromodynamics (QCD) is the quantum field theory that describes the strong interaction between partons [3]. Partons can be quarks or gluons and are carrying a colour charge (red, blue, green or their respective anticolours). QCD is based on the gauge invariance of these colour charged particles. So, if all colours in a system are

[1]The Standard Model does not include the gravitational force, dark matter and dark energy and can not provide an explanation for several issues like the matter-antimatter asymmetry.

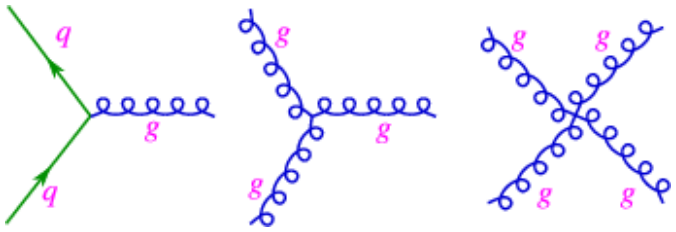

FIGURE 2.1: The fundamental interaction vertices in Quantum Chromodynamics. Note that the direction of time and space are not specified in these diagrams.

simultaneously changed, the interactions will still be the same. Such transformations are expressed as:

$$\psi_k \to \psi'_j = \exp[i\, g_s\, \alpha_a\, T^a_{jk}]\, \psi^k, \tag{2.1}$$

where T^a_{jk} are the eight generators of the SU(3) transformation, α_a the corresponding complex fields and g_s the coupling strength. The QCD Lagrangian, which obviously has to be invariant under these rotations, is given by

$$\mathcal{L}_{\text{QCD}} = \bar{\psi}\,(i\gamma^\mu\,(\partial_\mu - ig_s A^a_\mu T_a) - m)\,\psi - \frac{1}{4} F^a_{\mu\nu} F^{\mu\nu}_a. \tag{2.2}$$

Here, A^μ_a is the gluon field and $F^a_{\mu\nu}$ a fully gluonic tensor. See Ref. [4] for a detailed description of the QCD Lagrangian. The first term of equation 2.2 is similar as in the Quantum Electrodynamics gauge theory (QED), and produces vertices with two quarks and one gluon (e.g. gluon splitting or gluon radiation). The last term of equation 2.2 gives rise to three- or four-gluonic interaction vertices, as the tensor is given by:

$$F^{\mu\nu}_a = \partial^\mu A^\nu_a - \partial^\nu A^\mu_a - g_s f^{bc}_a A^\mu_b A^\nu_c\,. \tag{2.3}$$

Here, f^{bc}_a are the structure constants of the SU(3) symmetry group. The final interactions are schematically described using Feynman diagrams in Figure 2.1.

The gluon self-interaction gives rise to a strong confinement force between partons. It is therefore that quarks always appear in bound states, called hadrons. It is not possible to measure an individual parton directly. On the other hand, hadrons can be measured in colliders like the LHC. There are two types of hadrons: baryons, consisting out of three (anti)quarks, and mesons, consisting out of a quark and an antiquark. The confinement force that holds these quarks together can be approximated, at large distances, by a potential that rises linear with the distance between the partons. This increase ensures that a new quark-antiquark pair will be created, instead of the "existence" of a free quark. For small distances, the force can be described with a Coulomb potential.

The coupling constant g_s is, after renormalisation, given by $\alpha_s = g_s^2/4\pi$. Despite the name, this coupling is not constant. It reaches very large scales in interactions between partons of small momentum scales. In a first-order approximation, this momentum dependence is given by

$$\alpha_s \propto 1/\ln \frac{Q^2}{\Lambda^2_{\text{QCD}}}. \tag{2.4}$$

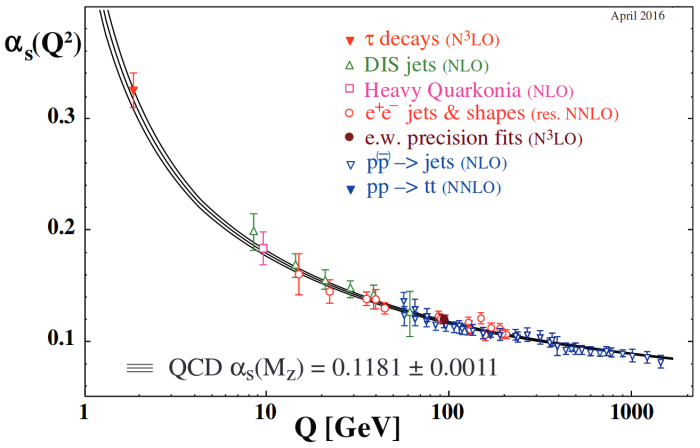

FIGURE 2.2: Theoretical predictions and experimental measurements of the strong running coupling constant α_s as a function of the momentum transfer Q. Figure taken from [5].

Experimental measurements of the coupling constant are shown in Figure 2.2. Both in theoretical and experimental results, one observes an asymptotic behavior $\alpha_s \to 0$ for $Q \to \infty$, which is called asymptotic freedom.

For processes involving partons at large momentum, α_s will be small enough for a perturbative treatment of Quantum Chromodynamics (pQCD). In this treatment, the calculations of squared matrix elements are expanded into perturbative series of α_s. The lower orders in α_s will be the leading ones, and higher orders can be neglected. An often used pQCD calculation is the FONLL calculation (Fixed Order plus Next-to-Leading Logarithm) [6]. This theory combines next-to-leading order calculations and next-to-leading logarithmic resummation to calculate cross-sections of heavy-flavour quarks or mesons in proton-proton collisions. Uncertainties of the calculation are estimated by varying the masses, scaling, particle density functions, renormalisation and factorisation scales. In this thesis, a web interface to calculate FONLL predictions was used [7]. In the heavy-flavour community, GM-VFNS (General Mass Variable Flavour Number Scheme) [8, 9] is another often used perturbative calculation of the production cross-sections.

2.2 The Quark-Gluon Plasma

Asymptotic freedom, as presented in the previous section, motivates the question if it is possible to measure (quasi-)free partons. To answer this question, the phase-diagram of QCD has been studied for several decades (see Figure 2.3). It is now believed that at extremely high temperatures and/or densities, a phase transition to a new state of matter occurs. In this new phase, partons are deconfined and can move freely over larger distances than the typical scale of a hadron. Only in-medium interactions will perturb the path of the parton. This medium is called a quark-gluon plasma.

As one can see in Figure 2.3, a QGP can exists in systems with an extremely high temperature and/or baryon chemical potential μ, which scales with the density of a system. So ultra-dense systems, like the core of a neutron star, or extremely hot systems, like the Early Universe a few microseconds after the Big Bang, are expected to consist

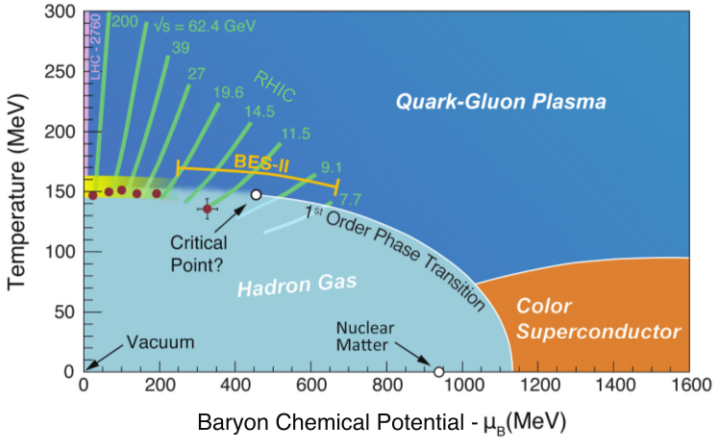

FIGURE 2.3: Lattice QCD calculations of the phase diagram of the strong interaction. The red circles indicate measurements of the freeze-out curve at the LHC and RHIC. Figure is taken from [13].

out of a quark-gluon plasma. This state of matter can be created in heavy-ion collisions in the laboratory. At the LHC, signs of a QGP have also been observed in smaller systems like p-Pb and even in pp collisions [10–12]. It is, however, highly debated if these observations are due to a plasma phase.

As the lifetime of a quark-gluon plasma is extremely short (a few fm/c), it can not be measured directly. When the system expands, the temperature and density decrease and the QGP will decay in multiple hadrons that can be detected. Besides indirect signs, like increased strangeness production and elliptic flow, there is no direct proof of the quark-gluon plasma, although it is predicted by numerical solutions of QCD [14].

2.3 Heavy quarks

There are several reasons why heavy quarks (charm and beauty) are good probes to study the QGP. First of all, because they are colour charged particles, they interact with medium particles. Secondly, due to their large masses, they are most likely to be pair-produced in the early stage pQCD processes. This means that the heavy quarks are produced before the quark-gluon plasma. Additionally, heavy quarks live much longer than the QGP, so they pass through the entire medium and therefore experience the full evolution of the system. As the temperature of the medium is much smaller than the heavy quark masses, secondary production of heavy-flavour quark pairs by the medium can be neglected.

As is shown in Figure 2.4, the heavy-quark masses are almost exclusively generated by the Higgs mechanisms, while for the light quarks (up, down and strange) the spontaneous breaking of the chiral symmetry in QCD is dominant. As it is believed that the chiral symmetry is restored in a quark-gluon plasma [15], heavy-flavour quarks remain heavy. The light quarks will interact with their bare current masses. In short, this means that the heavy quarks are less likely to thermalise with the medium than light quarks[2].

[2]Thermalisation with the medium means losing too much initial information so they become indistinguishable from medium particles.

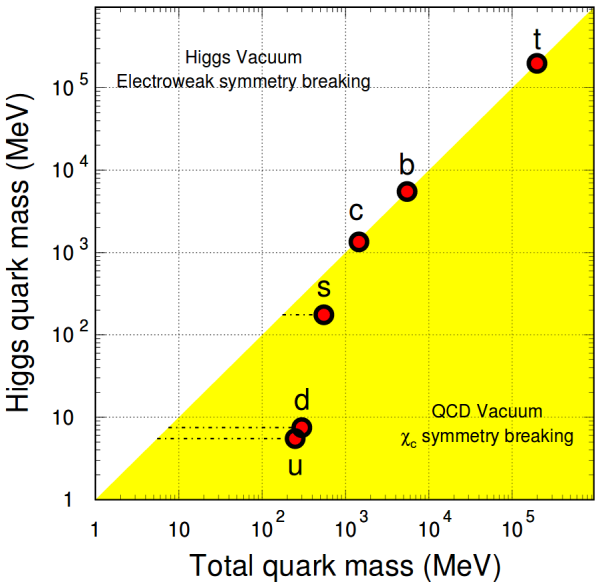

FIGURE 2.4: Quark masses in the QCD and Higgs vacuum. The light quark masses are mostly generated due to chiral symmetry breaking, which might be restored in a quark-gluon plasma. Figure taken from [15].

2.3.1 Heavy-flavour observables

Heavy quarks that pass through a quark-gluon plasma will interact with the medium particles and loose part of their energy. This suppression can be quantified using the so-called nuclear modification factor

$$R_{\mathrm{AA}} = \frac{\mathrm{d}N_{\mathrm{AA}}/\mathrm{d}p_{\mathrm{T}}}{\langle T_{\mathrm{AA}} \rangle \cdot \mathrm{d}\sigma_{\mathrm{pp}}/\mathrm{d}p_{\mathrm{T}}}, \tag{2.5}$$

where $\langle T_{\mathrm{AA}} \rangle$ is the average nuclear overlap function, $\mathrm{d}\sigma_{\mathrm{pp}}/\mathrm{d}p_{\mathrm{T}}$ the differential cross-section in pp collisions and $\mathrm{d}N_{\mathrm{AA}}/\mathrm{d}p_{\mathrm{T}}$ the yield in heavy-ion collisions. So, the properties of heavy quarks in proton-proton collisions are used as a reference. An example of the R_{AA} measured by ALICE in Pb-Pb collisions at $\sqrt{s_{\mathrm{NN}}} = 2.76$ TeV is illustrated in the left panel of Figure 2.5 [16]. A significant in-medium energy loss of charm quarks is observed. The CMS experiment measured the nuclear modification factor for beauty mesons (see Ref. [17]) and also there a R_{AA} smaller than one is observed. Note that cold nuclear matter effects, such as the Cronin effect [18], can enhance the number of heavy quarks, so that $R_{\mathrm{AA}} > 1$ is physically possible.

The elliptic flow of heavy quarks is another interesting observable often measured in the LHC experiments. Because most of the time, the nuclei do not hit each other head-on, the QGP medium does not have to be spherical. For peripheral collisions, the system will have an almond-shape and experience spatial anisotropy. As heavy quarks are produced before the quark-gluon plasma is formed, it can be expected that this spatial anisotropy reflects itself in the final momenta. This can be shown experimentally using the elliptic flow parameter v_2 (see right panel Figure 2.5 for an example [19]). Besides hinting to partially thermalised charm quarks with the medium, these measurements can also be used to differentiate between different in-medium energy loss mechanisms.

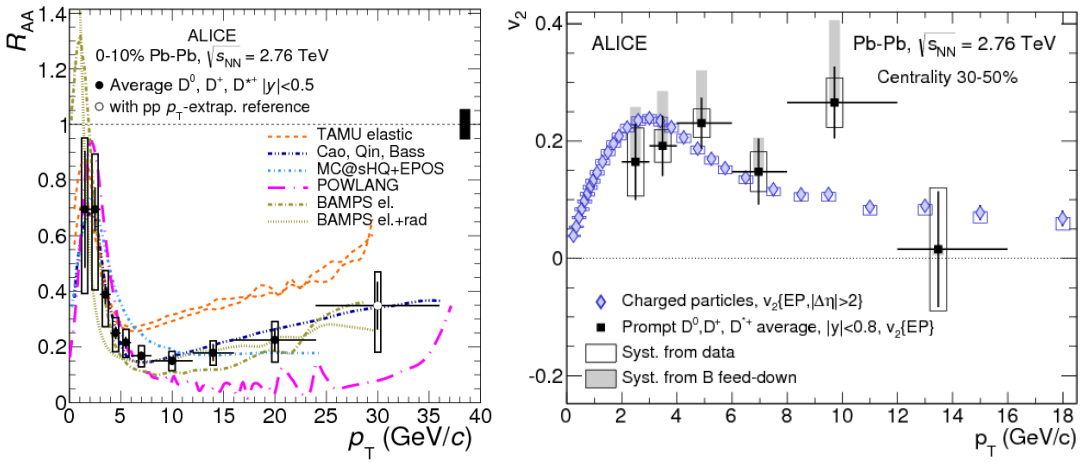

FIGURE 2.5: Left: Average of prompt D^0, D^+ and D^{*+}-meson R_{AA} as measured by the ALICE experiment in centrality class 0-10% at $\sqrt{s_{NN}} = 2.76$ TeV [16]. Right: Average of D^0, D^+ and D^{*+}-meson v_2 as a function of p_T in centrality class 30-50% as measured by the ALICE experiment at $\sqrt{s_{NN}} = 2.76$ TeV [19].

At the moment, it is yet unclear through what mechanisms heavy quarks lose their energy in a QGP, which can be purely collisional or collisional+radiative. For a purely collisional energy loss mechanism, a heavy quark experiences a lot of low energetic interactions with the medium constituents. The radiative energy loss mechanism characterises itself with only a few, but energetic, interactions. Collisional energy loss also depends linearly on the in-medium path-length, where the dependence is quadratic for radiative processes [20]. Up to now, measurements of the R_{AA} and v_2 have not been able to answer this open question.

With the upcoming detector upgrades of the ALICE [21] and CMS experiments [22], correlation measurements of heavy quarks in Pb-Pb collisions may become feasible. These measurements, as discussed during the Lorentz workshop 2016 in Leiden [23], hold great promise to provide a distinguishing measurement. Especially, momentum correlation measurements of heavy quarks are of great interest [24–26]. At this moment, there are only a few heavy-flavour correlation measurements available in pp collisions and most of them cannot be reproduced by state-of-the-art event generators like Pythia or Herwig (see for example Ref. [27]). Therefore, besides experimental upgrades, also improvements of the modelling approaches are needed. This will be the subject of the theoretical study discussed in Chapter 4.

Chapter 3

D^{*+}-meson cross-section measurement in ALICE

In this chapter, the cross-section measurement of the D^{*+} meson in proton-proton collisions at $\sqrt{s} = 5.02$ TeV in the ALICE detector will be discussed. The D^{*+} meson is a heavy-flavour meson consisting of a charm and an antidown quark. The fully hadronic decay channel $D^{*+} \rightarrow D^0\pi^+ \rightarrow K^-\pi^+\pi^+$ is used to reconstruct the D^{*+} meson. The measured cross-section has been compared to perturbative QCD FONLL calculations. The results presented here have been accepted as preliminary by the ALICE experiment for the Quark Matter conference 2017 in Chicago.

In the previous chapter, the importance of heavy quarks in the study of the QGP was already discussed. Besides Pb-Pb and p-Pb collisions, the ALICE experiment also studies heavy-flavour production in proton-proton collisions. These charm production cross-section measurements in proton-proton collisions are essential as baseline for the heavy-ion analyses. In addition, these measurements are also an important test for perturbative QCD calculations. At low p_{T}, where the theoretical uncertainties are still relatively large, heavy-flavour production is dominated by low-x gluons. So, measurements in this region can provide necessary constraints on the pQCD calculations.

First, a general overview of the ALICE experiment and detector will be given, where only the subdetectors used for this analysis will be described in detail. In section 3.2, the used data and the corresponding Monte-Carlo (MC) samples will be discussed. For the latter sample, some of the important quality assurance checks will also be shown. In section 3.3, the reconstruction strategy is outlined. The final results are presented in section 3.4, where the study of the systematic uncertainties is presented in section 3.5.

3.1 Experimental setup

3.1.1 The ALICE detector

At CERN, the European Organization for Nuclear Research in Geneva, the Large Hadron Collider (LHC) is located. This 27 km long particle accelerator houses the detectors of the ATLAS, CMS, LHCb and ALICE experiments. The ALICE (A Large Ion Collider

Experiment) detector is the only detector specifically designed to study heavy-ion collisions. In Figure 3.1, the detector and its subdetectors are schematically shown. This 10,000 tons weighing detector consists roughly out of the central barrel ($|\eta| < 0.9$) and the forward muon spectrometer. The most important subdetectors for the measurement of D mesons are all located in the central barrel and will be discussed in the following subsections. The ALICE apparatus is described in detail in Ref. [28].

3.1.1.1 Inner Tracking System

The detector closest to the interaction point is the Inner Tracking System (ITS), which is a cylindrically-shaped silicon detector with a pseudorapidity coverage of $|\eta| < 0.9$. It is a very important detector for short-living particles, which are the interest of this analysis. Using the ITS, prompt particles can be distinguished from particles coming from decays of particles with a short lifetime. Besides this, the ITS detector plays an important role in identifying and tracking of low momentum particles. It also improves the momentum and angle measurements of the Time Projection Chamber.

The ITS consists of six layers of silicon detectors located at radii between 3.9 and 43 cm from the beamline (see inset Figure 3.1). The two innermost layers are Silicon Pixel Detectors (SPD). Pixel detectors have a very high spatial resolution, which allow to reconstruct the primary vertices with high precision. The two intermediate layers are Silicon Drift Detectors (SDD) and the two outermost layers are equipped with double-sided Silicon Strip Detectors (SSD). The SDD detectors give information about the two-dimensional positions, where the SSD layers are essential to make the connection with tracks in the TPC. The outermost four layers also allow for particle identification by measuring the specific ionisation energy loss $\mathrm{d}E/\mathrm{d}x$.

In the second long shutdown of the LHC, ALICE will install a new Inner Tracking System [21]. Because it will have an additional layer closer to the collision point and in general a higher resolution, the new ITS will allow for better vertexing and tracking of particles. This is an important upgrade for the second part of this thesis, where a theoretical study into heavy-flavour correlation measurements is performed. With this upgrade, such measurements will become feasible in the ALICE experiment.

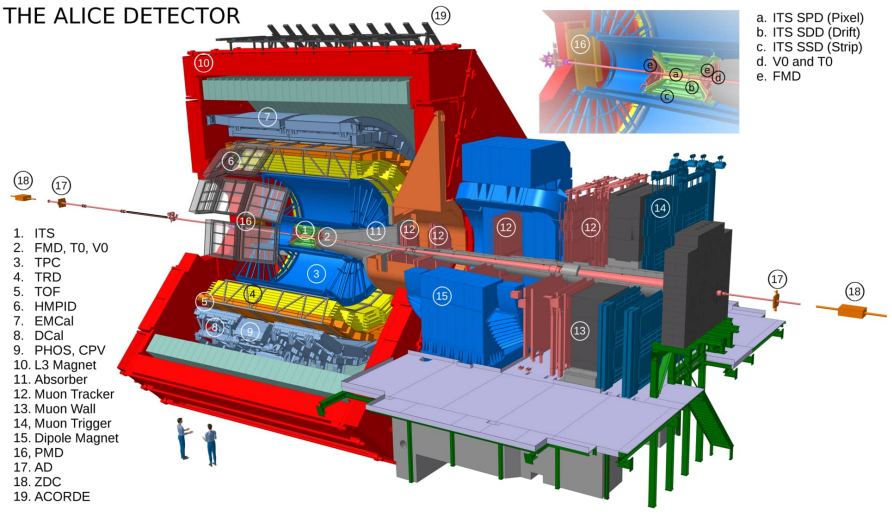

FIGURE 3.1: Schematic 3D view of the ALICE detector in LHC Run-2 [29].

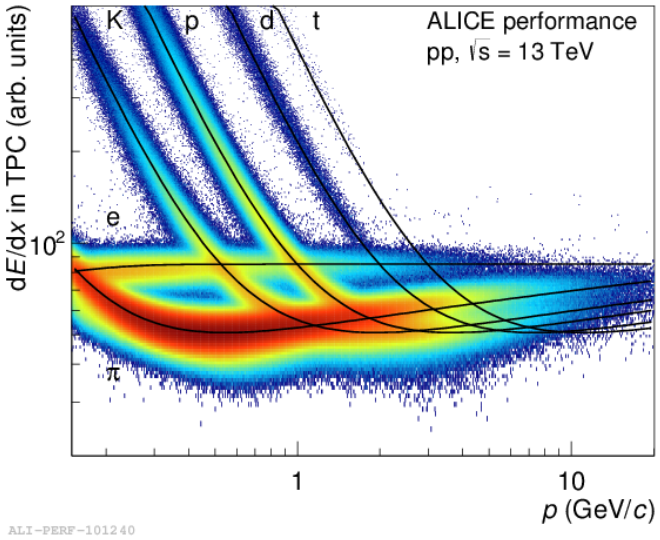

FIGURE 3.2: The dE/dx particle identification performance by the TPC in the LHC Run-2 for proton-proton collisions. Note that this figure shows the performance at 13 TeV, as for this data sample the statistics are better [31].

3.1.1.2 Time Projection Chamber

The cylindrical Time Projection Chamber (TPC) that surrounds the ITS detector (at radii $85 < r < 247$ cm) is the main tracking device of the ALICE detector [30]. It is filled with a Ne/CO_2 gas mixture ($90 : 10$) that ionises when charged particles are passing the chamber. The ions and removed electrons are attracted by an electric field of 400 V/cm along the beam direction, after which the specific energy loss is measured in multi wire readout chambers. The amount of lost energy per distance for a given momentum is used to identify charged particles as is illustrated in Figure 3.2. The point of impact and the difference in arrival time on the two ends of the detector lead to the reconstruction of a track. The TPC can have a maximum of 159 three-dimensional space points per track and has an acceptance of $|\eta| < 0.9$.

3.1.1.3 Time Of Flight detector

The particle identification capability of the TPC is complemented by the Time Of Flight (TOF) detector, which covers the full azimuthal angle, has an acceptance of $|\eta| < 0.9$ and is positioned at radii of 377 to 399 cm. It consists out of 1638 Multi-gap Resistive Plate Chambers (MRPCs). Using the event start time information from other detectors, the TOF detector can determine the time of flight of a particle. This information, combined with the momentum hypothesis, results in an estimate of the particles mass, which is used for particle identification. The TOF is optimised for charged particles with momentum below 2.5 GeV/c (which is the case for the final-state particles used in this analysis), where for particles with larger momentum the High Momentum Particle Identification (HMPID) detector is used. The time resolution in the TOF detector is approximately 80 ps, which provides a 3σ separation between pions and kaons up to 2.2 GeV/c as can be seen in Figure 3.3.

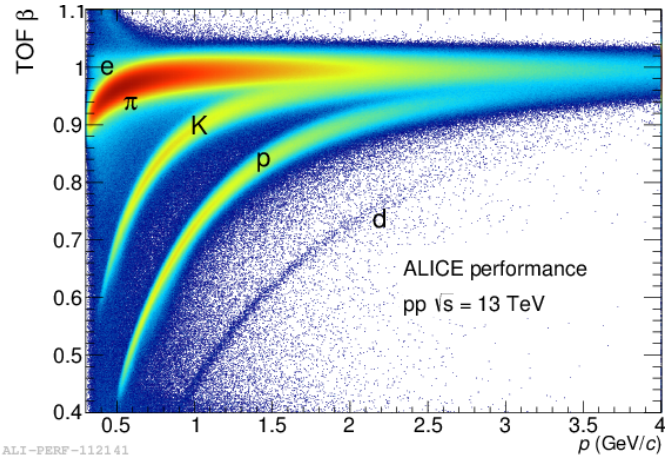

FIGURE 3.3: The $\beta = v/c$ versus p particle identification performance by the TOF detector in LHC Run-2 for proton-proton collisions. Note that this figure shows the performance at 13 TeV, as for this data sample the statistics are better [31].

3.1.1.4 VZERO detector

Because the bunches of protons in the LHC collide every 25 ns, the electronics of the ALICE experiment are not capable of saving each event, so triggers are used for event selection. The minimum-bias collisions of the pp reference run in 2015 used for this analysis, were triggered by the so-called kINT7 trigger. It is triggered when both sides of the VZERO detector measure a signal above a certain threshold. This detector consists out of two separate arrays. The VZERO-A array is located at $z = 328$ cm covering $2.8 < \eta < 5.1$, and the VZERO-C array at $z = -86$ cm covering $-3.7 < \eta < -1.7$. The VZERO systems consist out of two disks of plastic scintillator hodoscopes divided into 4 rings with 8 segments.

3.1.2 Analysis framework

The analysis framework used by ALICE is called AliRoot, which is used for all physical analyses but also for the reconstruction of an event. This framework is called "off-line", where the measurements and event selection in the previous discussed sections is referred to as "on-line". AliRoot is based on ROOT [32] and GEANT [33]. ROOT is a software framework that is specifically designed to analyse data obtained at particle colliders, but is nowadays also used in different fields of research. The software package GEANT is a transport code that simulates the interaction between particles and different kind of matter. Because AliRoot contains the full construction of the detector, GEANT can be used to simulate the detector responses when particles travel through the detector.

The macros used for all the different analyses performed in ALICE are saved in the AliPhysics Git master branch. The here presented results are based on the PWG-HF code. For example, the D^{*+} mass spectra are obtained using the task AliAnalysisTaskSEDStarSpectra, where the selection cuts and particle identification are performed using the class AliRDHFCutsDStartoKpipi.

3.2 Data and Monte-Carlo samples

For this analysis, the pp collisions at $\sqrt{s} = 5.02$ TeV collected in November 2015 by the ALICE experiment are studied. This run consists only of five days of data taking, but is nevertheless important because it is a reference run for the heavy-ion runs. Hence, it was performed at the same energy as the p-Pb (LHC Run-1 and 2) and Pb-Pb (LHC Run-2) runs. Where up to now, the 7 TeV pp run was extrapolated to 5.02 TeV to function as baseline, this measurement can be used directly. As this extrapolating procedure will, by definition, enlarge the uncertainties of the 7 TeV measurement, it is better to use the reference run. However, because the timeline for Quark Matter 2017 was too tight, the heavy-ion preliminaries were still using the extrapolated 7 TeV cross-section. In the future, the aim is to use this measurement as a baseline. Especially, in combination with the additional "long pp reference run" scheduled in 2017.

3.2.1 Data sample

In this analysis, the minimum-bias triggered data of sample LHC15n pass2 is used. The AODs (Analysis Object Data)[1] were produced using AliRoot v5-08-13e-1 and AliPhysics v5-08-13e-01-1. After quality assurance checks in August 2016, the Data Preparation Group (DPG) published the following good runlist for LHC15n:

- 244628, 244627, 244626, 244619, 244618, 244617, 244542, 244540, 244531, 244484, 244483, 244482, 244481, 244480, 244456, 244453, 244421, 244416, 244377, 244364, 244359, 244355, 244351, 244343, 244340.

So, in total 25 runs were used for this analysis that correspond to 116 million minimum-bias events.

A general physics selection procedure on the AOD events is applied. The primary vertex, which has to be reconstructed using ITS+TPC tracks, needs to have a z coordinate in the range $|z| < 10$ cm. The kINT7 trigger selection was also used off-line to reject beam and background events.

3.2.2 Monte-Carlo sample

The Monte-Carlo (MC) production LHC16i6a is anchored to the LHC15n pass2 data sample. Besides for optimisation and checks of the analysis, this MC sample is necessary to compute the efficiency corrections. By anchoring to each run of LHC15n, one makes sure that data and MC have the same conditions. This MC sample is heavy-flavour enriched, so each pp event was required to contain a $c\bar{c}$ or $b\bar{b}$ pair. The produced D mesons were forced to decay hadronically, to gain statistics.

The MB pp collisions in LHC16i6a, were produced with the event generator Pythia 6 [34] with the Perugia-2011 tuning [35]. The AODs were produced using AliRoot v5-08-13o-1 and AliPhysics v5-08-13o-01-1. The run numbers used for the MC are the same as stated above for the LHC15n sample, which correspond to approximate 3.2 million events.

[1] The final data on which the analysis is performed.

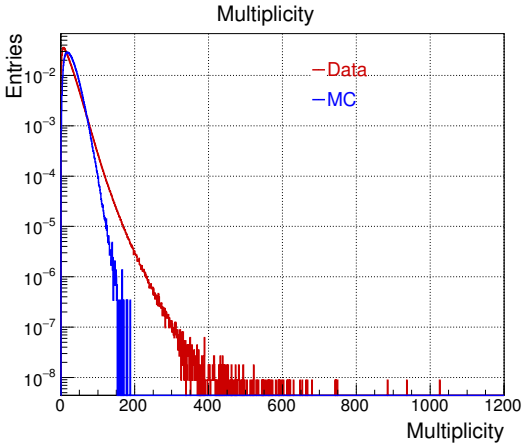

FIGURE 3.4: Multiplicity distribution for period LHC15n and the anchored LHC16i6a Monte-Carlo sample with heavy-flavour enrichment.

3.2.2.1 Quality assurance

In the remaining of this section, some of the performed quality assurance checks of this MC sample will be shown. Also the fundamental distributions between data and MC are reported. These quality assurance checks are similar for each D meson, as the D^{*+} meson adopts the same selection procedure as the D^0 and D^+ mesons. All mesons utilise a similar secondary vertex strategy and use the same topological variables. Therefore, it was chosen to use the D^+ filtering cuts. As a quality assurance consists out of many checks, only a few plots will be shown here. All the relevant plots can be found in Refs. [36] and [37].

In Figure 3.4, the multiplicity distribution for both data and MC is shown. A difference in both distributions is observed, but this is expected due to the heavy-flavour enrichment of the MC sample. A factor of two difference in the tail was also observed in previous simulations [38]. As this analysis is multiplicity integrated, a proper correction is not needed.

The number of "Good daughter tracks per event" and the number of "Selected tracks per event" are shown in Figure 3.5. These interesting observables display respectively the number of tracks that pass some basic track selection and the number of tracks that pass the full D^+-meson selection. Again, a difference in both distribution is found, originating from the same heavy-flavour enrichment of the MC. The difference is, however, smaller as for the multiplicity and is reduced when the full selection is applied.

The ϕ distribution of the daughter tracks is shown in Figure 3.6. Just like for the η and vertex position distributions (not shown here), data and MC are compatible. Finally, one example of the particle identification quality assurance is shown in Figure 3.7, where the TPC PID estimator for pions is presented for data and MC. The average, expected to be zero, is drawn in black, where the standard deviation, drawn in red, is expected to be one.

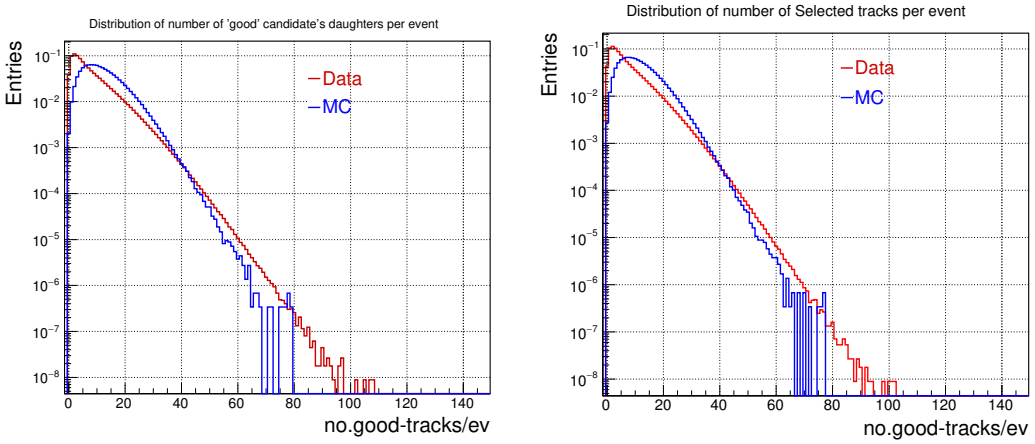

FIGURE 3.5: Distribution of the number of "Good daughter tracks per event" (left) and the number of "Selected tracks per event" (right) for period LHC15n and the anchored LHC16i6a Monte-Carlo sample.

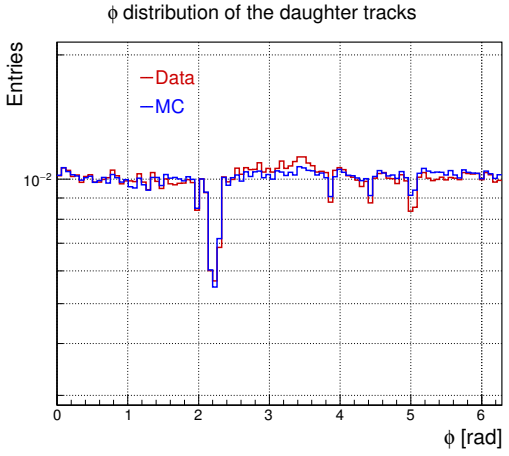

FIGURE 3.6: ϕ distribution of the daughter tracks for period LHC15n and the anchored LHC16i6a Monte-Carlo sample.

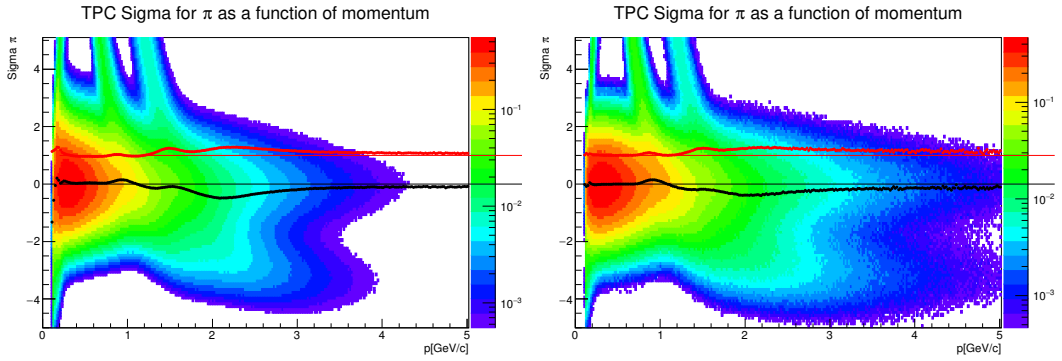

FIGURE 3.7: TPC PID estimator as a function of momentum for pions for period LHC15n (left) and the anchored LHC16i6a Monte-Carlo sample (right).

3.3 D^{*+}-meson reconstruction

The D^{*+} mesons, as well as their antiparticles, were reconstructed in the central rapidity region in the charged hadronic decay channel $D^{*+} \to D^0\pi^+ \to K^-\pi^+\pi^+$ with a branching ratio (BR) of 2.66 ± 0.03 % [5]. An invariant mass analysis of fully reconstructed decay topologies was used to extract the D^{*+}-meson yields in different transverse momentum bins. Because the D^{*+} meson decays strongly at the primary vertex, D^0 candidates were attached to $\pi^{\pm}$ candidate tracks at the primary vertex. To reconstruct the D^0 candidates, the decay topology displacement with respect to the primary vertex was employed.

To enhance the signal-to-background ratio, p_{T} dependent topological and kinematic selection cuts are applied on the final decay products of both the D^{*+} and D^0 mesons. Further background rejection is obtained with particle identification (PID) in the TPC and TOF detectors.

Secondary vertices of D-meson candidates were reconstructed using tracks having $\eta < |0.8|$, $p_{\mathrm{T}} > 0.3$ GeV/c, at least 70 points (out of a maximum of 159) associated space points and a $\chi^2/\mathrm{ndf} < 2$ in the TPC, and a ratio of crossed rows over findable clusters in the TPC larger than 0.8. At least one associated hit in either of the two pixel layers is also required. These track selection criteria reduce the D meson acceptance, which drops steeply to zero for $|y_{\mathrm{lab}}| > 0.5$ at low p_{T} and for $|y_{\mathrm{lab}}| > 0.8$ at $p_{\mathrm{T}} > 5$ GeV/c. A p_{T}-dependent fiducial acceptance region was therefore defined as $|y_{\mathrm{lab}}| < y_{\mathrm{fid}}(p_{\mathrm{T}})$, with $y_{\mathrm{fid}}(p_{\mathrm{T}})$ increasing from 0.5 to 0.8 in the transverse momentum range $p_{\mathrm{T}} < 5$ GeV/c according to a second-order polynomial function, and $y_{\mathrm{fid}} = 0.8$ for $p_{\mathrm{T}} > 5$ GeV/c.

3.3.1 Topological selection

To reconstruct the D^{*+} mesons, topological selection of the reconstructed candidates is needed to reduce the large combinatorial background. For each reconstructed candidate, several cut variables are computed using the primary and secondary vertex positions and the kinematics of the decay tracks.

The base of the selection cuts for the D^{*+} meson are the values used in the 7 TeV pass4 pp analysis. These values have been optimised for the 5.02 TeV sample using the true D^{*+}-meson distributions from the heavy-flavour enriched LHC16i6a sample compared with background D^{*+} candidates from the minimum-bias LHC10f6a sample. By making Receiver Operating Characteristic (ROC) curves, so plotting the signal selection efficiency versus the background rejection efficiency, the values of all cut variables were checked and optimised if needed. Additionally, the three most effective cuts were varied using the AliAnalysisTaskSESignificance task: the distance of closest approach (DCA), the cosine of the pointing angle between the D^0 flight line and the reconstructed D^0 momentum ($\cos\theta_{\,\mathrm{point}}$) and the product of impact parameters from the kaon and pion ($d_0^K \cdot d_0^{\pi}$). This task uses a multidimensional approach to optimise the cuts to obtain the highest significance in a given range. The final applied selection cuts for the D^{*+} meson are shown in Table 3.1.

As discussed in section 3.1, the TPC and TOF detector can separate kaons and pions from all other particle species in different momentum ranges. The energy loss deposited in the Time Projection Chamber and the velocity measurements in the Time Of Flight

p_{T} [GeV/c]	[1,2]	[2,3]	[3,4]	[4,5]	[5,6]	[6,7]	[7,8]	[8,10]	[10-12]	[12,16]	[16,24]
Inv. Mass D^0 [GeV/c^2]	0.035	0.035	0.035	0.038	0.038	0.04	0.04	0.045	0.045	0.05	0.07
DCA [cm]	0.04	0.034	0.04	0.1	0.1	0.1	0.1	0.1	0.1	0.1	0.5
$\cos\theta^*$	0.9	0.9	1	1	1	1	1	1	1	1	1
p_{T} K [GeV/c]	0.5	0.7	0.8	0.9	1	1	1	1	1	0.3	0.3
p_{T} π [GeV/c]	0.5	0.7	0.8	0.9	1	1	1	1	1	0.3	0.3
d_0 K [cm]	0.1	0.1	0.1	0.1	0.1	0.1	0.1	0.1	0.1	0.15	0.15
d_0 π [cm]	0.1	0.1	0.1	0.1	0.1	0.1	0.1	0.1	0.1	0.15	0.15
$d_0^K \cdot d_0^\pi$ [cm^2]	-6.56e-05	-0.000172	-5.7e-05	-1.6e-05	0.0004	0.001	0.001	0.006	0.006	0.01	0.01
$\cos\theta_{point}$	0.7	0.7	0.9	0.9	0.82	0.74	0.72	0.55	0.55	0.65	0.55
Inv. Mass half width D^{*+} [GeV/c^2]	0.3	0.3	0.3	0.3	0.3	0.3	0.3	0.3	0.3	0.3	0.3
Half width ($M_{K\pi\pi} - M_{\mathrm{D}^0}$) [GeV/$c^2$]	0.3	0.3	0.3	0.3	0.3	0.3	0.3	0.3	0.3	0.3	0.3
$p_{\mathrm{T,min}}$ of π_{soft} [GeV/c]	0.05	0.05	0.05	0.05	0.05	0.05	0.05	0.05	0.05	0.05	0.05
$p_{\mathrm{T,max}}$ of π_{soft} [GeV/c]	100	100	100	100	100	100	100	100	100	100	100
θ, angle between π_{soft} and D^0 [rad]	1	1	1	1	1	1	1	1	1	1	1
$\lvert\cos\theta_{point_{XY}}\rvert$	-1	-1	-1	-1	-1	-1	-1	-1	-1	-1	-1
NormDecayLength$_{XY}$	0	0	0	0	0	0	0	0	0	0	0

TABLE 3.1: Table of the topological and kinematic selection cuts applied for the D^{*+} analysis in proton-proton collisions at $\sqrt{s} = 5.02$ TeV. Some of the selection cuts, like the $p_{\mathrm{T,max}}$ of π_{soft} and the NormDecayLength, are not used in this analysis.

detector are employed. A track can be identified in units of resolution of the difference between the measured and expected signals using $n\sigma$ cuts. In this analysis, a 3σ compatibility cut was applied for both the TPC and TOF signal. If there was no TOF signal, only the TPC detector was used for the particle identification. Contradicting particle identifications were considered as non-identified. With this particle identification strategy, the combinatorial background is reduced without a significant loss of signal. Because in two of the higher transverse momentum bins (10-12 and 16-24 GeV/c, respectively) there was almost no combinatorial background, the particle identification strategy was not used, as it had a negative effect on the signal extraction.

In addition to these cuts, events with pile-up were rejected using the standard SPD algorithm: IsPileUpFromSPD. This algorithm searches for pile-up vertices above a certain distance from the primary vertex with a minimum number of contributors. The standard values for the algorithm are used: a separation in z between the two vertices of 0.6 cm and a minimum number of contributors to the primary vertex of 3.

3.3.2 Signal extraction

The D^{*+}-meson yields in the different p_T bins were extracted with a fit to the invariant mass distribution. The fitting function contains a threshold function convoluted with an exponential for the background and a Gaussian term for the signal. The background function is shown in equation 3.1:

$$f_{\text{back}}(x) = a\sqrt{x - m_\pi}\ \ \mathrm{e}^{b(x-m_\pi)}, \tag{3.1}$$

where a and b are free parameters and m_π the pion mass.

The D^{*+}-meson signal was successfully extracted in the p_T bins: 1-2, 2-3, 3-4, 4-5, 5-6, 6-7, 7-8, 8-10, 10-12, 12-16 and 16-24 GeV/c. The difference in invariant mass (ΔM) of the D^{*+} mass and of the D^0 for each p_T bin are shown in Figure 3.8. The significance is higher than 5 for all p_T bins except for the first (1-2 GeV/c) and last one (16-24 GeV/c) where the significance is respectively 4.7 and 3.0. For the last p_T bin, this is a statistics issue.

The mass distributions for true D^{*+} mesons from the MC are shown in Figure 3.9. Because the invariant mass distributions in the first three p_T bins have tails on the right side of the Gaussian peak, the range of the fit is shortened. The peak position and width for the D^{*+} meson, as obtained from the fits to data and MC, are shown in Figure 3.10. The solid and dashed lines in the left panel indicate the expected invariant mass and errors for the D^{*+} minus the D^0 mass obtained from the Particle Data Group [5]. The mean of the MC simulation is in general a bit above the expected PDG mass, which was also the case for the D^{*+} analysis at $\sqrt{s} = 8$ TeV [38]. The mean of the data is, within statistical errors, compatible with both the MC and the PDG values. Only the mean in p_T bin 10-12 GeV/c is on the high side, which is because the fit suffers from too few background entries on the left side and a statistical fluctuation on the right side of the peak. In the right panel of Figure 3.10, the widths of the fits for data and MC are compared. All p_T bins agree within statistical errors.

The D^{*+}-meson raw yields are extracted from the respective fit functions by considering a 3σ interval around the peak position. Table 3.2 shows the raw yields and signal-to-background ratios in all p_T bins.

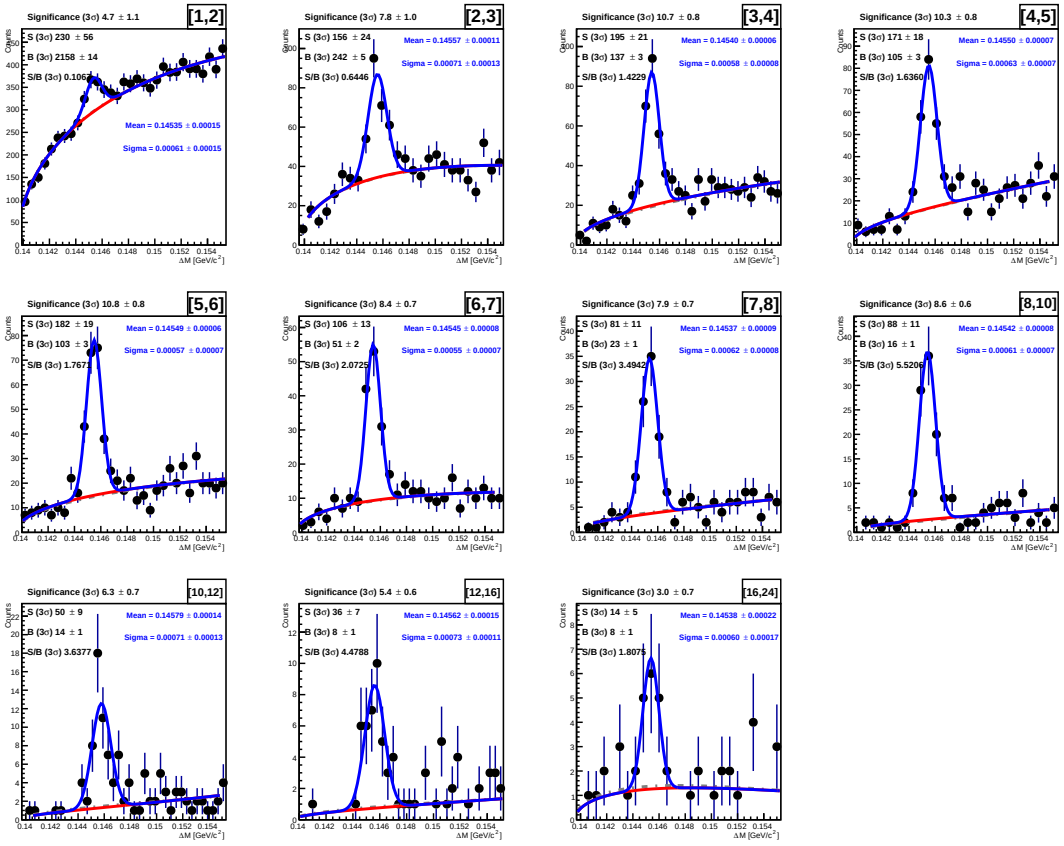

FIGURE 3.8: Distribution of the difference in invariant mass ($K\pi\pi - K\pi$) for different p_T bins. The background fit is given in red, the background plus signal curve in blue.

p_T	D^{*+}	
(GeV/c)	S	S/B
[1-2]	230 ± 56	0.1067
[2-3]	156 ± 24	0.6446
[3-4]	195 ± 21	1.4229
[4-5]	171 ± 18	1.6360
[5-6]	182 ± 19	1.7671
[6-7]	106 ± 13	2.0725
[7-8]	81 ± 11	3.4942
[8-10]	88 ± 11	5.5206
[10-12]	50 ± 9	3.6377
[12-16]	36 ± 7	4.4788
[16-24]	14 ± 5	1.8075

TABLE 3.2: Raw yields (considering a 3σ interval) and signal-to-background ratios for the D^{*+} meson.

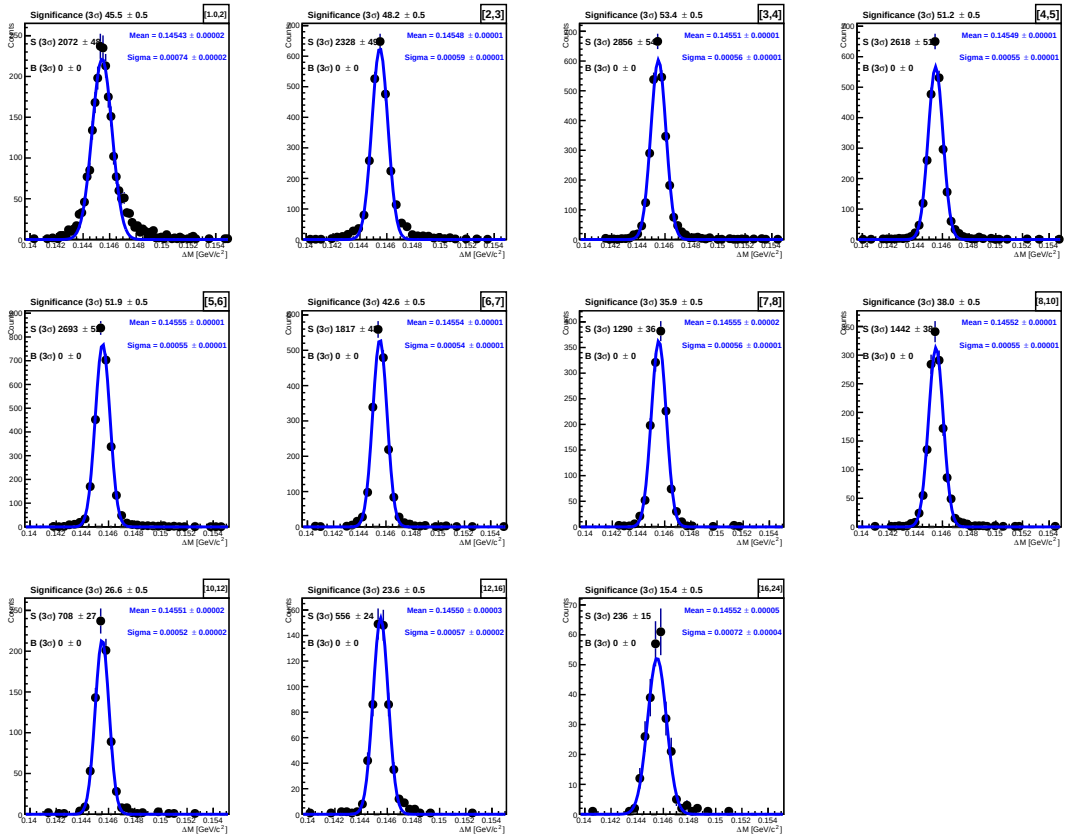

FIGURE 3.9: Distribution of the difference in invariant mass ($K\pi\pi - K\pi$) for true MC D^{*+} mesons. For the first three bins, the fit range is shortened because of the tails at the right side of the peak.

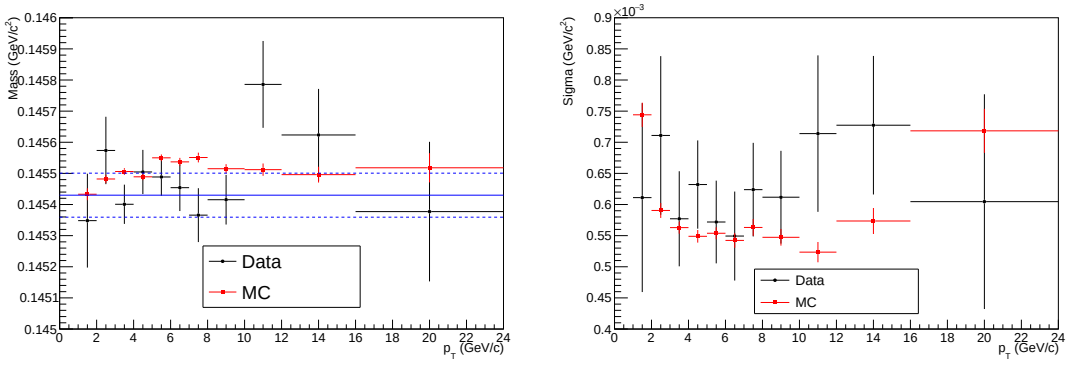

FIGURE 3.10: Comparison of the fit parameters between data and MC for the D^{*+} meson. The extracted mass is shown in the left panel, and the width of the peak on the right. The blue lines indicate the value and uncertainties from the PDG [5].

3.4 Results

The raw yields, as obtained in the previous section, are one of the ingredients to calculate the invariant cross-section of D^{*+} mesons at $\sqrt{s} = 5.02$ TeV. The acceptance-times-efficiency correction, Acc $\times \epsilon$, and the relative feed-down contribution from B meson decays, f_{prompt}, are also needed. These corrections will be discussed in the next two subsections, where the final results are presented at the end of this section. The systematic uncertainties on this measurement, which will already be included in the figures shown here, are discussed in the next section.

3.4.1 Acceptance and efficiency corrections

The acceptance-times-efficiency correction was obtained using the LHC16i6a MC sample for the D^{*+}-meson efficiency calculations and a toy MC for the acceptance correction. This correction is needed to account for the limited performance of the ALICE detector, so one gets an invariant cross-section. The efficiency is calculated for both prompt and feed-down D^{*+} mesons, where the latter is needed for the feed-down correction.

The MC sample LHC16i6a is used to calculate the efficiency of the ALICE detector after each step in the reconstruction procedure. In the end, the efficiency is given by the fraction of reconstructed D^{*+} mesons after PID selection over the number of MC particles generated in the acceptance. The acceptance itself is generated using a toy MC, which makes use of the framework of event generator Pythia. The final acceptance is calculated by dividing the number of generated protons, pions and kaons in the acceptance over those within a limited acceptance ($|y| < 0.5$).

Figure 3.11 shows the acceptance-times-efficiency for prompt and feed-down D^{*+} mesons. As observed, the acceptance-times-efficiency increases with the transverse momentum. For prompt D^{*+} mesons, the Acc $\times \epsilon$ varies between a few percent at small p_{T} to 40-80% at large transverse momenta. The efficiency for D^{*+} mesons coming from B decays is larger than for prompt D^{*+} mesons due to the fact that the decay vertices of the feed-down D^{*+} mesons are more displaced from the primary vertex and, thus, they are more efficiently selected by the used cuts.

3.4.2 Feed-down subtraction

Because the topological selection criteria are preferentially selecting feed-down D^{*+} mesons, a subtraction strategy is needed to calculate the prompt D^{*+}-meson production cross-section. In ALICE, two methods are available, the so-called f_{c} method:

$$f'_{\mathrm{prompt}} = \left(1 + \frac{(\mathrm{Acc} \times \epsilon)_{\mathrm{feed-down}}}{(\mathrm{Acc} \times \epsilon)_{\mathrm{prompt}}} \cdot \frac{\left(\frac{\mathrm{d}^2\sigma}{\mathrm{d}y\,\mathrm{d}p_{\mathrm{T}}}\right)^{\mathsf{FONLL}}_{\mathrm{feed-down}}}{\left(\frac{\mathrm{d}^2\sigma}{\mathrm{d}y\,\mathrm{d}p_{\mathrm{T}}}\right)^{\mathsf{FONLL}}_{\mathrm{prompt}}} \right)^{-1} , \tag{3.2}$$

and the N_{b} method

$$f_{\mathrm{prompt}} = 1 - \left(\frac{\mathrm{d}^2\sigma}{\mathrm{d}y\,\mathrm{d}p_{\mathrm{T}}}\right)^{\mathsf{FONLL}}_{\mathrm{feed-down}} \cdot \frac{(\mathrm{Acc} \times \epsilon)_{\mathrm{feed-down}} \cdot \Delta y \cdot \Delta p_{\mathrm{T}} \cdot \mathrm{BR} \cdot L_{int}}{N^{\mathrm{D\,raw}}/2} . \tag{3.3}$$

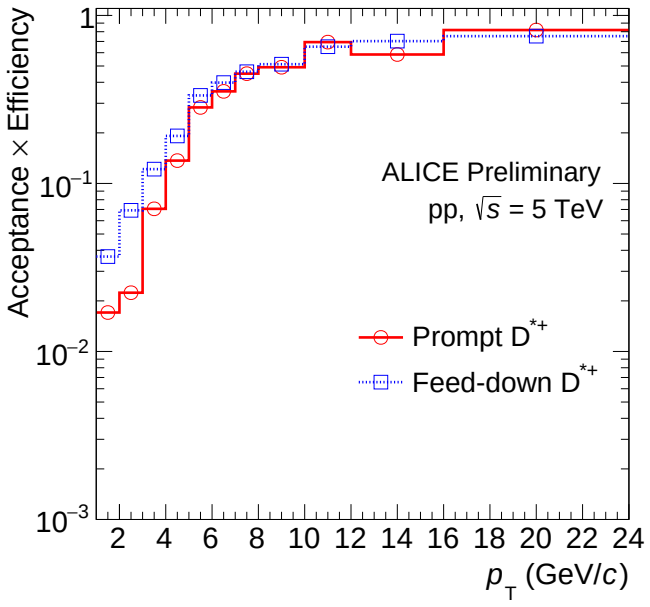

FIGURE 3.11: Acceptance-times-efficiency for prompt and feed-down D^{*+} mesons calculated using the LHC16i6a MC sample. This plot includes the fact that PID is not used for p_{T} bins 10-12 and 16-24 GeV/c.

The first method needs both the FONLL prediction for prompt and feed-down D mesons, where the N_{b} only needs the prediction for beauty feed-down. Previous D^{*+}-meson production cross-section measurements in ALICE at $\sqrt{s} = 2.76$ TeV, 7 TeV (pass2) and 8 TeV were using a combination of both methods [38–40]. However, as these and other LHC experiment D-meson measurements systematically lay on the upper edge of the FONLL uncertainty band, while FONLL provides a good description of B^{+}, B^{0} and B$_{\mathrm{s}}$ mesons [41, 42], it was decided to only use the N_{b} method for this analysis.

3.4.3 Production cross-section

The final p_{T} differential production cross-section for prompt D^{*+} mesons is calculated using:

$$\left.\frac{\mathrm{d}\sigma^{\mathrm{D}}}{\mathrm{d}p_{\mathrm{T}}}\right|_{|y|<0.5} = \frac{1}{2}\frac{1}{\Delta y \Delta p_{\mathrm{T}}}\frac{f_{\mathrm{prompt}}(p_{\mathrm{T}}) \cdot N^{\mathrm{D\,raw}}(p_{\mathrm{T}})\big|_{|y|<y_{\mathrm{fid}}}}{(\mathrm{Acc}\times\epsilon)_{\mathrm{prompt}}(p_{\mathrm{T}}) \cdot \mathrm{BR} \cdot L_{int}}\,. \tag{3.4}$$

The cross-section is calculated per unit of rapidity and momentum. The factor 1/2 is necessary to account for the fact that $N^{\mathrm{D\,raw}}$ contains both particles and antiparticles. f_{prompt} is the fraction of prompt D^{*+} mesons to separate the contributions from feed-down D^{*+} mesons. $N^{\mathrm{D\,raw}}$ is the raw yield as obtained by a fit to the invariant mass spectra as discussed in subsection 3.3.2. The acceptance-times-efficiency, Acc $\times\,\epsilon$, is used as discussed above. BR is the branching ratio of the decay of interest and L_{int} is the integrated luminosity. This is the number of analysed events (approximate 116 million for this sample) divided by the total inelastic cross-section measured as $(51.2\pm1.2)\cdot10^{6}$ nb based on measurements of the Van der Meer scan performed on the LHC15n data sample [43].

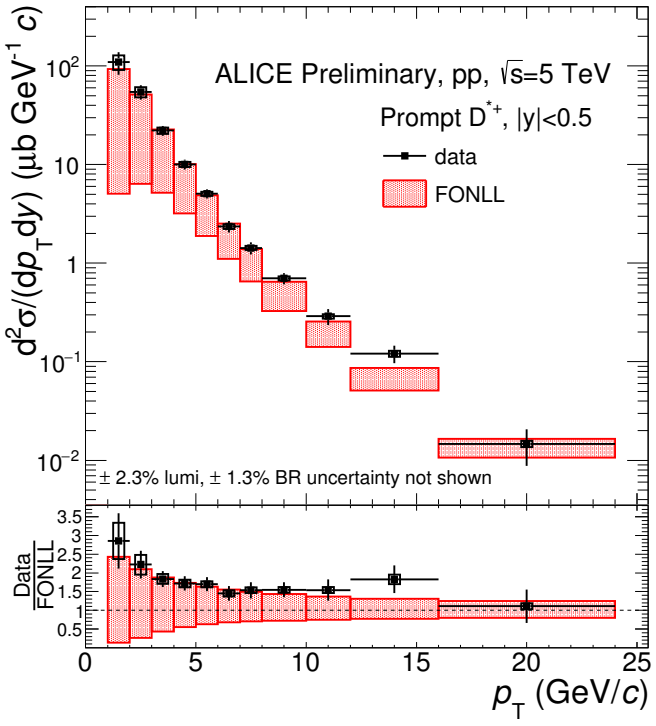

FIGURE 3.12: D^{*+}-meson p_T inclusive production cross-section in pp collisions at $\sqrt{s} = 5$ TeV compared with FONLL calculations (top). Ratio of the measured cross-section and the predicted central value for FONLL (bottom).

The measured cross-sections are compared to FONLL calculations in Figure 3.12. Contributions to the systematic error in these and following plots are discussed in section 3.5. The various contributions are added in quadrature. Several performed checks, like splitting in positive and negative eta ranges or splitting in low, intermediate and high intensity runs, confirm the results presented here.

While compatible with the FONLL error band, the central FONLL predictions are on average lower than the measured cross-section. It can be noted that this is also the case for the D^0 and D^+ mesons in the same date sample [36]. Therefore, FONLL tends to underestimate charm production in pp at $\sqrt{s} = 5$ TeV as was already noted at higher (7 and 8 TeV) and lower (2.76 TeV) collision energies [38, 39, 44]. As an extra comparison, the D^{*+} meson cross-section from this analysis is also compared to the pp at 7 TeV (pass4) and 8 TeV cross-sections (see Figure 3.13). For this ratio, the raw yield extraction, cut variation, MC p_T shape, tracking, normalisation and PID systematics are taken as non-correlated. The feed-down systematic is partially correlated and the branching ratios correlated. The fully correlated systematics drop out in the ratio, for the partially correlated systematics the largest of the two is taken and the non-correlated systematics are added in quadrature. Also several systematic uncertainties of the pQCD models cancel in these energy ratios, which offer a great potential for sensitive tests of and constraints on the gluon density function [45].

In the bottom of Figure 3.13, it is visible that the 7 TeV (pass4) / 5 TeV ratio for the D^{*+} meson is in general lower compared to the same ratio for the central values of the FONLL calculations. The 8 TeV / 5 TeV ratio for the D^{*+} meson is more compatible

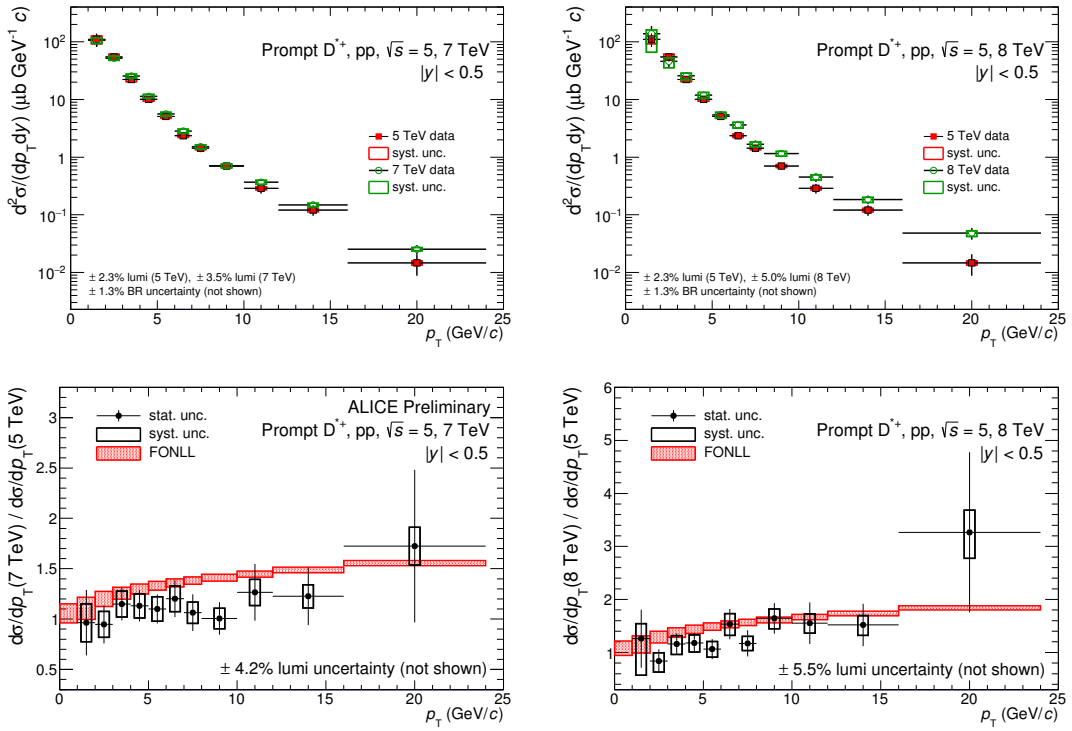

FIGURE 3.13: Top: prompt D^{*+}-meson production cross-section at 5 TeV compared to the result in 7 TeV (pass4) (left) and 8 TeV (right). Bottom: Ratio 7 TeV (pass4) over 5 TeV (left) and ratio 8 TeV over 5 TeV (right) compared with the same ratio from FONLL calculations. Note the different y-axis in the ratio plots.

with the FONLL calculations. For the D^0 meson a similar trend was observed [36]. The statistical errors on the 2.76 TeV cross-section measurement were too large. Therefore, the comparison between 5 TeV / 2.76 TeV and FONLL are not shown here.

In Figure 3.14, the ratio between the measured cross-sections for all three D mesons is plotted for both 5 TeV and 7 TeV (pass4), again with the same ratio for the FONLL values. These species ratios are important, as they are sensitive to the different fragmentation functions for D mesons. The data points agree with FONLL within statistical errors, but no significant p_{T} dependence is observed. In the 5 TeV ratio plots, fewer outliers are observed than for the 7 TeV (pass4) ratios. For this type of ratio, the raw yield extraction, cut variation, branching ratio and MC p_{T} shape systematics are taken as non-correlated. The feed-down systematic is partially correlated and the tracking, normalisation and PID systematics are correlated. Note that FONLL does not predict these ratios by itself, values for the fragmentation functions are taken from Ref. [46].

As said before, this cross-section measurement at $\sqrt{s} = 5$ TeV is important as a reference for the results from p-Pb and Pb-Pb collisions. Because of the tight schedule for Quark Matter 2017, the corresponding preliminaries for Pb-Pb have been made with the extrapolated 7 TeV (pass4) cross-section. In Figure 3.15, the comparison between this extrapolated cross-section measurement and the measurement at $\sqrt{s} = 5$ TeV is shown. This pQCD based energy scaling method, explained in detail in Ref. [39], uses the ratio of the theoretical cross-sections at 5.02 and 7 TeV calculated using FONLL to scale down the 7 TeV (pass4) measurement to 5.02 TeV.

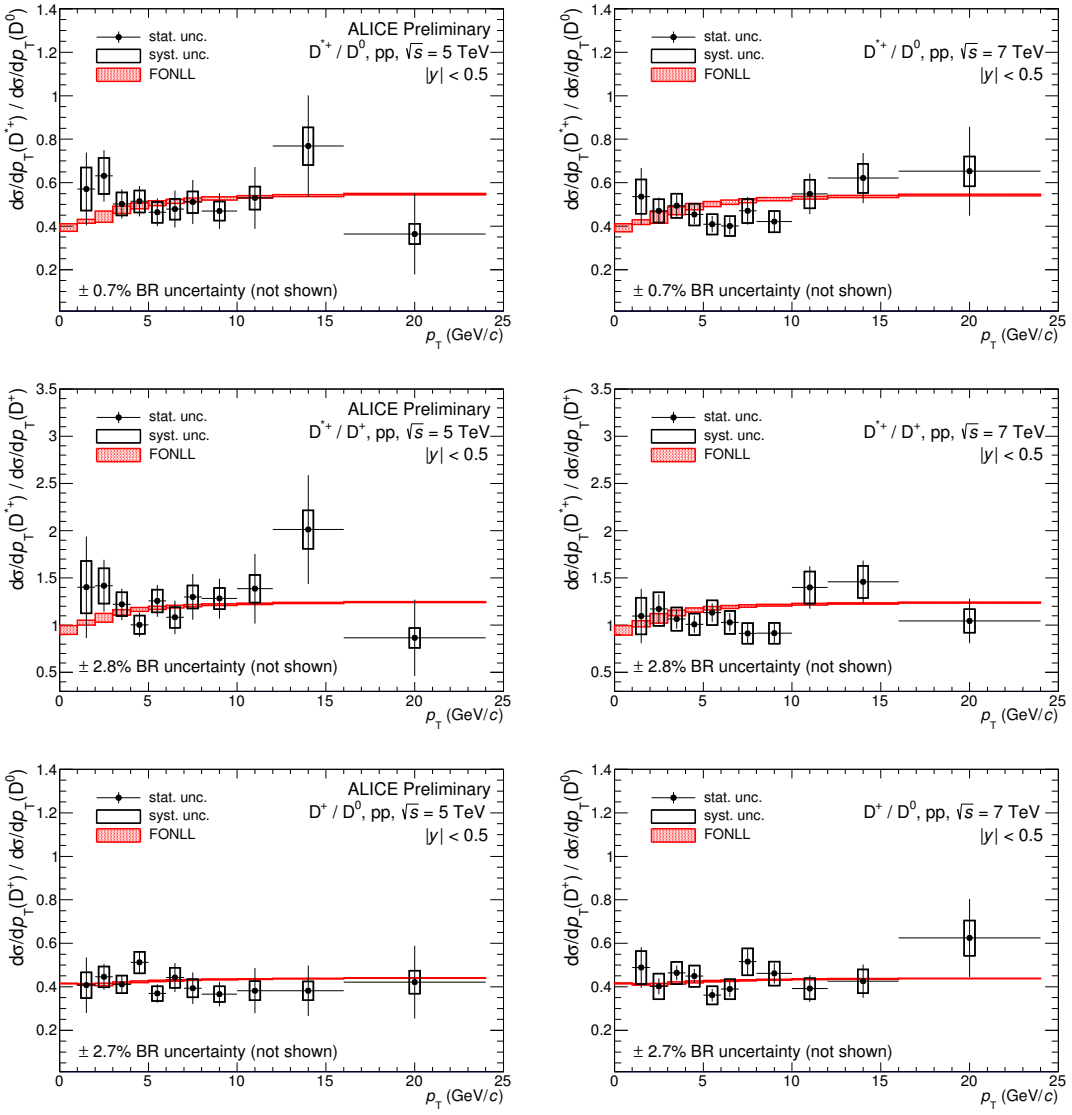

FIGURE 3.14: Ratio between the different D meson production cross-section compared to the same ratio for FONLL. Top: ratio D^0 over D^{*+} for 5 (left) and 7 TeV (pass4) (right). Middle: ratio D^{*+} over D^+ for 5 (left) and 7 TeV (pass4) (right). Bottom: ratio D^0 over D^+ for 5 (left) and 7 TeV (pass4) (right).

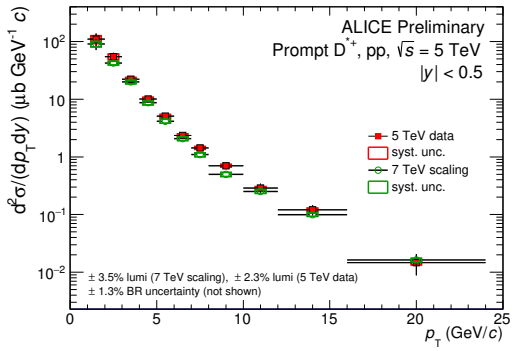

FIGURE 3.15: Comparison between the measured 5 TeV cross-section and the (for Quark Matter 2017 used pp reference) extrapolated 7 TeV (pass4) cross-section for the D^{*+} meson.

3.5 Systematic uncertainties

The sources of systematic uncertainties considered in this analysis are following from:

- Extracting the raw yields;
- Cut variation;
- The particle identification strategy;
- The MC p_{T} shape of the generated D^{*+} mesons;
- The feed-down subtraction;
- The tracking efficiency;
- Pile-up.

3.5.1 Raw yield

The systematic error on the yield extraction was estimated by comparing the differences in extracted yield when the fit parameters and constraints were varied. The raw yield was extracted while:

- Varying the range of the invariant mass fit;
- Using a different background fit function. A power law instead of a power law convoluted with an exponential was used;
- Rebinning the histogram;
- Using two bin counting methods to extract the yield, based on counting the entries within $n\sigma$ of the peak after subtracting the background;

The resulting deviations from the default method are shown in Figure 3.16. The systematic is given by the root mean square (RMS) of the deviations from 1.

To check if these deviations in the raw yield extraction are due the used method and not of statistical natures, a multi-trial method is performed where each point in the invariant mass spectra is smeared 5000 times with Poisson statistics. The RMS of the obtained smeared yields per p_{T} bin is compared with the yield obtained from the fit on the data. No significant deviations where found. Besides this check, also a second multi-trial method was performed where the data was fitted with approximate 500 different fit trials (varying the fit range, rebin values and first used bins). An example for p_{T} bin 3-4 GeV/c is visible in Figure 3.17. The assigned systematic here is the sum of the mean and RMS of the difference in yield plot (where the outliers were double checked). A comparison between the assigned raw yield extraction systematic for the one- and multi-trial method can be found in Figure 3.18. Both multi-trial methods confirm the results obtained with the one-trial method.

The final assigned systematic is a combination of both the one- and multi-trial method. Since the systematic error is expected to be reasonably smooth as a function of p_{T}, additional smoothening of the systematic uncertainties is performed. Together with the other systematic contributions, these numbers are shown in Table 3.4 on page 33.

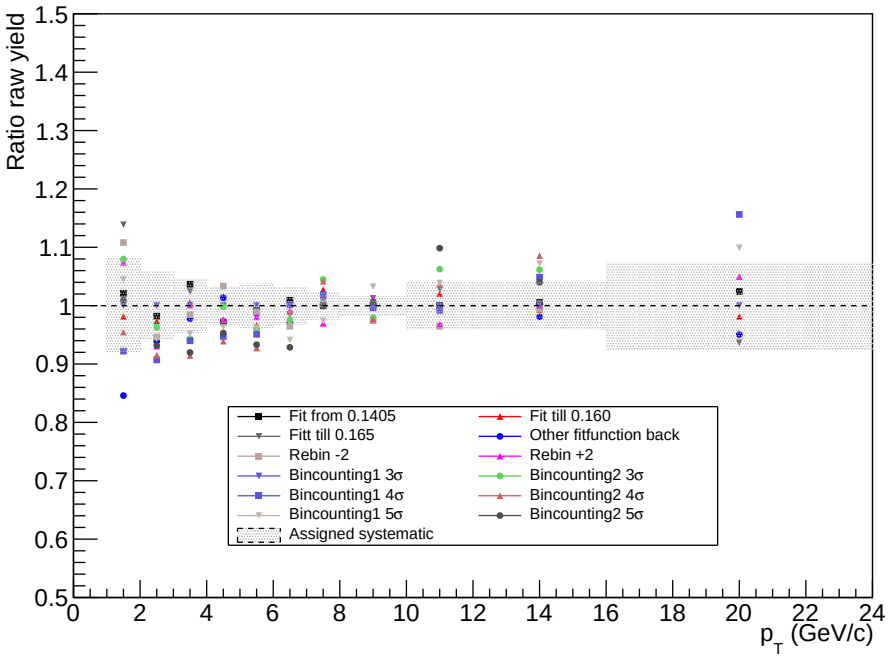

FIGURE 3.16: Systematic uncertainty in raw yield extraction for the D^{*+} meson.

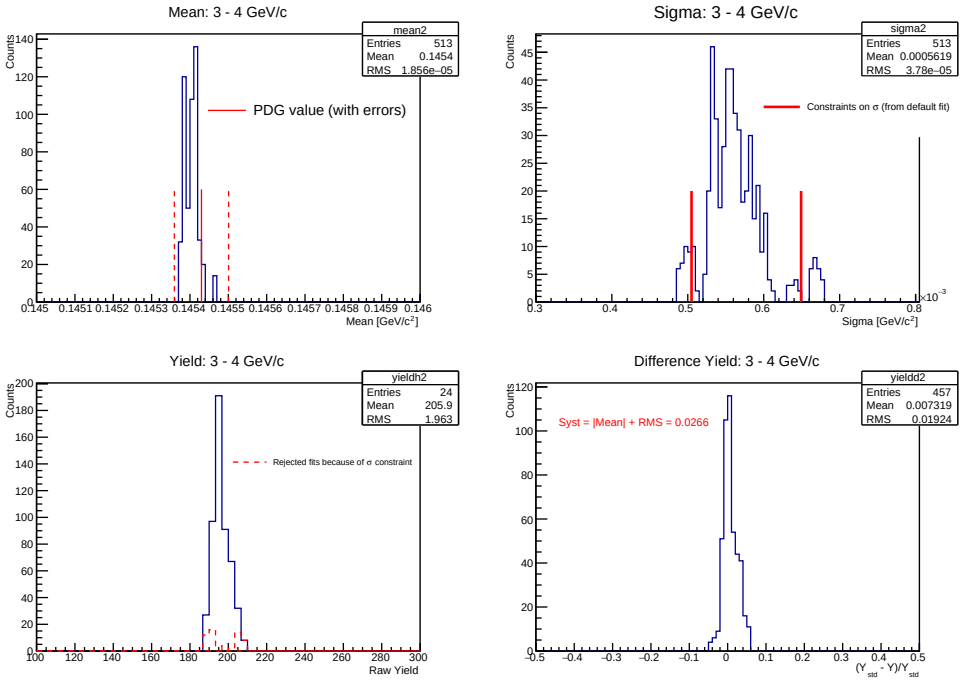

FIGURE 3.17: Output of the multi-trial fitting method to the D^{*+}-meson invariant mass distributions in the p_{T} interval 3-4 GeV/c.

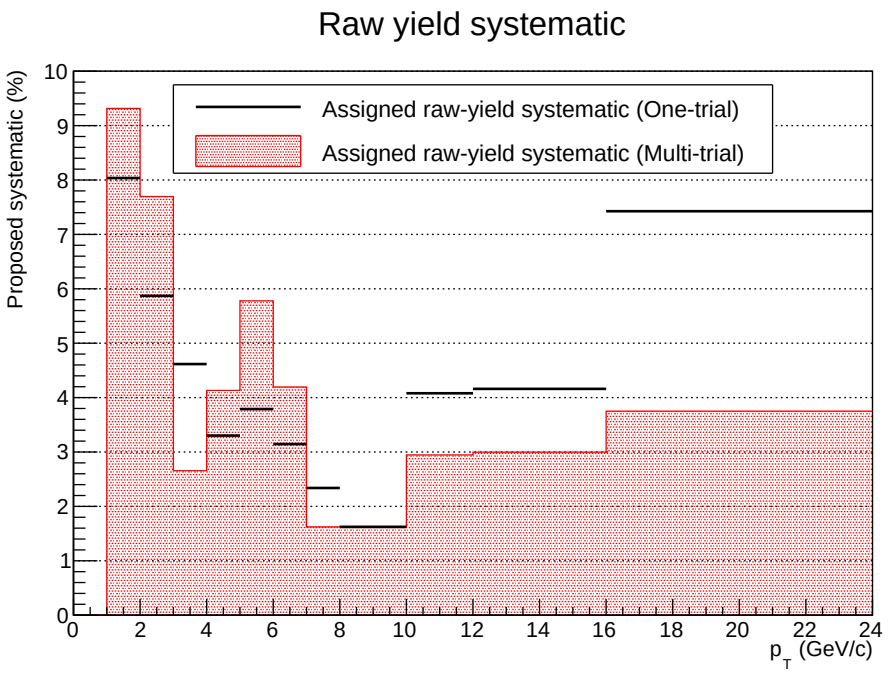

FIGURE 3.18: Comparison of the systematic uncertainty in raw yield extraction for the D^{*+} meson, calculated with the one- and multi-trial method. The final assigned value is taken as a combination of both methods and can be found in Table 3.4.

3.5.2 Selection efficiency

The systematic uncertainty due to possible imperfections in the description in the simulations of the variables used in the geometrical selections of the D^{*+} meson displaced decay vertices was studied by repeating the analysis varying the applied selection criteria.

The systematic uncertainty on the selection efficiency for the D^{*+} meson has been performed varying the selection cuts with respect to the chosen central values, reported in Table 3.1. The most effective cuts were varied: the distance of closest approach (DCA), the cosine of the pointing angle between the D^0 flight line and the reconstructed D^0 momentum ($\cos\theta_{\mathrm{point}}$) and the product of impact parameters from the kaon and pion ($d_0^{\mathrm{K}} \cdot d_0^{\pi}$). Each of these cuts were varied by 5%, 10%, 15% or 20% both tighter and looser (for one set of cuts, all cut variables are varied simultaneously in the same direction).[2]

The raw yield has been extracted fitting the mass spectra with a Gaussian function for the signal peak, with the width fixed to the value of the central values, in order to limit fluctuations due to the fit performance. The ratio of the corrected cross-section obtained with the varied cut sets and the default one is shown in Figure 3.19. The assigned systematic, starting from the RMS of the cross-section ratio plot, is decreasing for increasing p_{T}, which is expected because the cuts are getting looser as one can see in Figure 3.20. For $p_{\mathrm{T}} > 7$ GeV/c, the cuts are basically completely open.

[2]For the cosine of the pointing angle cut, the difference with 1 was used to loosen or tighten the cut.

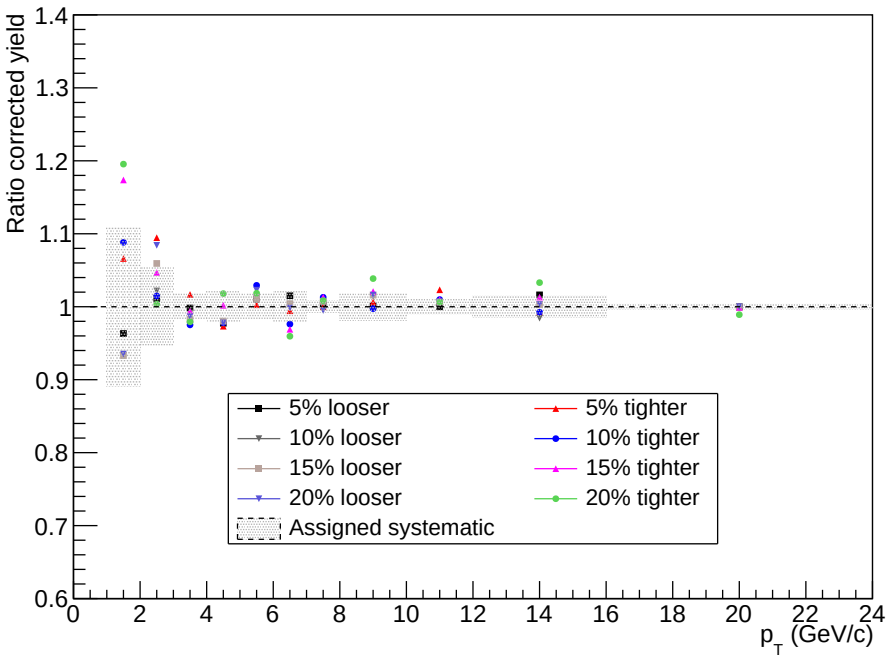

FIGURE 3.19: Assigned systematic uncertainty due to cut variation for the D^{*+} meson. The assigned systematic in the plot is the RMS of the difference of all points with 1.

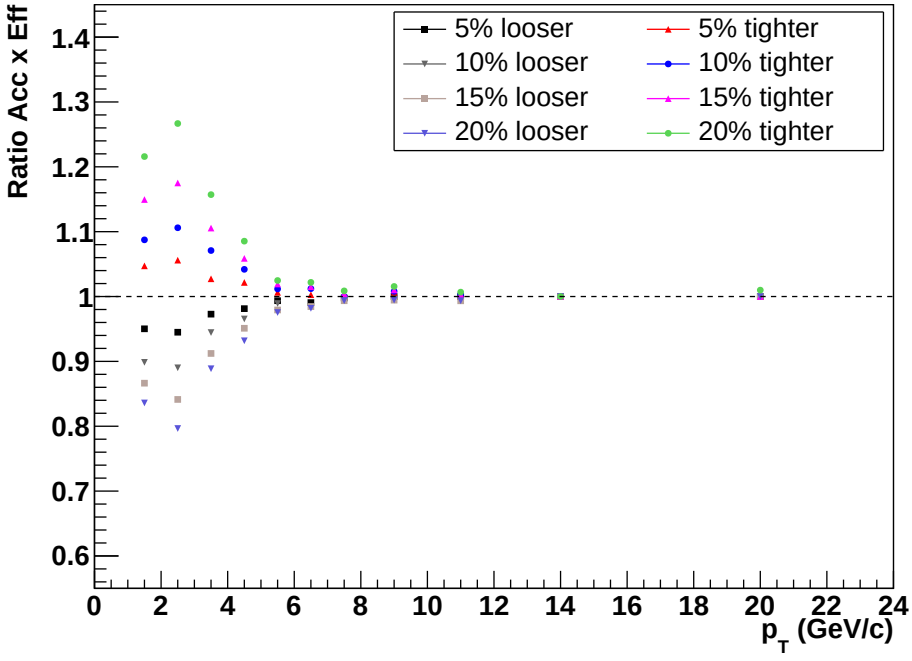

FIGURE 3.20: Effect of the cut variation on the efficiency-times-acceptance for the D^{*+} meson.

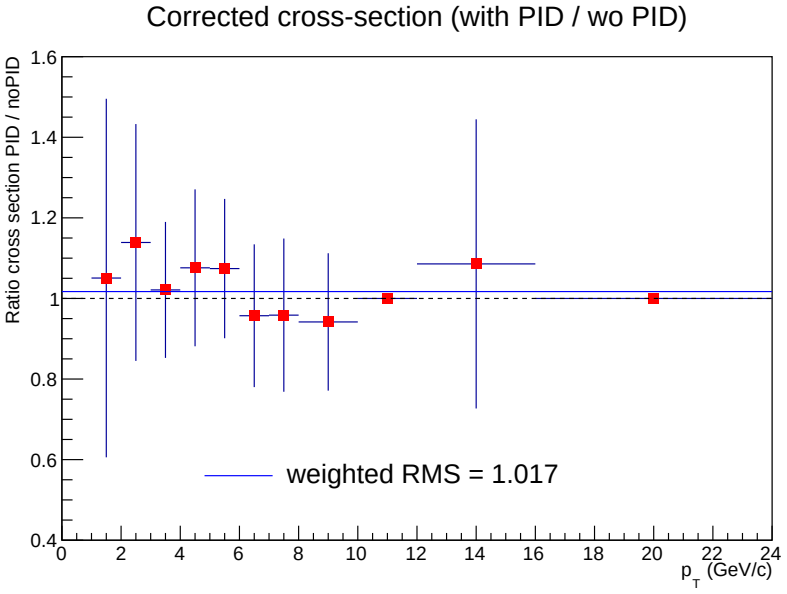

FIGURE 3.21: Systematic uncertainty due to particle identification for the D^{*+} meson. This figure shows the ratios of the corrected cross-section with and without PID. The assigned systematic is given by the weighted root mean square (indicated by the blue line).

3.5.3 Particle identification

The effect of the particle identification strategy used in this analysis, see subsection 3.3.1, was studied by comparing the obtained cross-section with and without using PID. Obviously, the significance drops when the particle identification is turned off, but a good signal in all p_{T} bins remains.

The ratio of the corrected cross-section with and without PID is shown in Figure 3.21. Note that for p_{T} bins 10-12 and 16-24 GeV/c, PID was not used. The values are all consistent with one and the RMS is smaller than 3%, which is compatible with the expected efficiency of the PID strategy. Therefore, no systematic error is assigned due to PID.

3.5.4 Monte-Carlo p_{T} shape

The effect of the shape of the simulated D^{*+} meson p_{T} spectrum from Pythia was estimated from the relative variation in the Monte Carlo efficiencies obtained after using p_{T} shapes from FONLL. This can be done by computing the efficiency with and without making use of the AliCFTaskVertexingHF task, which allows to use p_{T} dependent weights to correct for the difference between the Pythia and FONLL p_{T} spectrum.

The relative variation of the efficiencies using these different p_{T} shapes can be seen in Figure 3.22. The differences with one are smaller than 1%, so no systematic uncertainty due to the p_{T} shape is assigned.

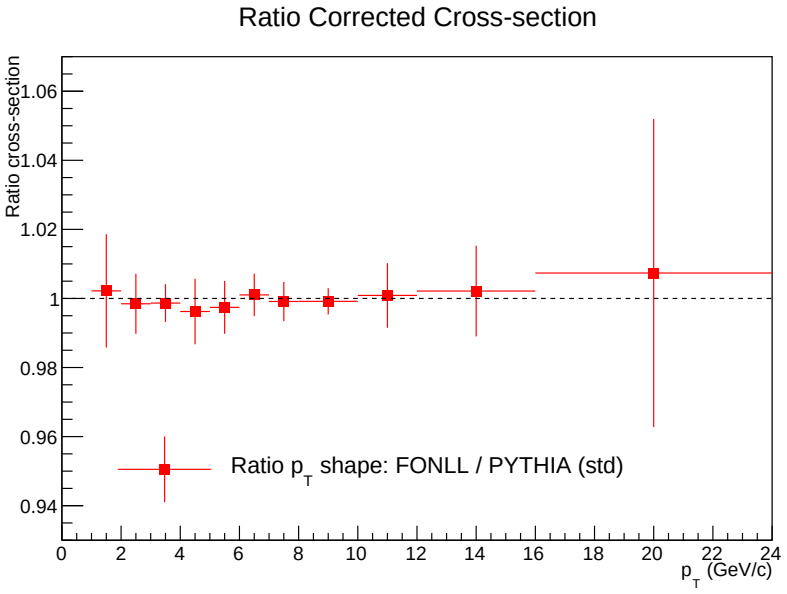

FIGURE 3.22: Systematic uncertainty due to the used MC p_{T} shape for the D^{*+} meson.

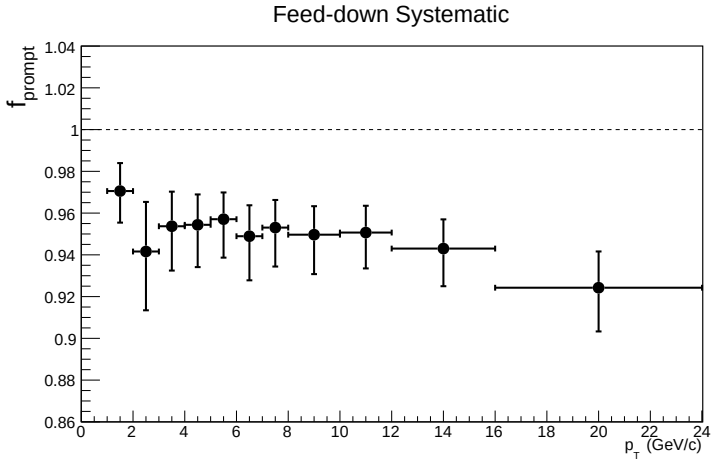

FIGURE 3.23: Fraction of prompt D^{*+} mesons. The assigned feed-down systematic uncertainties are the (asymmetric) error bars in each p_{T} bin.

3.5.5 Feed-down

By varying the parameters for the FONLL B predictions used in the N_{b} method, the systematic uncertainty of the feed-down estimation is calculated. The asymmetric errors on the value for f_{prompt} in Figure 3.23 are the assigned systematics. See Table 3.4 for the smoothened numbers.

3.5.6 Tracking efficiency

The systematic uncertainty related to the tracking efficiency includes the effects arising from track finding in the TPC, from track propagation from the TPC to the ITS and from track quality selections. It was estimated with the following tests:

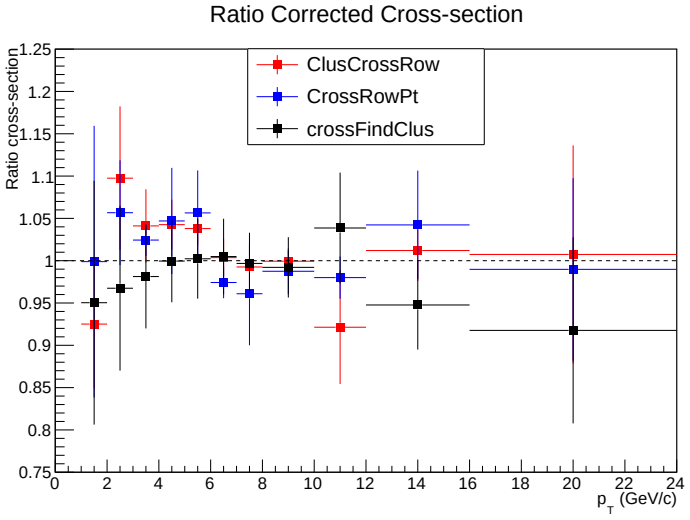

FIGURE 3.24: Ratio of the default cross-section with the cross-section calculated after varying the quality track cuts for the D^{*+} meson.

- Comparison of the D^{*+}-meson cross-sections obtained with different track selection cuts;
- Comparison of the TPC-ITS track matching efficiency in data and simulations.

The D^{*+}-meson raw yield, efficiency and corrected yield were evaluated with different sets of track selection cuts. Only one cut at a time was changed with respect to the standard values. In particular, the following three cut variations were tested:

1. Number of TPC crossed rows $> 120 - (5/p_{\mathrm{T}})$;
2. Number of TPC clusters $> 0.65 \times$ number of TPC crossed rows;
3. Ratio of crossed rows over findable clusters in the TPC > 0.9.

In Figure 3.24, the ratio of the different cross-sections can be found. Based on the variation of the distributions, a systematic uncertainty of 3% was estimated. This corresponds to a 1% uncertainty per track, as the D^{*+} meson is reconstructed from a three-body decay channel. This is consistent with the assigned systematic for the D^{+} and D^{0} meson.

The second part of the tracking efficiency is D meson independent, and calculated by the analysers of the D^{0} meson. This TPC-ITS track matching efficiency is defined as the fraction of tracks with clusters in both the ITS and TPC over the total number of tracks with clusters in the TPC. The systematic uncertainty arises from discrepancies between data and MC. A detailed description of this calculation can be found in Ref. [44]. In the end, both parts of the tracking systematic are combined using a MC simulation that uses the same topological and PID cuts as used in the analysis. The final assigned systematic uncertainties are quoted in Table 3.4.

Option	No. Contributors	Separation z (cm)
1	3	0.8
2	4	0.8
3	5	0.8
4	6	0.8
11	3	0.8
12	3	0.9
13	3	1.0
14	3	1.1
15	3	1.2
16	3	1.3
17	3	1.4

TABLE 3.3: Different variations used to estimate the percentage of pile-up in the data sample LHC15n. The options correspond to the bin numbers in Figure 3.25.

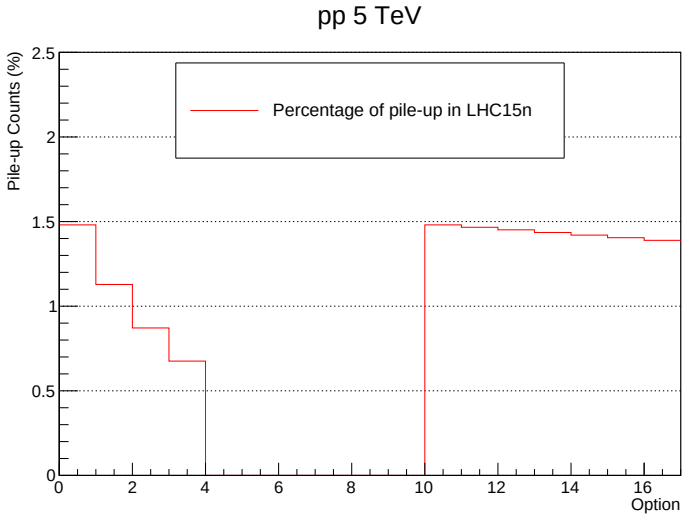

FIGURE 3.25: Percentage of pile-up events in data sample LHC15n. The different bins correspond to the scan of the parameters as reported in Table 3.3.

3.5.7 Pile-up

In order to check the in bunch pile-up of the 5 TeV sample, the standard SPD algorithm was used: IsPileUpFromSPD. This algorithm is searching for pile-up vertices above a certain distance from the primary vertex and with a minimum number of contributors.

The standard values for the algorithm are a separation in z between the two vertices of 0.6 cm and a minimum number of contributors to the primary vertex of 3. In order to systematically check for possible instabilities, it was decided to modify those two values according to Table 3.3. The results of the variations are displayed in Figure 3.25. This study shows an in bunch pile-up well below 1.5%, which includes also events without D^{*+} candidates. This percentage of events is rejected in the cut file, and no systematic uncertainty is assigned.

p_T [GeV/c]	1-2	2-3	3-4	4-5	5-6	6-7	7-8	8-10	10-12	12-16	16-24
Raw yield	9	7	4	4	5	4	2	2	3	3	5
Cut Variation	11	5	2	2	2	2	1	1	1	1	0
Feed-down above	1	2	2	1	1	1	1	1	1	1	2
Feed-down below	1	3	2	2	2	2	2	2	2	2	2
Tracking	6	6	6	5	5	5	5	5	5	6	7
PID MC p_{T} shape Pile-up	Negligible										

TABLE 3.4: Systematic uncertainties (in percentages) evaluated for the D^{*+} meson.

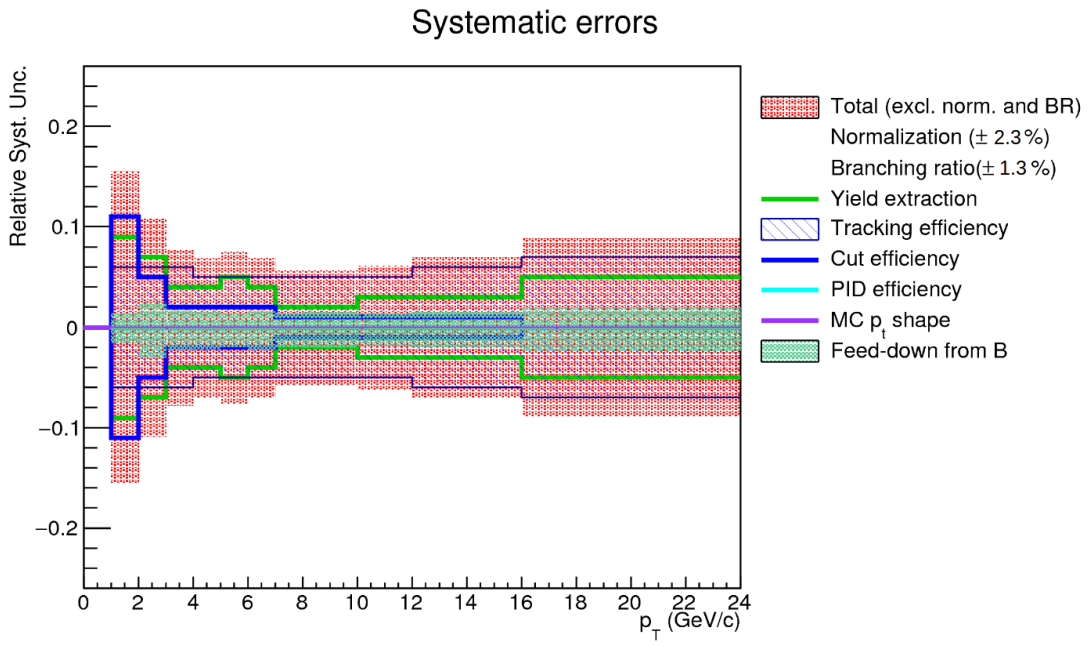

FIGURE 3.26: Relative systematic uncertainty evaluated for the D^{*+} meson. The different contributions are added in quadrature.

3.5.8 Total systematic uncertainties

Table 3.4 shows all the contributions to the systematic error as discussed in this section. The various contributions are added in quadrature. In addition to the values quoted here, a 2.3% systematic uncertainty is assigned due to normalisation. This number is a result from the Van der Meer scan of the 5 TeV data [43]. The assigned systematic uncertainties are also shown in Figure 3.26 and as boxes in the Figures 3.12 till 3.15.

3.6 Discussion

The results presented here, in combination with a similar cross-section analysis of the D^+ and D^0 meson, have been accepted by the ALICE Collaboration as preliminary results for the Quark Matter 2017 conference. This procedure consists out of many checks and needs the approval from the PAG, PWG and PB of the ALICE experiment. The Physics Forum accepted the results noted by "ALICE Preliminary" in the plots in this chapter. They are convinced that the analysis was performed correctly and the results show an interesting physical message for the community. In this section, I will discuss my opinion on some crucial points of this analysis.

First of all, the main conclusion of this analysis: the measured invariant D^{*+}-meson cross-section agrees within errors with FONLL calculations, although on the higher side of the theoretical error band. Similar conclusions were found for the D^+ and D^0 mesons in the same data sample, as can be seen in Figure 3.27. Additionally, other LHC experiments also measured a D-meson cross-section in the upper edge of the FONLL calculations [47–49]. An overview of these measurements is shown in Figure 3.28, where the total inclusive charm production cross-section in nucleon-nucleon collisions measured at different experiments is presented. For such a measurement, the p_{T} inclusive production cross-section needs to be extrapolated to the full transverse momentum and full phase space. Because of limited statistics in the 0-1 GeV/c transverse momentum bin, this was not possible with reasonable uncertainties using the measurement at $\sqrt{s} = 5.02$ TeV presented in this chapter. When the full data sample is collected, so together with the "long pp reference" run at the end of 2017, the total inclusive charm production cross-section at $\sqrt{s} = 5.02$ TeV will be calculated.

This measurement is performed using a framework that already exists for several years and which has been used for multiple publications by many different people. Although some parts could have been coded better, the classes are following the analysis strategy presented in this chapter. Of course, one can not be completely sure if there are no bugs somewhere, but if there are, I believe they are small and have a negligible effect on the final result. Otherwise, one of the many analysers would have noticed something.

The MC sample used for this analysis was produced quite short to the deadline for Quark Matter 2017. Therefore, there was some hurry in getting the results on time for the approvals. This has affected the precision in which the qualification assurance of Monte-Carlo sample LHC16i6a is performed. Although all standard D2H checks were looking fine, I would have preferred to do some additional checks. For example, the tails observed for the true D^{*+} mesons are not yet understood.

After the preliminaries were approved, some of the runs of period LHC15n (244377, 244411, 244617, 244618 and 24461) have been marked as bad by the Data Preparation Group for what concerns the MC productions. The technical details of the simulation of the TPC distortions had a negative effect on the matching efficiency, leading to a significant drop starting at $p_{\mathrm{T}} = 4$ GeV/c. The MC production was redone for these five runs, which in total contained approximate 6% of the statistics. A ratio of the old versus the new cross-section can be found in Figure 3.29. As we can see, the differences are very small in most of the p_{T} bins, so the final physical message will not change.

Finally, a lot of checks went into the 7 TeV (pass4) over 5 TeV ratio for the D^{*+} and D^0 mesons. Both ratios show a systematic trend downwards in comparison with the

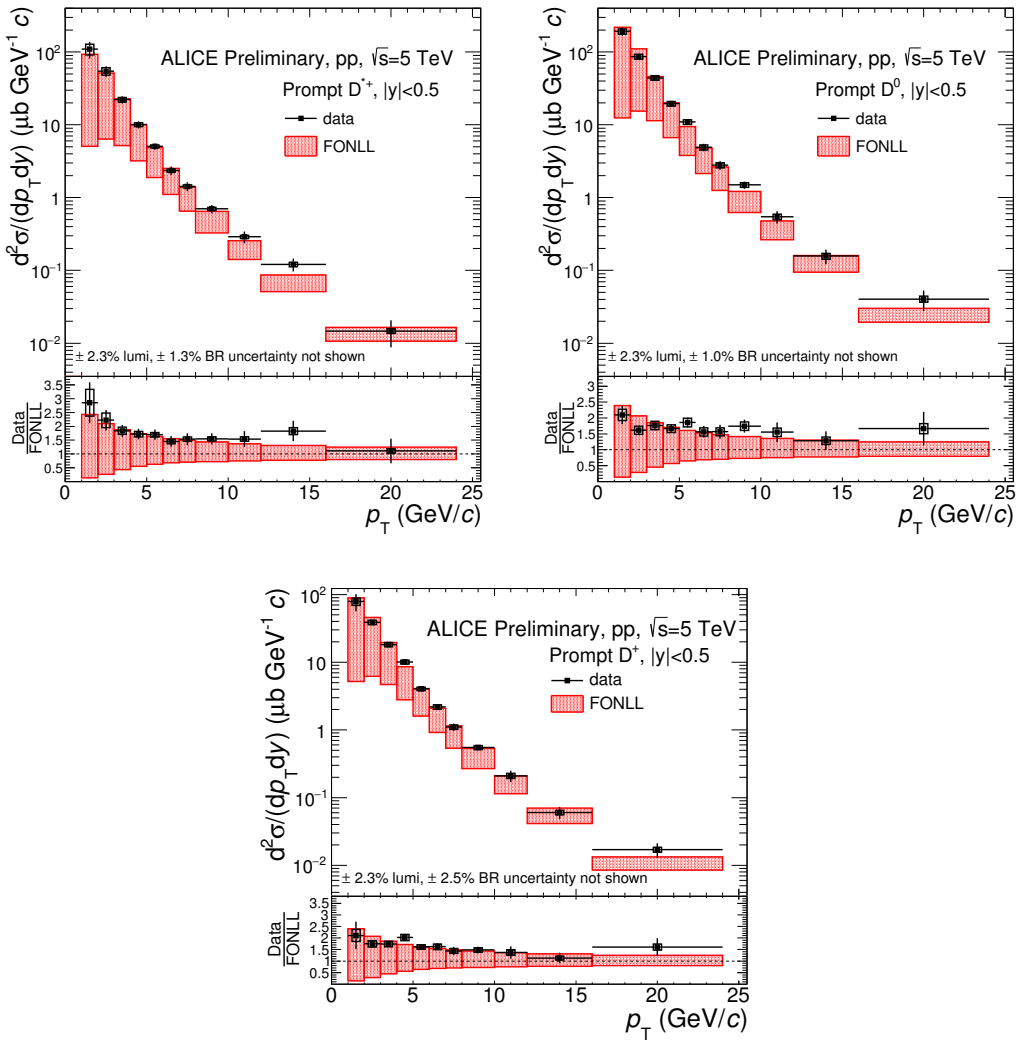

FIGURE 3.27: p_{T} inclusive production cross-section in pp collisions at $\sqrt{s} = 5$ TeV compared to FONLL calculations for the D^{*+} (top left), D^0 (top right) and D^+ (bottom) mesons. All three measurements were performed using the LHC15n data sample.

same ratio for FONLL. All checks that people in the D2H and PWG-HF groups could think of were performed, but nothing peculiar was found. As the D-meson ratios at 5 TeV, and the ratios with 8 TeV do not show this trend, it was accepted as statistical fluctuations in both the 7 TeV and 5 TeV samples. As there will be an additional long 5 TeV proton-proton run at the end of 2017, more statistics will be available. This should solve the statistical fluctuations in the 5 TeV sample, so more will be known of the nature of this trend.

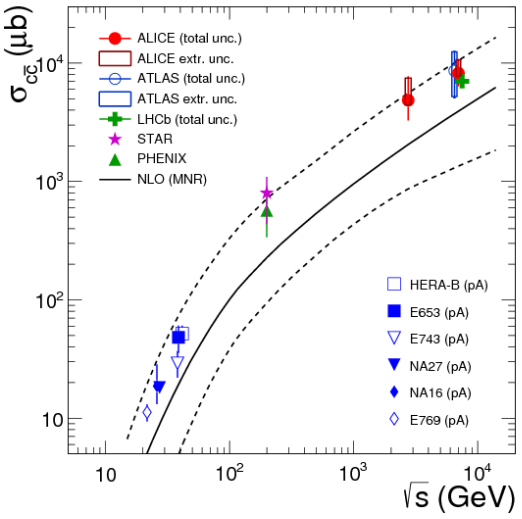

FIGURE 3.28: Total inclusive charm production cross-section in nucleon-nucleon collisions as a function of $\sqrt{s}$. Data from p-A collisions were scaled by $1/A$. The results are compared to NLO pQCD calculations [50]. Figure taken from [51].

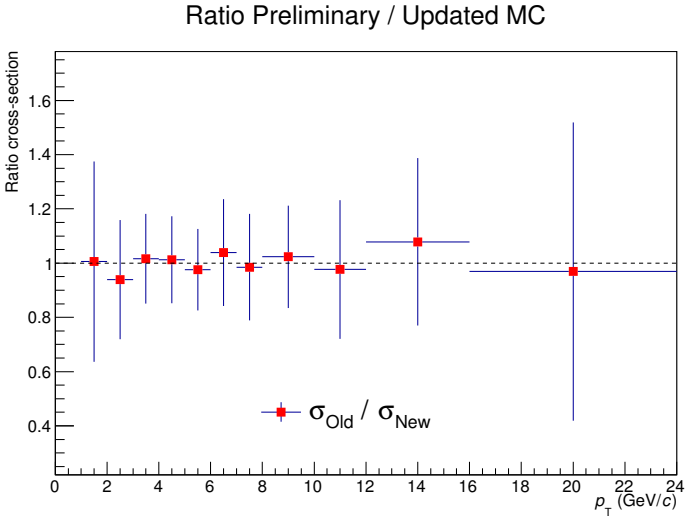

FIGURE 3.29: Ratio of the preliminary D^{*+}-meson p_{T} inclusive production cross-section in pp collisions at $\sqrt{s} = 5$ TeV versus the cross-section using the updated Monte-Carlo production after the TPC distortions fix.

Chapter 4

EPOS model calculations on open heavy-flavour correlations

As discussed in the last two chapters, heavy quarks are sensitive probes to study the dynamical properties of the quark-gluon plasma, which can be created in ultra-relativistic heavy-ion collisions. Up to now, the RHIC and LHC experiments have intensively studied "traditional" observables like the nuclear modification factor, R_{AA}, and the elliptic flow, v_2. These measurements show 1) a significant in-medium energy loss of charm and beauty quarks and 2) that charm quarks partially thermalise within the medium. However, these measurements cannot elaborate on the different energy loss mechanisms: collisional, or a combination of collisional and radiative. Besides in heavy-ion collisions, heavy quarks are good probes in proton-proton collisions to test perturbative QCD calculations on charm and beauty production.

These type of heavy-flavour observables are currently studied in multiple particle physics experiments, however their physical message remains limited. Open issues, like the in-medium energy loss mechanisms or details on the final-state radiation processes of heavy quarks, can not be answered. Therefore, theoreticians are studying new interesting observables. In this chapter, a theoretical simulation study is performed into such a new transverse momentum correlation observable between heavy-flavour particles. As discussed in section 2.3, these type of measurements hold great promise and can be feasible in experiments using Run-3 data of the LHC [23].

The study presented in this chapter is the result of an internship at Subatech in Nantes under supervision of Prof. Dr. J. Aichelin and Prof. Dr. P.B. Gossiaux. A new transverse momentum correlation observable is proposed, with as main goal to differentiate between in-medium energy loss mechanisms in heavy-ion collisions. Besides Pb-Pb collisions, this new observable is also interesting for proton-proton collisions where it will be sensitive to final-state radiation (FSR). Both systems will be discussed in this chapter. Heavy-flavour azimuthal correlations, as already studied in the light-light [52] and light-heavy sector [53], will also be shortly addressed.

The proton-proton results will be published and the paper is ready for submission. Also the heavy-ion analysis will be published, but at a later time scale.

4.1 Model description

For this analysis, the very recently updated EPOS3+HQ model [54] is used. This upgrade includes a new procedure for the heavy quarks. They are now treated just like the light flavours, produced from semi-hard pomerons. Previous studies with EPOS2+HQ [55] were using a randomly initialisation of $Q\bar{Q}$ pairs over the spatial points of initial nucleon-nucleon scatterings following the FONLL spectrum. EPOS3+HQ can also investigate the influence of a possible produced QGP in proton-proton collisions, in contrast to state-of-the-art event generators.

As it was time-wise not feasible to simulate high momentum heavy-flavour quark pairs in EPOS3+HQ[1], a comparison with one of the few heavy-flavour experimental correlation measurements available in pp was not possible. Therefore, it was chosen to do a model comparison with Pythia 6 (version 6.428 with the IBK-CTEQ5L Innsbruck tune). In this way, also different implementations of the FSR process could be studied. As the majority of LHC experiment MC simulation results (especially the very few heavy-flavour correlation measurements) are using Pythia 6 tunes, we chose to also use this relative old version. In Pythia 8, some new features were added to the FSR mechanisms, like $\gamma \to q\bar{q}$ and $\gamma \to l^+l^-$ branchings and extensions to handle bremsstrahlung in Hidden Valley models [56], but none of them are essential to this study.

In the next two subsections, technical details of both models will briefly be discussed. As the full discussion is outside the scope of this thesis, references to more detailed discussions of both models are given.

4.1.1 EPOS3+HQ

EPOS3+HQ couples the $3 + 1$ dimensional fluid dynamical evolution of the locally thermalised quark-gluon plasma, coming from the initial conditions of EPOS3 [57, 58], to MC@sHQ, the Monte-Carlo treatment of the Boltzmann equation of heavy quarks [59]. Since the recent update to EPOS3, EPOS3+HQ is an universal model for different systems. So, the same procedure for pp, p-A and A-A collisions is applied on an event-by-event procedure. The final EPOS3 simulation, including a possible produced medium, is based on the following stages:

- **Initial conditions:** The Parton-Based Gribov-Regge Theory (PBGRT) [60] is used for the multiple scattering approach. The elementary objects, so-called pomerons, are based on a DGLAP parton ladder. These parton ladders are treated in EPOS3 as classical relativistic strings.
- **Core-corona approach:** When the transverse momenta of the string segments are too large (at some early proper time τ_0), the fluid (core) is separated from the escaping hadrons (corona) [61, 62]. After this, the hydrodynamical evolution of the core is started. The corresponding energy-momentum tensor is transformed into an equilibrium one based on the assumption of a rapid equilibration.
- **Viscous hydrodynamic expansion:** Relativistic viscous hydrodynamic equations are used to evolve the core part of the system, starting from the initial

[1] An upgrade of the model to be able to only simulate high p_{T} $Q\bar{Q}$ pairs is ongoing, but will be too late for this thesis.

proper time τ_0 [62, 63]. For the shear velocity, $\eta/s = 0.08$ is taken. A cross-over equation-of-state is used, compatible with lattice QCD [64, 65].

- **Statistical hadronisation:** The thermal phase of the core ends when the hypersurface reaches the hadronisation temperature T_H (taken at the point where the energy density varies strongly with temperature) [65]. At this point, statistical hadronisation is employed to transform the "core-matter" into hadrons.
- **Final state hadronic cascade:** After the statistical hadronisation, the hadron density is still big enough to have hadronic scatterings, although these are no longer thermal. The UrQMD model [66, 67] is used to perform these hadronic scatterings until the system is too dilute. This is the end of the simulation procedure of EPOS3.

Since the upgrade to EPOS3, heavy quarks (Q) are, just like the light quarks, produced in the initial stage using the PBGRT formalism. The parton ladders are composed of two space-like parton cascades and a Born process, which both can emit time-like partons (leading to time-like cascades). In all these processes, $Q\bar{Q}$ production is possible, which means that LO+NLO production mechanisms are taken into account in EPOS3+HQ. Also the modified kinematics in case of non-zero quark masses ($m_c = 1.3$, $m_b = 4.2$ GeV/c^2 are used) are properly treated. A good agreement of D mesons in EPOS3 with available LHC data is found [68].

4.1.2 Pythia 6

The Donnachie and Landshoff parametrisation is used in Pythia 6 to calculate the total hadronic cross-section for the $AB \rightarrow$ anything process, which appears as the sum of a pomeron and a reggeon term [69]. The total cross-section consist out of an elastic, single diffractive, double diffractive and non-diffractive component. The Schuler and Sjöstrand parametrisation, based on Regge theory [70, 71], describes the first three components, where the latter is given by "whatever is left" [34]. When the process is selected, the Lund string model determines kinematic variables [72]. The default settings in Pythia do not include heavy quark masses for heavy-flavour production, however the mass can be included when one purely runs the leading-order (LO) flavour creation process.

Pythia 6 is a leading-order event generator, but it includes some approximated NLO effects like FSR and $Q\bar{Q}$ production mechanisms. The NLO flavour excitation production process for heavy quarks is approximated by partly treating it as initial-state radiation (ISR).[2] As the ISR has to be tuned rather high in Pythia to reproduce LHC data, it is known that Pythia (in both version 6 and 8) has problems reproducing $Q\bar{Q}$ azimuthal correlations [73–75]. It was therefore chosen to purely simulate LO $Q\bar{Q}$ flavour creation processes. A proper NLO treatment, as performed in Ref. [75], is left for future work. Note that other NLO processes, like ISR and FSR, are still included in the simulations.

By applying a back-to-back selection of heavy-flavour particles, which is mostly sensitive to the LO order production mechanisms, it is made sure that the results of Pythia can be compared to the LO+NLO order heavy-flavour production of EPOS3+HQ. In Ref. [75], it can already be seen that a proper LO+NLO treatment of Pythia 6 will not change the results of the back-to-back heavy-flavour selection a lot.

[2] In the flavour excitation process one heavy quark is kicked out of the proton, where its partner quark stays near beam rapidity.

4.2 Theory

The transverse momentum correlation observable, that is proposed later, will be sensitive to mechanisms that distort the momenta of the two heavy quarks independent of each other. The main contributors to this smearing are final-state radiation and interactions with medium particles. FSR will occur in both pp and Pb-Pb systems, where in-medium interactions will (mostly) occur in heavy-ion collisions. A theoretical background behind both mechanisms, and their modelling, will be given in this section.

4.2.1 Final-state radiation

Initial- and final-state radiation are important to be taken into account for all processes that contain particles with colour and/or charge. For initial-state radiation, one of the incoming particles emit radiation, while for final-state radiation, the radiation is emitted by the scattered particles. Here, the final-state radiation of colour charged particles, so the emissions of gluons, will be discussed, which is an important process at LHC energies. As our proposed observable will be sensitive to final-state radiation, it can help to improve our understanding of these processes and fix issues in its implementation in event generators, which will indirectly lead to a better understanding of the LHC data.

The matrix elements for simple FSR cases like $e^- e^+ \rightarrow \gamma^*/Z^0 \rightarrow q\bar{q}g$ can still be calculated analytically. However, this is not the case for most of the QCD processes. Here, calculations are limited to parton shower approaches in MC event generators. The modelling of these showers is based on Monte-Carlo algorithms of the DGLAP equations [76–78]. This description gives the probability for a parton to branch using a probabilistic approximation. Although this approach is state-of-the-art in the current event generators, quantitative differences arise between the models as there are still open questions in the DGLAP implementation.

The DGLAP equations are based on the assumption that the cross-section of a process that emits $n+1$ partons, σ_{n+1}, can be factorised into the cross-section σ_n and a splitting function P. This splitting function P gives the probability that one of the n partons splits into two daughter particles. They can be calculated using standard leading-order DGLAP splitting kernels [76–78]:

$$\begin{aligned} P_{q\rightarrow qg}(z) &= \frac{4}{3}\frac{1+z^2}{1-z}, \\ P_{g\rightarrow gg}(z) &= 3\frac{(1-z(1-z))^2}{z(1-z)}, \\ P_{g\rightarrow q\bar{q}}(z) &= \frac{1}{2}(z^2+(1-z)^2), \end{aligned} \tag{4.1}$$

where z is the energy fraction of the daughter partons (one parton is taking the fraction z, where the other one takes a fraction $1-z$). The probability for a parton a to branch, $\mathcal{P}_a$, can then be written as

$$\mathrm{d}\mathcal{P}_a = \sum_{b,c} \frac{\alpha_{abc}}{2\pi} P_{a\rightarrow bc}(z)\mathrm{d}t\mathrm{d}z, \tag{4.2}$$

where the sum runs over all allowed branchings. The α_{abc} factor can differ between the QED and QCD coupling constant, depending on the type of branching. The time t is defined in terms of the virtuality scale Q^2, which is a property of each incoming parton:

$$t = \ln\left(Q^2/\Lambda^2_{\mathrm{QCD}}\right) \quad \Rightarrow \quad \mathrm{d}t = \mathrm{d}\ln\left(Q^2\right) = \frac{\mathrm{d}Q^2}{Q^2}. \tag{4.3}$$

The properties of the incoming parton, especially its virtuality, determine the behaviour of the simulated parton showers in MC event generators. These initial values for Q^2 are increasing for initial- and decreasing for final-state showers. Equation 4.2 therefore gives the probability that during such a change $\mathrm{d}Q^2$, the parton splits into two daughters. To obtain the final probability that a parton branches at a specific virtuality, the branching probability needs to be multiplied with the probability that it does not split at a higher virtuality. This is given by the Sudakov factor $S(Q_{\mathrm{max}}, Q)$, that besides the virtuality also depends on a fixed maximum virtuality Q_{max}. This maximum scale is used as upper limit in the integral of the Sudakov factor. There are no clear guidelines for the choice of Q_{max}, but the decision can strongly affect the amount of well-separated jets [79].

The parton shower terminates when all produced partons have a virtuality that is lower or higher than a certain cut-off parameter. Such a cut-off can be motivated as the transition from perturbative splitting processes to the hadronisation process for final-state radiation. This cut-off parameter is event generator dependent. Also the choice for the shower evolution variable, Q^2, in FSR showers is not unique. It can be chosen to relate the virtuality with m^2 of the branching (time-like) parton, but another often used possibility are $p_\perp$-ordered showers.

In addition to this three differences in event generators, a running coupling constant α_s and the modelling of the Landau Pomerachuck Migdal (LPM) effect can affect the final-state radiation process. Due to the LPM effect, the number of branchings is reduced as subsequent gluon emissions are not independent processes. The next gluon can only be emitted after some formation time t_f of the former one [80, 81].

4.2.2 In-medium energy loss mechanisms

As heavy quarks are excellent probes to study the QGP, it is crucial to know how they lose energy while interacting with the QCD medium constituents. This interaction can be split into two main contributors: collisional energy loss [82–84] and radiative energy loss [85, 86]. If the in-medium interactions of heavy quarks are purely collisional, or a combination of collisional and radiative is not yet known. In the latter case, it is also not clear what will be the dominant mechanism, although usually one argues that collisional energy loss is dominant at low energies because the radiation phase space is restricted by the dead-cone effect [87].

At the moment, there are many theoretical models which are able to describe the R_{AA} and/or v_2 by simulations of the heavy quark inside the medium. There are purely elastic models [59], purely radiative [88], a combination of both [89] or non-perturbative approaches [90]. And then there are also differences in the mathematical description, for example the collisional energy loss can be described using a Boltzmann or Langevin equation [59, 91]. As in this study the EPOS3+HQ model is used to describe the QGP, only these approaches for both energy loss mechanisms will be discussed.

4.2.2.1 Collisional energy loss

In contrast to most of the theoretical approaches, EPOS3+HQ is using a Boltzmann equation instead of a Fokker-Planck approach to describe the time evolution of the heavy quark distribution. Collisional energy loss is a purely elastic processes coming from $Q + q \rightarrow Q' + q'$ and $Q + g \rightarrow Q' + g'$. The rate of these processes for a heavy quark Q in a fluid cell at rest can be written as

$$R_i = \frac{1}{p_0} \int \frac{\mathrm{d}^3 k}{(2\pi)^3} n_i(k) \frac{p \cdot k}{k^0} \int \mathrm{d}t \frac{\mathrm{d}\sigma_{i,2\rightarrow 2}}{\mathrm{d}t} \,, \tag{4.4}$$

where p and k are the four-momenta of the incoming heavy quark and light quark or gluon, respectively. The thermal distribution of the light quarks or gluons is given by $n_i(k)$, which is taken as a Boltzmann type in EPOS3+HQ [55]. The last term, $\mathrm{d}\sigma_{i,2\rightarrow 2}/\mathrm{d}t$, is the differential cross-section calculated using matrix elements for these elastic channels.

To obtain finite cross-sections, the matrix elements are fixed in two ways in EPOS3+HQ. First of all, a so-called HTL-semihard approach is used as an IR regulator, which adds a gluon self energy to the bare gluon propagator. In this way, the calculations are justified for both small and large values of the Mandelstam variable $|t|$. Secondly, a running coupling constant is used. Although it is implemented in a rigorous way extracting results from experiments, it improves the fixed-coupling pQCD calculations. More details on the collisional energy loss mechanism can be found in Refs. [55, 59].

4.2.2.2 Radiative energy loss

Several calculations of radiative energy loss exist for massless quarks [87, 92, 93], where some of them have been extended to heavy quarks. These approaches are based on the eikonal limit. This limit assumes that the formation time of the radiated gluon is large compared to the mean-free path. So, multiple "collisions" with the medium particles contribute to the radiation of one gluon.

The radiative energy loss mechanism of EPOS3+HQ, explained in detail in Refs. [89, 94], adopt a different approach based on the calculations of Ref. [95]. Using the heavy quark mass as regulator, the cross-section for $Q + q \rightarrow Q' + q' + g$ and $Q + g \rightarrow Q + g' + g''$ is approximated as

$$\frac{\mathrm{d}\sigma^{Qq\rightarrow Qgq}}{\mathrm{d}x \mathrm{d}^2 k_t \mathrm{d}^2 l_t} \simeq \frac{1}{\pi} \frac{\mathrm{d}\sigma_{\mathrm{el}}}{\mathrm{d}t} P_g(x, \vec{k_t}, \vec{l_t}) \Theta(\Delta) \,, \tag{4.5}$$

where l_t is the momentum transfer induced by the light parton, k_t the transverse momentum of the radiated gluon and x the momentum fraction. $\Theta(\Delta)$ is a phase-space condition, P_g a radiation factor as calculated in Ref. [95] and $\mathrm{d}\sigma_{\mathrm{el}}/\mathrm{d}t$ the elastic differential cross-section.

As is common for energy loss models, the obtained scattering rates need to be rescaled with a factor to compare the results to experimental data. This can be motivated as a description for unimplemented effects like medium expansion or cold nuclear matter effects. With a factor $K = 1.5$ for purely collisional and $K = 0.8$ for collisional+radiative, the models are able to describe both the R_{AA} and v_2 measured at the LHC.

4.3 A new correlation observable

For this new correlation observable, we consider the transverse momentum of the $c\bar{c}$ and $b\bar{b}$ pairs and their corresponding heavy-flavour mesons. For the following discussion, we take $c\bar{c}$ as an example, but the same strategy is employed for all cases.

First of all, all possible $c\bar{c}$ combinations in an event are formed.[3] This strategy is not unique. Another possibility is to use a trigger particle, which is employed for azimuthal correlations in the light-flavour sector. One can also make use of an additional p_{T} cut, to make only high momenta combinations. But, as this is the first study into this observable, we decided to focus on the full sample of pairs.

On this full sample, an azimuthal selection is employed: we concentrate on pairs which are observed back-to-back, with a difference in the azimuthal angle of $\Delta\phi > 3/4\pi$. As discussed before, this azimuthal selection is needed to compare LO+NLO $Q\bar{Q}$ production in EPOS3+HQ with only LO in Pythia 6. Besides this reason, also the largest correlation is expected for back-to-back pairs.

A $(p_{\mathrm{T}}, p_{\mathrm{T}}{}')$-lattice displays the transverse momenta of all selected pair combinations in a sample, where p_{T} and $p_{\mathrm{T}}{}'$ are for the c and $\bar{c}$ quark respectively. From this lattice, a 2-dimensional correlation function (independent of the grid size) is calculated, which is projected on the diagonal $\Delta p_{\mathrm{T}} = p_{\mathrm{T}} - p_{\mathrm{T}}{}'$ line for a specific $p_{\mathrm{T}} + p_{\mathrm{T}}{}'$ interval. This 1-dimensional projection is the final observable and will be compared for the different models. For the beauty sector we studied the range $10 < p_{\mathrm{T}} + p_{\mathrm{T}}{}' < 14$ GeV/c and for charm the range $6 < p_{\mathrm{T}} + p_{\mathrm{T}}{}' < 10$ GeV/c, which are high enough to not select quarks that are thermalised with the medium. In Figure 4.1, the 2-dimensional correlation function $C_R(p_{\mathrm{T}}, p_{\mathrm{T}}{}')$ for $c\bar{c}$ pairs in pp collisions at $\sqrt{s} = 5.02$ TeV in Pythia 6 is displayed as an example. The black lines indicate the diagonal band for the projection.

[3] In some plots only the real pairs (so coming from the same vertex) will be studied. This will be clearly noted, as these results (without combinatorial background) can obviously not be compared to experiments.

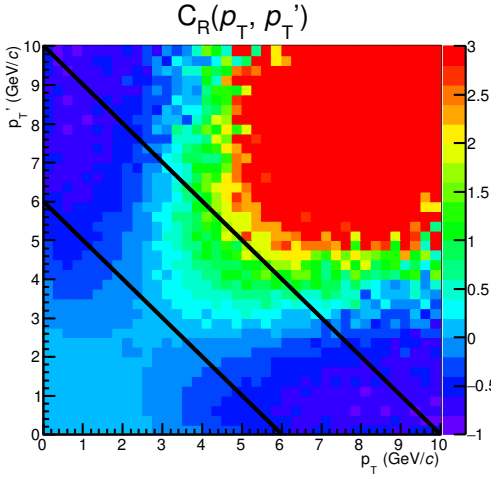

FIGURE 4.1: Two-dimensional correlation function $C_R(p_{\mathrm{T}}, p_{\mathrm{T}}{}')$ for $c\bar{c}$ pairs in pp collisions at $\sqrt{s} = 5.02$ TeV in Pythia 6. Note that the maximum in the plot is set to 3 to have a reasonable colour scale.

The calculation of the 2-dimensional correlation function $C_R(p_T, p_T')$ is based on the fact that each two-dimensional function can be written as the product of two one-dimensional functions times a correlation function. First of all, we build the equivalent probability distribution:

$$p(p_T, p_T') = \frac{N(p_T, p_T')}{\Delta p^2 \sum_{p_T, p_T'} N(p_T, p_T')}\,, \tag{4.6}$$

where $N(p_T, p_T')$ is the average number of counts in a (p_T, p_T')-cell and Δp^2 the grid size. The reduced probability distribution, which is basically a projection of the histogram on one of the two axis, is then given by:

$$p_R(p_T) = \Delta p \sum_{p_T'} p(p_T, p_T')\,, \tag{4.7}$$

which satisfies $\Delta p \sum_{p_T} p_R(p_T) = 1$. Now, the absolute correlation

$$C(p_T, p_T') = p(p_T, p_T') - p_R(p_T) p_R(p_T')\,, \tag{4.8}$$

which is normalised to zero, and the relative correlation $C_R(p_T, p_T')$ can be build:

$$C_R(p_T, p_T') = \frac{C(p_T, p_T')}{p_R(p_T) p_R(p_T')}\,. \tag{4.9}$$

Both objects vanish in the absence of a correlation and are independent of the grid size (when Δp is small enough and the statistics are large enough). Note that using this method, the final correlation can be larger than one. In the next subsection, theoretical toy model studies are performed to study the properties of this new observable in case of strong and weakly correlated variables.

4.3.1 Toy model studies

As the final values of $C_R(p_T, p_T')$ can vary between -1 and infinity, it is hard to get a feeling of the final correlation between both transverse momenta. So, to study what a typical correlation value says, two theoretical toy models with strong and weakly correlated variables are implemented. These will be discussed in the next two subsections, but first of all, a simple version of the strong correlation toy model is presented. Since this toy model is using the same framework as in which the final results will be presented, it will help for a better understanding of the plots presented in the next section.

In this toy model, the found maximum values of $C_{R,\text{final}}(p_T, p_T')$ are related to the widths of an initial Gaussian correlation, $C_{R,\text{initial}}(p_T, p_T')$, distributed around $\Delta p_T = p_T - p_T' = 0$. Starting from this initial correlation, the corresponding two-dimensional density function is filled using a finite number of MC trials assuming

$$N(p_T, p_T') = N(p_T) N(p_T') C_{R,\text{initial}}(p_T, p_T') \tag{4.10}$$

with $N(p_T) = 1/(1+p_T)^4$. The $C_{R,\text{final}}$ distributions and projections are calculated with the same function as used for the real results. The four stages of this procedure are shown in Figure 4.2. The final relation between the observed maximum correlation value and the initial Gaussian width is shown in Figure 4.3. The uncertainty is calculated using the envelope of simulations with different number of MC trials (50k, 100k and 200k events).

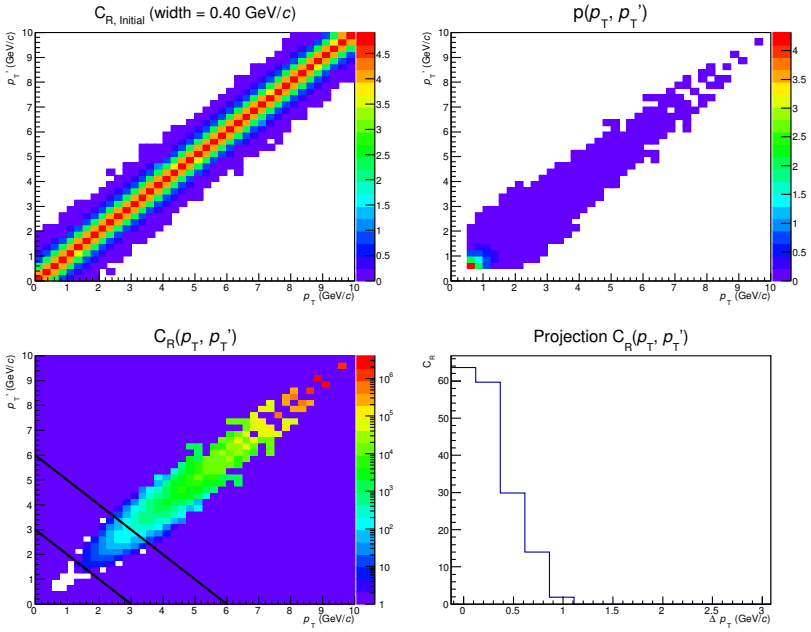

FIGURE 4.2: Four stages of the Gaussian toy model with a width of 400 MeV/c and 2 million simulated events. The initial Gaussian C_R distribution is shown on the top left, from which the MC simulated $p(p_\mathrm{T}, p_\mathrm{T}')$ (top right), $C_R(p_\mathrm{T}, p_\mathrm{T}')$ (bottom left) and its projection (bottom right) follow.

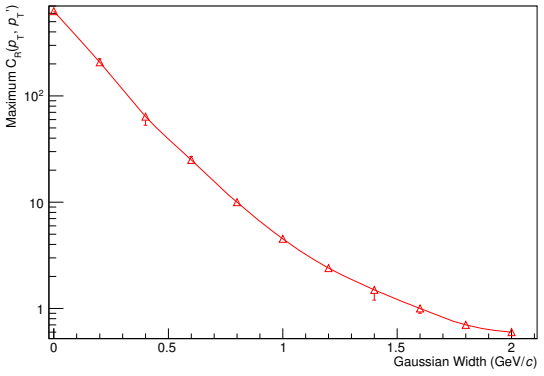

FIGURE 4.3: Relation between the width of the initial Gaussian correlation $C_{R,\mathrm{initial}}$ and the final maximum value of the projection of $C_{R,\mathrm{final}}$. The error bars are calculated as the envelope of simulations with different number of MC trials.

Note that for an infinitesimal small lattice, a zero Gaussian width will be related to a maximum of infinity.

4.3.1.1 Strongly correlated variables

The toy model discussed in this subsection is basically an extended version of the simple toy model shown in the Figures 4.2 and 4.3. These results will have a different layout as this toy model is made in Mathematica. Also, the projection method is a bit different, where a line ($p_\mathrm{T} + p_\mathrm{T}' = 8$ GeV/c) is used instead of a transverse momentum band.

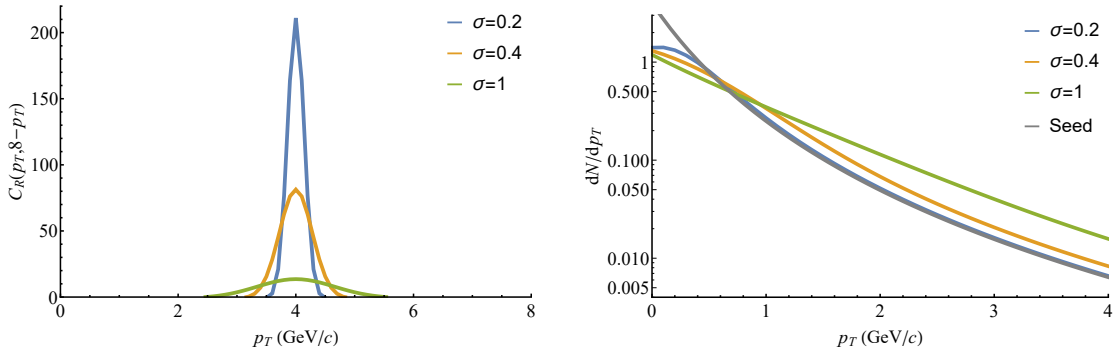

FIGURE 4.4: Left: Calculation of $C_R(p_\mathrm{T}, 8 - p_\mathrm{T})$ for the strongly correlation variable model of equation 4.11. The lines correspond to $\sigma = 0.2$, 0.4 and 1.0 with $n = 4$. Right: Calculation of the normalised one-body distribution, $\mathrm{d}N/\mathrm{d}p_\mathrm{T}$, for the strongly correlation model with the same settings.

If one assumes that p_T and p_T' are generated via a process that first leads to a common value and then some difference appear, a good model is

$$\frac{\mathrm{d}^2N^{\mathrm{strong}}(p_\mathrm{T}, p_\mathrm{T}')}{\mathrm{d}p_\mathrm{T}\mathrm{d}p_\mathrm{T}'} \propto \frac{1}{(1+\frac{p_\mathrm{T}+p_\mathrm{T}'}{2})^n} \times \frac{\exp[\frac{(p_\mathrm{T}-p_\mathrm{T}')^2}{-2\sigma^2}]}{\sigma}\,, \tag{4.11}$$

where n and σ are free parameters that define the strength of the correlation. If the NLO corrections are small, so $\sigma \to 0$, this model is a priori a good one. To derive the associated $p_R(p_\mathrm{T})$ ($\propto \mathrm{d}N(p_\mathrm{T})/\mathrm{d}p_\mathrm{T}$), one has to numerically integrate equation 4.11.

The projection of C_R is shown in the left panel of Figure 4.4 for $n = 4$ and $\sigma = 0.2$, 0.4 and 1. As expected, a larger σ corresponds to smaller maximal values at the origin ($p_\mathrm{T} = 4$ GeV/c). One recovers the ordering associated to the σ parameter. The amplitude is determined by the behaviour of p_R. The results of the numerical integration are shown in the right panel of Figure 4.4. For small σ, p_R is close to the seed spectrum (which is chosen as $1/(1+p_\mathrm{T})^4$), so the correlation of equation 4.9 can be simplified to:

$$\begin{aligned} C_R(p_\mathrm{T}, p_\mathrm{T}') &= \frac{\frac{\mathrm{d}^2N^{\mathrm{strong}}}{\mathrm{d}p_\mathrm{T}\mathrm{d}p_\mathrm{T}'}}{\int \mathrm{d}p_\mathrm{T} \frac{\mathrm{d}^2N^{\mathrm{strong}}}{\mathrm{d}p_\mathrm{T}\mathrm{d}p_\mathrm{T}'} \times \int \mathrm{d}p_\mathrm{T}' \frac{\mathrm{d}^2N^{\mathrm{strong}}}{\mathrm{d}p_\mathrm{T}\mathrm{d}p_\mathrm{T}'}} - 1 \\ &\approx \frac{G}{p_R(p_\mathrm{T})} - 1 \qquad \text{with} \qquad G = \frac{\exp[\frac{(p_\mathrm{T}-p_\mathrm{T}')^2}{-2\sigma^2}]}{\sigma}\,. \end{aligned} \tag{4.12}$$

So, the law defining the indicator C_R absorbs a p_R^{-1} factor for a strong correlation, hence the large values. For larger values of σ, smaller values of p_T for a given p_T' can be explored. So, p_R becomes larger and the C_R decreases.

4.3.1.2 Weakly correlated variables

For the weakly correlated variable toy model, we start from a completely uncorrelated two-particles distribution

$$\frac{\mathrm{d}^2N^{\mathrm{unc}}}{\mathrm{d}p_\mathrm{T}\mathrm{d}p_\mathrm{T}'} \propto \frac{1}{(1+p_\mathrm{T})^n} \times \frac{1}{(1+p_\mathrm{T}')^n}, \tag{4.13}$$

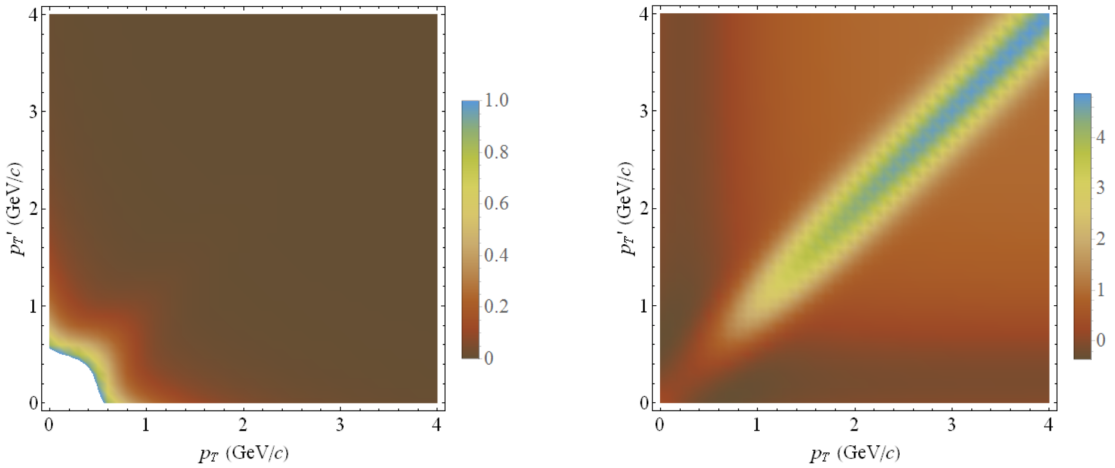

FIGURE 4.5: Distribution for $\frac{\mathrm{d}^2N^{\mathrm{weak}}}{\mathrm{d}p_{\mathrm{T}}\mathrm{d}p_{\mathrm{T}}'}$ (left) and the corresponding correlation function C_R (right) for the weak correlation toy model. The parameters are: $n = 4$, $\sigma = 0.2$ and $a = 0.5$. The colour scale of the left plot has a maximum at 1.0, hence the white area.

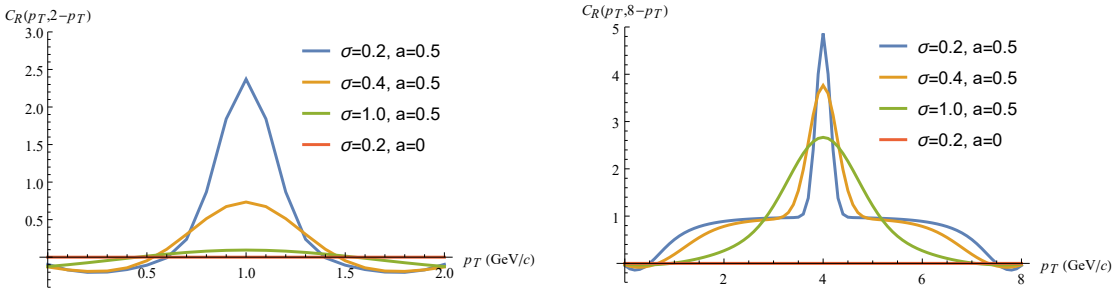

FIGURE 4.6: Calculation of $C_R(p_{\mathrm{T}}, 2 - p_{\mathrm{T}})$ (left) and $C_R(p_{\mathrm{T}}, 8 - p_{\mathrm{T}})$ (right) for the weakly correlation variable model of equation 4.14 with different widths. A reference with no correlation, so $a = 0$, is also shown in both plots.

to which a small correlation is added

$$\frac{\mathrm{d}^2N^{\mathrm{weak}}}{\mathrm{d}p_{\mathrm{T}}\mathrm{d}p_{\mathrm{T}}'} \propto \frac{1}{(1+p_{\mathrm{T}})^n} \times \frac{1}{(1+p_{\mathrm{T}}')^n} \times \left[1 + a \times C_2(p_{\mathrm{T}} - p_{\mathrm{T}}')\right]. \tag{4.14}$$

Here, a is the absolute magnitude of the correlation (between 0 and 1) and $C_2 = c_0 \cdot G - 1$. The variable G is similar as defined in equation 4.12 and $c_0(\sigma, n)$ is evaluated such that

$$\iint \mathrm{d}p_{\mathrm{T}}\mathrm{d}p_{\mathrm{T}}' \frac{1}{(1+p_{\mathrm{T}})^n} \times \frac{1}{(1+p_{\mathrm{T}}')^n} \times C_2(p_{\mathrm{T}} - p_{\mathrm{T}}') = 0\,. \tag{4.15}$$

In Figure 4.5, the 2-dimensional particle distribution function and the corresponding correlation C_R are shown for the weak correlation variable toy model. In the density plot, the correlation is not that obvious, but it appears nicely in the distribution of C_R. Projections along the line $p_{\mathrm{T}} + p_{\mathrm{T}}' = 2$ and 8 can be found in Figure 4.6. When there is no correlation, so $a = 0$, one obtains $C_R = 0$ as expected.

For $C_R(p_{\mathrm{T}}, 2 - p_{\mathrm{T}})$, so at small p_{T}, the correlation appears as one naturally expects with $p_R(p_{\mathrm{T}}) \propto \frac{1}{(1+p_{\mathrm{T}})^n}$ and $C_R \approx aC_2$. For larger momenta and small values for σ, so the right panel of Figure 4.6, $p_R(p_{\mathrm{T}})$ is no longer proportional to $\frac{1}{(1+p_{\mathrm{T}})^n}$ and some kind of pedestal is observed.

4.4 Results

In this section, the results for both the proton-proton analysis into final-state radiation and the Pb-Pb analysis into the different energy loss mechanisms are presented. In total, there are seven EPOS3+HQ samples at $\sqrt{s_{\mathrm{NN}}} = 5.02$ TeV: one pp sample and six Pb-Pb samples in the 0-10%, 30-50% and 50-70% centrality class for both collisional and collisional+radiative energy loss. There are two stages at quark level in these samples, called "Initial" and "Final", corresponding respectively to the quarks before the interaction with a possible quark-gluon plasma and to the quarks just before hadronisation. So, when no QGP is produced, the properties of the quarks in both stages will be the same. For Pythia 6 there is only one stage at quark level, which compares to the initial stage in EPOS3+HQ (so after processes like final-state radiation).

For the meson-meson correlations, we are analysing prompt D^+, D^-, D^0 and $\overline{\mathrm{D}^0}$ mesons (similar for the B mesons). We are aware of the experimental difficulties to measure two fully reconstructed heavy mesons in one event, so we also (partly) studied heavy-flavour leptonic correlations using a weak decay according to a measurement of the BaBar Collaboration for the B mesons [96]. Only a few of these results are, however, shown here because the leptonic decay will only introduce an additional transverse momentum smearing.

4.4.1 Proton-proton collisions

In this subsection, the results for the proton-proton study into final-state radiation at $\sqrt{s} = 5.02$ TeV in both EPOS3+HQ and Pythia 6 are presented. It was chosen for this energy because there exist pp, p-Pb and Pb-Pb LHC data at this energy. So, besides for this study, the results can also be used as reference for heavy-ion analyses. It was checked that the physical message does not change when the energy is increased to $\sqrt{s} = 7$ or 13 TeV.

The results at both quark and meson level will be shown, because the physical picture of the final-state radiation is most clear at the quark stage, while experiments can only measure mesons. By looking at the correlations for the corresponding mesons, the additional effect of the fragmentation process is also studied[4]. As the Peterson function for charm does not peak at large $x = p/p_{\mathrm{max}}$, which is the case for beauty quark fragmentation [97], information about the initial transverse momentum correlation will be lost more in the charm sector when moving to the final-state mesons.

4.4.1.1 Azimuthal correlations

In this analysis, a back-to-back selection on the difference in azimuthal angle is applied ($\Delta\phi > 3/4\pi$). As argued before, this is an important cut to compare the results of LO+NLO $Q\bar{Q}$ production in EPOS3+HQ with only LO in Pythia 6. The differences between both models are visible in Figure 4.7, where the $\Delta\phi(b, \bar{b})$ and $\Delta\phi(\mathrm{D}, \bar{\mathrm{D}})$ distributions are shown.

[4]Both models are using a string fragmentation model.

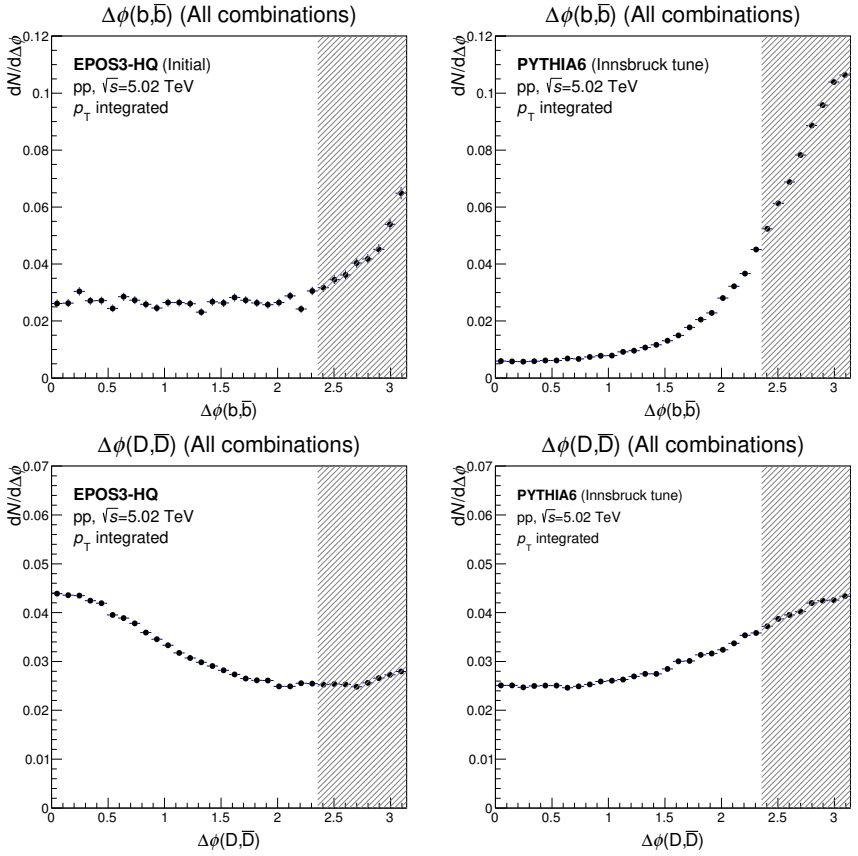

FIGURE 4.7: Azimuthal angular distribution for all $b\bar{b}$ (top) and prompt D$\overline{\text{D}}$ (bottom) combinations in p_{T} integrated pp collisions at $\sqrt{s} = 5.02$ TeV for EPOS3+HQ (left) and Pythia 6 (right). The shaded band indicates the back-to-back selection cut. All distributions are normalised to one.

In both EPOS3+HQ and Pythia 6 an increase at $\Delta\phi = \pi$ is observed for the beauty quarks. So in EPOS3+HQ, the LO production mechanisms for beauty are still dominant over the NLO contribution, where in Pythia 6 the peak is relatively large because of the lack of NLO production processes. Using the back-to-back selection (shaded area), we make sure we are mostly selecting LO flavour creation production processes. The combinatorial background, so $b\bar{b}$ pairs that do not originate from the same vertex in proton-proton collisions, is negligible. Only in 0.9% of the beauty events, two $b\bar{b}$ pairs were produced. The initial EPOS3+HQ distribution is shown, but differences with the final distribution for quarks are minimal, as the probability to produce a medium in pp collisions is low.

In contrast to the beauty sector, the $\Delta\phi(\text{D}, \bar{\text{D}})$ distributions for EPOS3+HQ and Pythia 6 differ quite a lot. The difference between LO and LO+NLO order $Q\bar{Q}$ production mechanisms is clearly visible. For EPOS3+HQ, the NLO processes, like gluon splitting, are dominant, which lead to the peak observed at $\Delta\phi(\text{D}, \bar{\text{D}}) = 0$. For Pythia 6, the leading-order peak at $\Delta\phi(\text{D}, \bar{\text{D}}) = \pi$ is still observed. Because charm quarks are produced more often in proton-proton collisions than beauty quarks, the combinatorial background is more important here.

Although not shown here[5], the difference between $\Delta\phi(c,\bar{c})$ at the initial and final levels of EPOS3+HQ is very small. The initial and final distributions agree within statistical uncertainties, so the effect of a possible QGP on the difference in azimuthal angle is negligible. As we will see in the next subsection, the transverse momentum correlations are affected more.

4.4.1.2 Transverse momentum correlations

In Figure 4.1, an example of the 2-dimensional $C_R(p_\mathrm{T}, p_\mathrm{T}')$ function was shown. This correlation function is projected on the diagonal Δp_T line for a specific p_T range. Diagonal p_T bands of $6 < p_\mathrm{T} + p_\mathrm{T}' < 10$ GeV/c and $10 < p_\mathrm{T} + p_\mathrm{T}' < 14$ GeV/c are used for respectively charm and beauty. These bands are relative large in order to have sufficient statistics. The results for EPOS3+HQ and Pythia 6 are illustrated in Figure 4.8, 4.9 and 4.10 for $b\bar{b}$, $c\bar{c}$ and prompt D$\bar{\mathrm{D}}$ pairs, respectively.

In the left panel of Figure 4.8, which shows the $C_R(p_\mathrm{T}, p_\mathrm{T}')$ of the selected $b\bar{b}$ pairs, a clear transverse momentum correlation at $\Delta p_\mathrm{T} = 0$ is visible after final-state radiation. With in-medium interactions included (middle panel), this maximal correlation value is smeared out, which is expected as collisions with medium particles will change the p_T of the quarks independent of each other. Although the peak value decreases, the overall shape at $\Delta p_\mathrm{T} > 0$ stays the same when switching from the initial to the final EPOS3+HQ stage. One has to note that, as on average the heavy quarks lose more energy than they obtain after interactions with a medium, the final sample will be slightly smaller than the initial EPOS3+HQ sample. The projection for Pythia 6 (shown in the right panel) does not show a clear correlation at $\Delta p_\mathrm{T} = 0$. The transverse momentum correlations at meson level could not be studied for beauty in the pp sample of EPOS3+HQ, but as the Peterson function for beauty peaks at large values, similar distributions as for the quarks are expected.

As we can see in the left panel of Figure 4.9, also for $c\bar{c}$ pairs a clear transverse momentum correlation at $\Delta p_\mathrm{T} = 0$ is visible at the initial stage. However, the maximal correlation is smaller than for $b\bar{b}$ pairs. At the final EPOS3+HQ stage shown in the middle panel, so with interactions with a possible quark-gluon plasma included, again a decrease of the $p_\mathrm{T} = p_\mathrm{T}'$ symmetry is observed. Just like for the beauty quarks, the overall shape at $\Delta p_\mathrm{T} > 0$ stays similar.

The projection of the transverse momentum correlation of $c\bar{c}$ pairs for Pythia 6 is shown in the right panel of Figure 4.9. This plot should be compared with the initial EPOS3+HQ distribution, as both do not include in-medium interactions. The distribution for Pythia 6 does not show a clear correlation between p_T and p_T'. Besides the different maximal correlation values, Pythia 6 and EPOS3+HQ also differ at larger Δp_T. Where the distribution for Pythia 6 keeps decreasing, EPOS3+HQ stays almost flat. This is also the case for $b\bar{b}$ pairs.

Figure 4.10 shows the transverse momentum correlation for the final-state D mesons, as experiments can obviously not measure bare quark correlations. Note that here is only one stage for EPOS3+HQ, which includes the in-medium interactions. The fragmentation process of the charm quarks broadens the peak at small values of Δp_T.

[5]The $\Delta\phi(c,\bar{c})$ distribution looks very similar as $\Delta\phi(\mathrm{D},\bar{\mathrm{D}})$ shown in Figure 4.7.

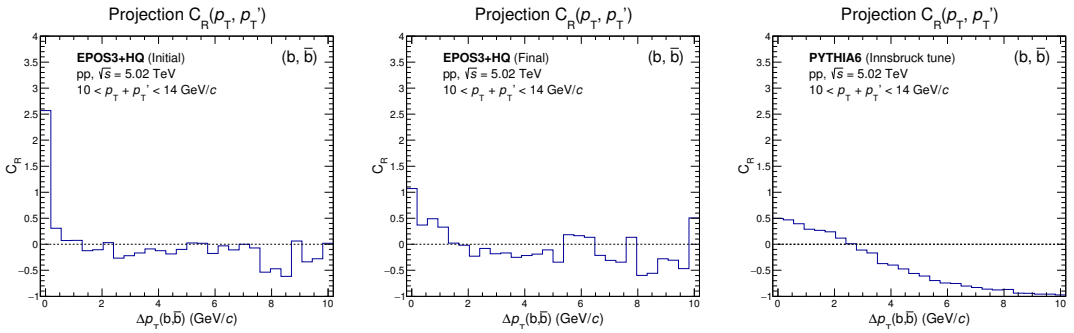

FIGURE 4.8: Projections of the transverse momentum correlation function $C_R(p_\mathrm{T}, p_\mathrm{T}')$ for $b\bar{b}$ pairs with $\Delta\phi > 3/4\pi$ for EPOS3+HQ initial (left), EPOS3+HQ final (middle) and Pythia 6 (right) in the p_T band: $10 < p_\mathrm{T} + p_\mathrm{T}' < 14$ GeV/c.

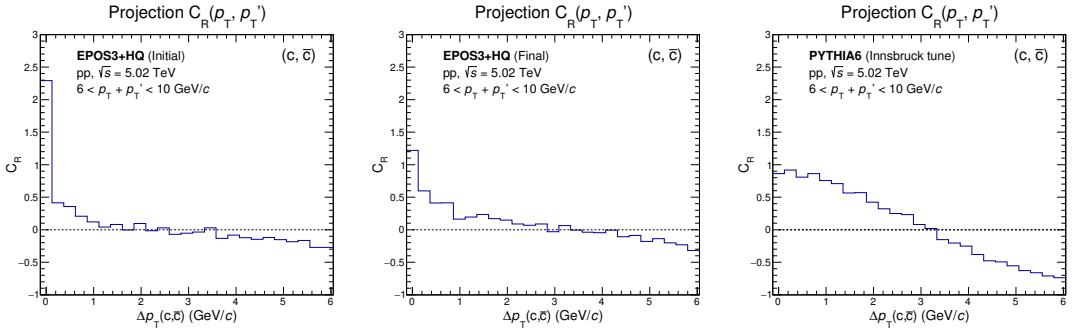

FIGURE 4.9: Projections of the transverse momentum correlation function $C_R(p_\mathrm{T}, p_\mathrm{T}')$ for $c\bar{c}$ pairs with $\Delta\phi > 3/4\pi$ for EPOS3+HQ initial (left), EPOS3+HQ final (middle) and Pythia 6 (right) in the p_T band: $6 < p_\mathrm{T} + p_\mathrm{T}' < 10$ GeV/c.

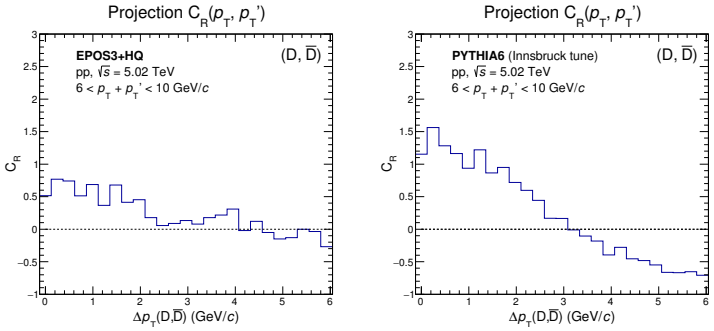

FIGURE 4.10: Projections of the transverse momentum correlation function $C_R(p_\mathrm{T}, p_\mathrm{T}')$ for prompt D$\overline{\mathrm{D}}$ pairs with $\Delta\phi > 3/4\pi$ for EPOS3+HQ (left) and Pythia 6 (right) in the p_T band: $6 < p_\mathrm{T} + p_\mathrm{T}' < 10$ GeV/c.

For both models, the overall shape at $\Delta p_\mathrm{T} > 0$ is similar for $c\bar{c}$ and D$\overline{\mathrm{D}}$. A clear difference in both distributions, as observed for $c\bar{c}$ pairs, is still visible.

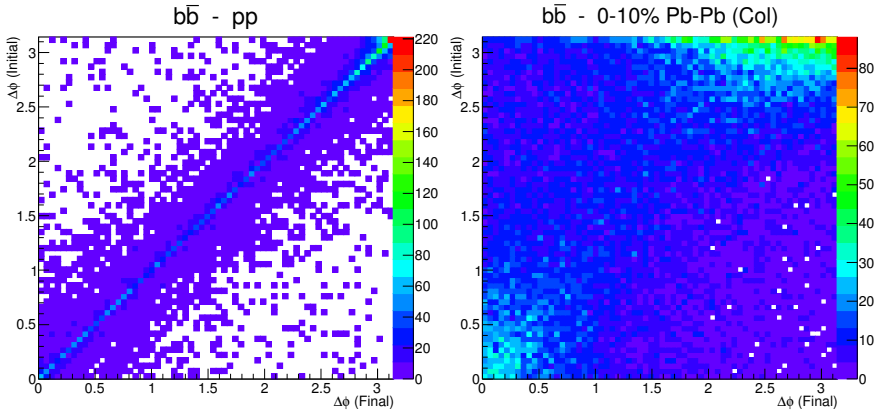

FIGURE 4.11: Final $\Delta\phi$ versus the initial $\Delta\phi$ for $b\bar{b}$ pairs in pp (left) and 0-10% collisional Pb-Pb (right) collisions.

4.4.2 Heavy-ion collisions

In this subsection, the results for the heavy-ion analysis into the different in-medium energy loss mechanisms in EPOS3+HQ are presented. There are seven samples at $\sqrt{s_{\mathrm{NN}}} = 5.02$ TeV, corresponding to pp, 50-70% Pb-Pb (col and col+rad), 30-50% Pb-Pb (col and col+rad) and 0-10% Pb-Pb (col and col+rad). The proton-proton results are presented in the previous subsection. We will purely focus on beauty correlations for the transverse momentum correlation, because there are too many charm quarks produced in heavy-ion collisions. Therefore, the initial correlation is too small to be visible over the combinatorial background (see left side of Figure A.4).

4.4.2.1 Azimuthal correlations

For this study, the differences between the initial and final stage of EPOS3+HQ are important. The results for the initial stage will be similar for both energy loss samples, where we expect to observe a significant difference in the transverse momentum correlations after in-medium interactions. These interactions will, however, also change the azimuthal angle distributions, which are needed to select the back-to-back pairs. In Figure 4.11, the initial $\Delta\phi(b, \bar{b})$ distribution versus the final one is shown for pp and most central Pb-Pb collisions. As expected, only a small difference is observed for proton-proton collisions. For central Pb-Pb collisions, the final distribution is much more smeared out, although still most of the pairs that are found back-to-back in the final state were also back-to-back created.

Figure 4.12 and 4.13 show the final $\Delta\phi$ distributions for beauty and charm quarks in the heavy-ion EPOS3+HQ samples. The left two plots show the pure signal, so pairs coming from the same vertex. The right two plots show the combinatorial background, so quarks coming from different vertices. We show the Pb-Pb samples separately for collisional and collisional+radiative energy loss mechanisms. The signal distributions show a similar trend as observed for proton-proton in the previous subsection. For beauty quarks a LO peak at $\Delta\phi = \pi$ is visible, where for charm the NLO contribution is dominant. For more central collisions, the so-called partonic wind effect start to play a role [98]. This is the phenomena that initial back-to-back correlations of quark pairs are pushed into the same direction (so towards smaller opening angles) due to the radial flow of the matter.

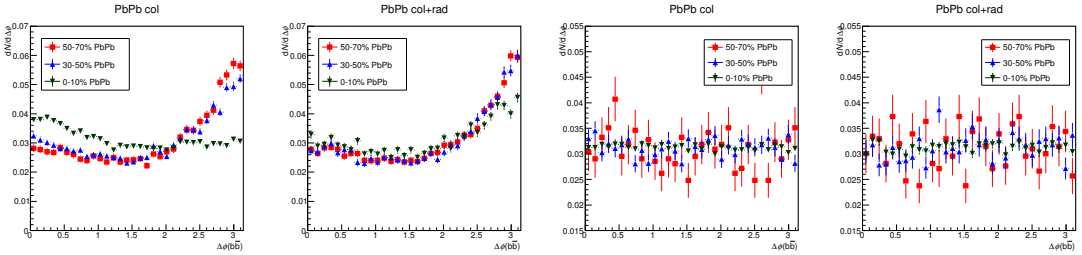

FIGURE 4.12: Final difference in azimuthal angle between two beauty quarks for the seven EPOS3+HQ samples. The two left plots show the pure signal, so quarks emerging from the same vertex. The two right plots show the combinatorial background. The distribution shown here are p_T integrated and normalised to one.

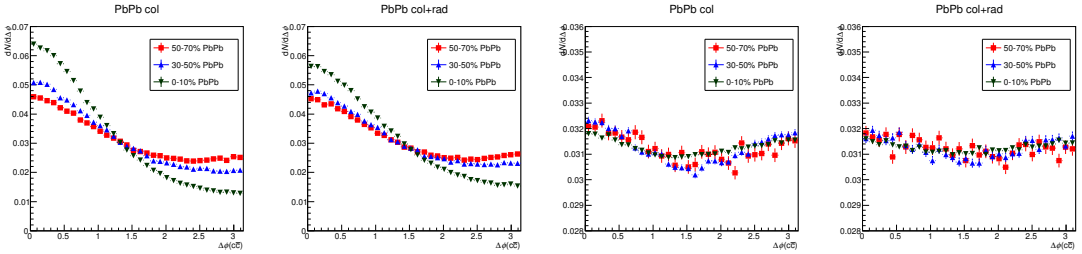

FIGURE 4.13: Final difference in azimuthal angle between two charm quarks for the seven EPOS3+HQ samples. The two left plots show the pure signal, so quarks emerging from the same vertex. The two right plots show the combinatorial background. The distribution shown here are p_T integrated and normalised to one.

As already noted in Ref. [55], this effect is stronger for purely collisional energy loss mechanisms. Due to the larger mass, the beauty quarks are less affected, although the partonic wind effect remains visible for the 0-10% Pb-Pb collisional sample.

In the figures with only combinatorial background, we see a flat distribution for beauty quarks, but a slight enhancement at $\Delta\phi = 0$ and π for charm. This cosine shape for non-related charm quarks is arising from the flow pattern. Again, the results are more pronounced for the collisional than for the collisional+radiative samples. As there are only a few $b\bar{b}$ pairs produced in heavy-ion collisions, the flat distribution for non-related beauty quarks is expected.

4.4.2.2 Transverse momentum correlations

The goal of this part of the analysis is to find significant differences between the collisional and collisional+radiative samples in the final distribution for our new proposed transverse momentum correlation observable. As one can imagine, central collisions will change the initial correlation more than peripheral collisions. Therefore, we have six samples, with central (0-10%), semi-central (30-50%) and peripheral (50-70%) collisions. In Appendix A, all twelve $b\bar{b}$ correlation projections can be found. In this subsection, the result for the 50-70% centrality class will be shown, as we expect the initial correlation here to survive the most. These projections are depicted in Figure 4.14.

The initial distributions of $C_R(p_\mathrm{T}, p_\mathrm{T}')$ in Pb-Pb collisions are similar as found in pp. The maximal value is a bit lower for the Pb-Pb projections, but this is expected as there is a higher combinatorial background from random pairs in these samples. So, initially a

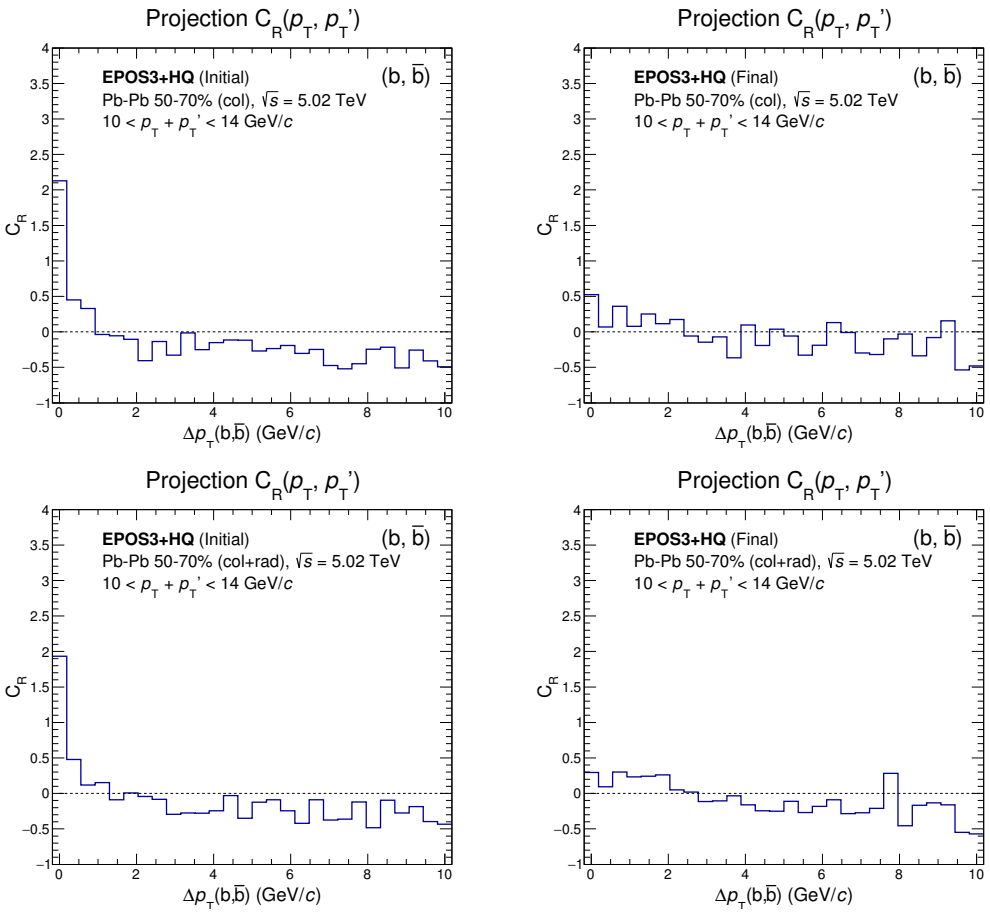

FIGURE 4.14: Projections of $C_R(p_T, p_T')$ for $b\bar{b}$ pairs for 50-70% Pb-Pb EPOS3+HQ collisions (both col and col+rad) in the p_T band: $10 < p_T + p_T' < 14$ GeV/c. Top: Collisional sample, initial (left) and final (right). Bottom: Collisional+radiative sample, initial (left) and final (right).

clear correlation between the transverse momenta of beauty quarks is observed. Where in pp collisions the initial correlation was decreased by a factor 2 (see Figure 4.8), for 50-70% Pb-Pb collisions a decrease of a factor 4 to 8 is found. The initial correlation is almost completely washed out due to the in-medium interactions. This is even more pronounced in central collisions, where a flat distribution is found for the 0-10% Pb-Pb sample (see Figures A.1 and A.2). So, for these relative low p_T samples, the two energy loss mechanisms can not be distinguished using our transverse momentum correlation observable. The meson-meson correlations are not shown in this thesis, because no improvement over the quark distributions is seen. The fragmentation of the beauty quarks introduces an additional smearing factor over the initial p_T-p_T' symmetry.

As said before, the largest transverse momentum correlation is expected for $b\bar{b}$ and B$\overline{\text{B}}$ pairs. An experimental problem with these beauty correlations is that they are relatively difficult to measure. Therefore, we also show the correlation for prompt D$\overline{\text{D}}$ mesons in semi-central collisions in Figure 4.15. Again, no significant deviation between both interaction mechanisms is observed. Another possibility is to study the (partly) leptonic correlations, so where one or both heavy-flavour mesons decay weakly. Because almost all high momentum electrons are coming from heavy-flavour decays, they can be used as triggers. Of course, part of the p_T correlation will be lost because of the other decay products of the B meson. In Figure 4.16, the e^-e^+ transverse momentum correlations

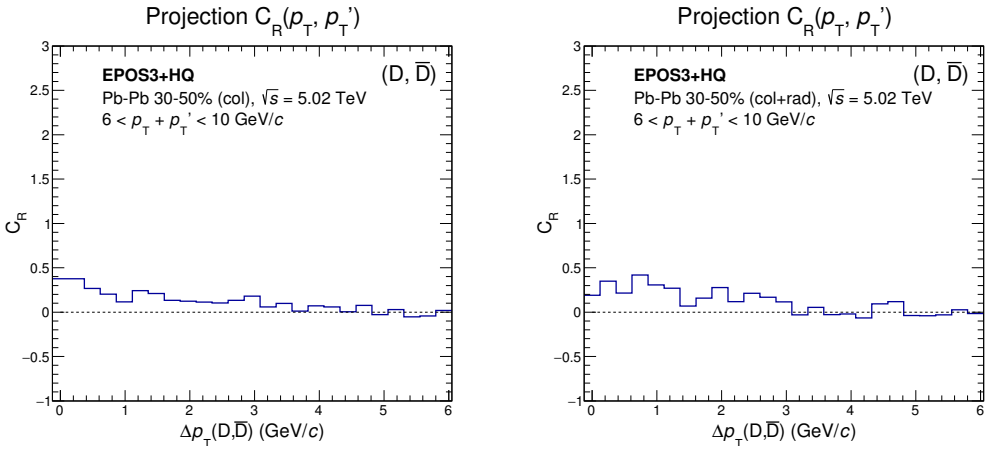

FIGURE 4.15: Projections of $C_R(p_\mathrm{T}, p_\mathrm{T}')$ for prompt D$\overline{\text{D}}$ pairs for 30-50% Pb-Pb EPOS3+HQ collisions in the p_T band: $6 < p_\mathrm{T} + p_\mathrm{T}' < 10$ GeV/c. The collisional sample is shown on the left, the collisional+radiative distribution on the right.

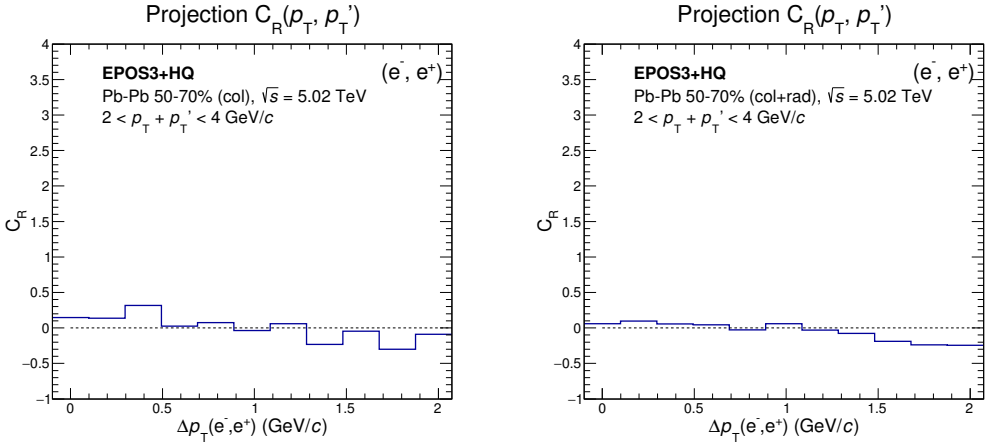

FIGURE 4.16: Projections of $C_R(p_\mathrm{T}, p_\mathrm{T}')$ for e^-e^+ pairs for 50-70% Pb-Pb EPOS3+HQ collisions in the p_T band: $2 < p_\mathrm{T} + p_\mathrm{T}' < 4$ GeV/c. The collisional sample is shown on the left, the collisional+radiative distribution on the right.

from two B mesons are shown for the 50-70% Pb-Pb collisional and collisional+radiative sample. Again, no significant deviation between both interaction mechanisms is found.

4.5 Discussion

Because this analysis is the first one using EPOS3+HQ, one can have doubts if all "teething problems" are solved. Only one year ago, one of the model authors still argued that it was not yet possible to reproduce experimental results for heavy quarks with this model [99]. However, a lot of work have been done during the last months and now a good description of charm and beauty meson production can be obtained with EPOS3+HQ. In Ref. [68], good comparisons with D meson results of ALICE have been presented. Besides this, it is already known for some time that EPOS describes the measurements in the light sector well.

Our proposed observable is extensively tested using three toy models. The mathematical definition is correct and the different trends are understood using the results of a strong and weakly correlation model. Nevertheless, it can still be the case that the observable is not sensitive enough, as we saw for the EPOS3+HQ Pb-Pb samples. To check whether this result is not model dependent, we will contact two other model builders (Prof. dr. Elena Bratkovskaya and Prof. dr. Steffen Bass) in the near future to look at the same observable. It could be the case that there is a correlation to be seen in real data, but that EPOS3+HQ overestimates the smearing of the initial correlation.

There is no doubt that a correlation survives in the proton-proton collisions, which will be sensitive to the final-state radiation process. While different models have different implementations of FSR, they try to make sure they do not fool themselves by calibrating their code. This is done for instance in e^-e^+ collisions by studying observables like the thrust or humped back plateau. If the initial calibration is already different, our conclusions at the two-body level can also just point to this.

For an outsider, it is hard to dig out what type of calibration is performed, but it is an important aspect of the comparison between different models. To check if a similar calibration in EPOS3+HQ and Pythia 6 is used, we studied the single particle spectra $\mathrm{d}N/\mathrm{d}p_\mathrm{T}$ for charm and anti-charm quarks. The results can be found in Figure 4.17 for EPOS3+HQ and Pythia 6. Two approaches for Pythia are shown, where LO $c\bar{c}$ corresponds to the strategy used in this thesis and LO+NLO $c\bar{c}$ to the default settings of Pythia. As we are not interested what happens at low p_T, where the EPOS3+HQ model and the Pythia 6 approaches are expected to differ, the distributions are normalised to the total number of simulated events. At large transverse momenta, where the LO $c\bar{c}$ production mechanisms will be dominant, a similar p_T distribution for charm quarks is found as compared to the total number of events.

One last important point to discuss is the fact that in the EPOS3+HQ model the assumption is made that a (small droplet of) quark-gluon plasma can also be produced in small systems. This is an effect of the universality of the model, meaning that pp, p-A and A-A collisions are treated in the same way. I agree that it is important to have an universal framework for the different collision systems and I also see the importance of studying properties of a possible produced QGP in pp collisions. However, this assumption is currently highly debated. In my opinion, it would be better to use the QGP like a flag that can be turned on and off depending on the analysis. In this way, one also has access to the properties of D mesons without in-medium interactions. Currently this is not possible in EPOS3+HQ.

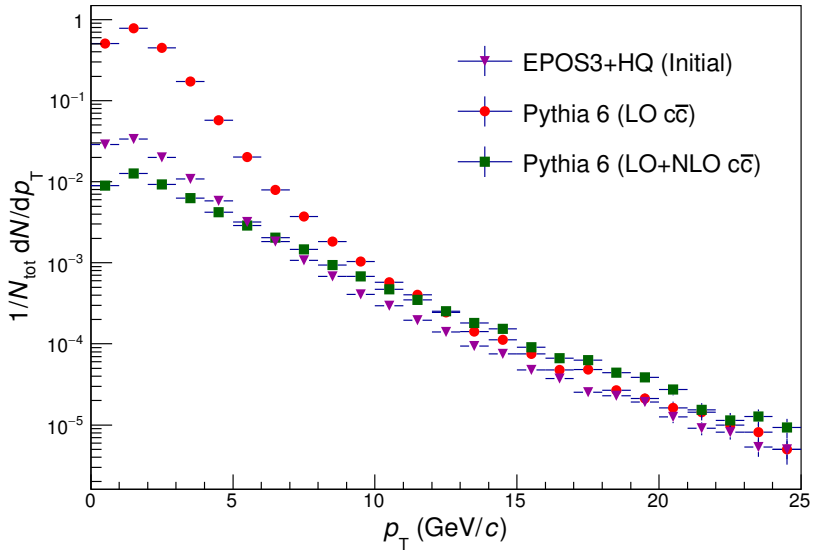

FIGURE 4.17: Single particle spectra, $\mathrm{d}N/\mathrm{d}p_{\mathrm{T}}$, for charm and anti-charm quark in EPOS3+HQ and both heavy-flavour production approaches for Pythia (LO and LO+NLO). The distributions are normalised to the number of simulated events.

Chapter 5

Conclusions and outlook

5.1 D^{*+}-meson cross-section

The production cross-section of the D^{*+} mesons was measured by the ALICE experiment in minimum-bias pp collisions at $\sqrt{s} = 5.02$ TeV in the transverse momentum range $1 \leq p_{\mathrm{T}} \leq 24$ GeV/c. The invariant mass method was applied to extract the D-meson signal. The final invariant cross-section agrees within errors with FONLL calculations, although the results are on the higher side of the theory curve. Cross-section ratios with the other D mesons (D^+ and D^0) agree with similar ratios for FONLL. In the D^{*+}-meson cross-section ratio with 7 TeV, a small shift downwards is observed in comparison with FONLL. After several checks, it was decided that this systematic trend is due to statistical fluctuations in both the 5 and 7 TeV cross-section measurements.

At the end of 2017, this measurement should be combined with the new proton-proton sample at $\sqrt{s} = 5.02$ TeV. This run is expected to last for three full weeks, so a lot more statistics is expected (rough estimate: factor 21days/5days ≈ 4 more statistics). This will result in smaller error bars (rough estimate: factor $\sqrt{N}/\sqrt{(1+4)N} = 1/\sqrt{5}$ smaller) and, hopefully, less statistical fluctuations. Before combining these samples, the measurement presented here should be redone with pass3 and the fix of the five runs in the MC sample. LHC15n pass3 includes the fix for the PID bug, of which the reconstruction of the first samples of LHC Run-2 suffered. So, a better particle identification performance is expected, which will lead to smaller background. Part of the MC simulation was redone because the technical details of the simulation of the TPC distortions had a negative effect on the matching efficiency, leading to a significant drop starting at $p_{\mathrm{T}} = 4$ GeV/c.

Additionally, an EMCal triggered cross-section measurement would be important. This is already performed for the D^{*+} meson at $\sqrt{s} = 8$ TeV and proofed to be useful in extending the p_{T} reach. This can be very helpful for the baseline for heavy-ion analyses, which normally have a larger p_{T} range. Finally, to further study the production cross-section of D mesons as a function of energy, the same analyses should be performed at $\sqrt{s} = 13$ and 14 TeV.

5.2 Heavy-flavour correlations

In the second part of this thesis, a new transverse momentum correlation observable is proposed as a sensitive probe to study the influence of final-state radiation on heavy-flavour quarks and differentiate between different in-medium energy loss models. Calculations using EPOS3+HQ and Pythia 6 were performed to study the effect of final-state radiation. In EPOS3+HQ, also the effect of a possible produced QGP has been taken into account. Finally, a centrality dependent study of the collisional and collisional+radiative energy loss models in EPOS3+HQ is performed. The proposed observable is extensively tested with three toy models. The mathematical definition is correct and the different trends are understood using toy models with strong and weakly correlation variables.

Our new observable shows that the initial symmetric $p_{\mathrm{T}} = p_{\mathrm{T}}{}'$ correlation in proton-proton collisions is not completely destroyed by the final-state radiation, neither for the final $\mathrm{D}\overline{\mathrm{D}}$ nor for the $c\bar{c}$ and $b\bar{b}$ before hadronisation. The absolute value of the C_R shows that we are in a region of "intermediate" correlated variables. We also saw that the shape of this correlation differs quite a lot between EPOS3+HQ and Pythia 6. For the latter model, the transverse momentum correlation after final-state radiation shows no enhancement at $\Delta p_{\mathrm{T}} = 0$. For larger Δp_{T} the distribution for Pythia 6 decreases faster than for EPOS3+HQ. This observation suggest to use this correlation to study the final state radiation of heavy quarks or, more explicitly, the dead-cone effect, which is only little known up to now by comparison between experiment and theory. The data, which will be collected in LHC Run-3 will open this opportunity.

The use of this same observable to differentiate between different in-medium energy loss mechanisms is limited. Different systems have been studied, but the correlation (which is clearly visible before interactions with the medium) did not survive. Even without taking the fragmentation of quarks into account, no difference could be observed between collisional and collisional+radiative samples. In the azimuthal correlation distributions for Pb-Pb EPOS3+HQ events, radial flow and the so-called partonic wind effect were visible.

As already noted in the discussion section, it is important to see what the behaviour of our new observable is in different models. Perhaps, EPOS3+HQ overestimates the energy loss of heavy quarks, and will there still be a correlation visible in experimental data.

The EPOS3+HQ samples studied in this analyses contained heavy quarks with relatively small transverse momenta. Extending the p_{T} ranges to higher values (e.g. larger than 40 GeV/c for B mesons, as measured in Ref. [75]) should be a logical next step. These high momenta heavy mesons are most likely to come from LO processes and should be easily detected in experiments. Up to now, it was time-wise not feasible to simulate high p_{T} heavy quarks in EPOS3+HQ, but an update is currently ongoing. When this is ready, both analyses should be redone for high momenta only.

Acknowledgements

Working on my master thesis for the past year in Utrecht and Nantes has been a real pleasure. Both projects were very interesting and I enjoyed my work. I would really like to thank everyone who helped me finish this thesis.

A big thanks to André Mischke and Alessandro Grelli, my supervisors at the Institute for Subatomic Physics at Utrecht University. Their help and support made it possible for me to complete this master's thesis. I also would like to thank André for helping to arrange my three-monthly internship in Nantes.

I'm also very grateful to my supervisors at Subatech in Nantes, Pol-Bernard Gossiaux and Jörg Aichelin. I really enjoyed my stay in France and would like to thank them for all their support (also outside the field of physics). Their knowledge and insight into the field of particle physics have been an inspiration and a big part of the reason I will continue in science.

Many other people helped me with my work, but I want especially want to thank Lennart van Doremalen, Mike Sas and David Fuseau who made both offices a lot more fun. Lastly, I would like to thank my girlfriend, friends and family for all the support they have given me.

Appendix A

Appendix A

The initial and final projections of the transverse momentum correlation for the six Pb-Pb EPOS3+HQ samples for all $b\bar{b}$ combinations that are back-to-back ($\Delta\phi > 3/4\pi$). In Figure A.4, the same distributions for $c\bar{c}$ in 50-70% Pb-Pb collisions are presented.

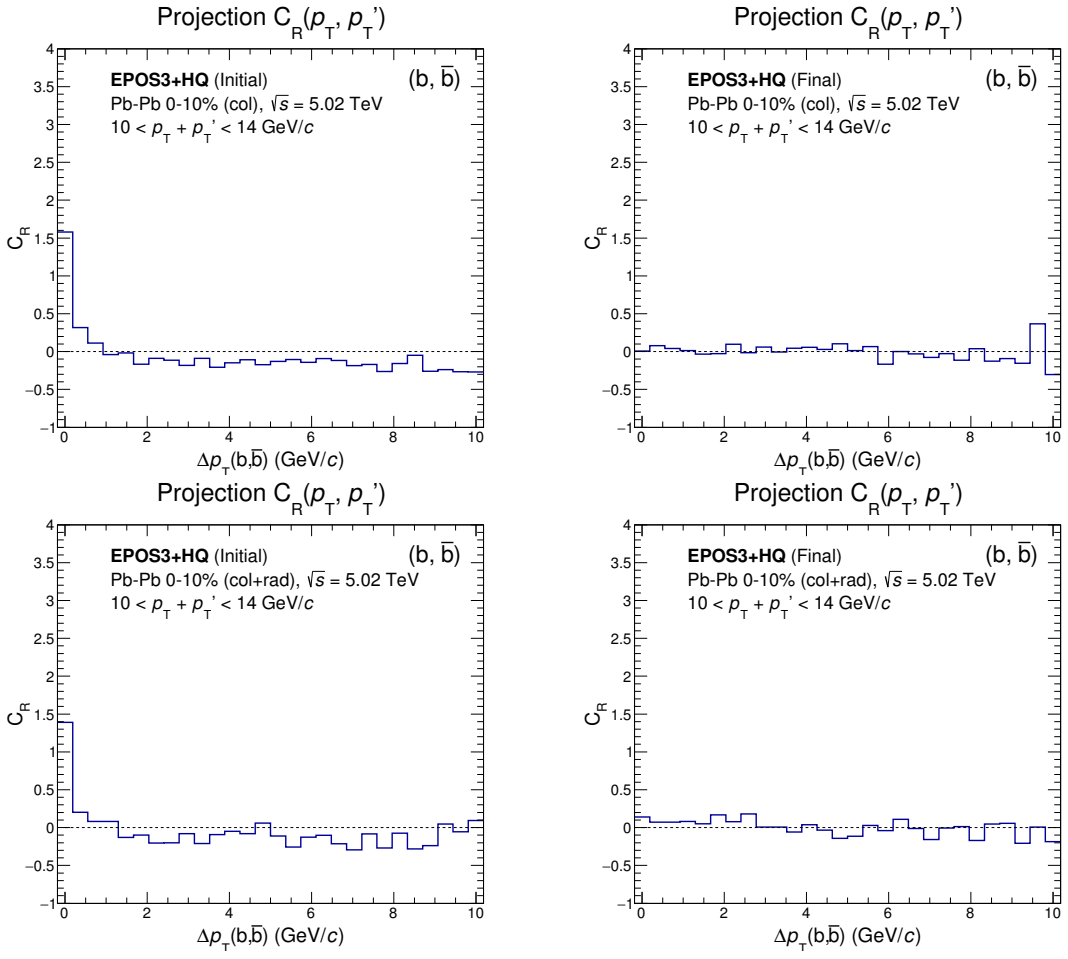

FIGURE A.1: Projections of $C_R(p_\mathrm{T}, p_\mathrm{T}')$ for $b\bar{b}$ pairs with $\Delta\phi > 3/4\pi$ for 0-10% Pb-Pb EPOS3+HQ collisions in the p_T band: $10 < p_\mathrm{T} + p_\mathrm{T}' < 14$ GeV/c. The purely collisional sample is shown in the top row and the collisional+radiative sample in the bottom row. The left plot shows the initial correlation and the right plot the final one.

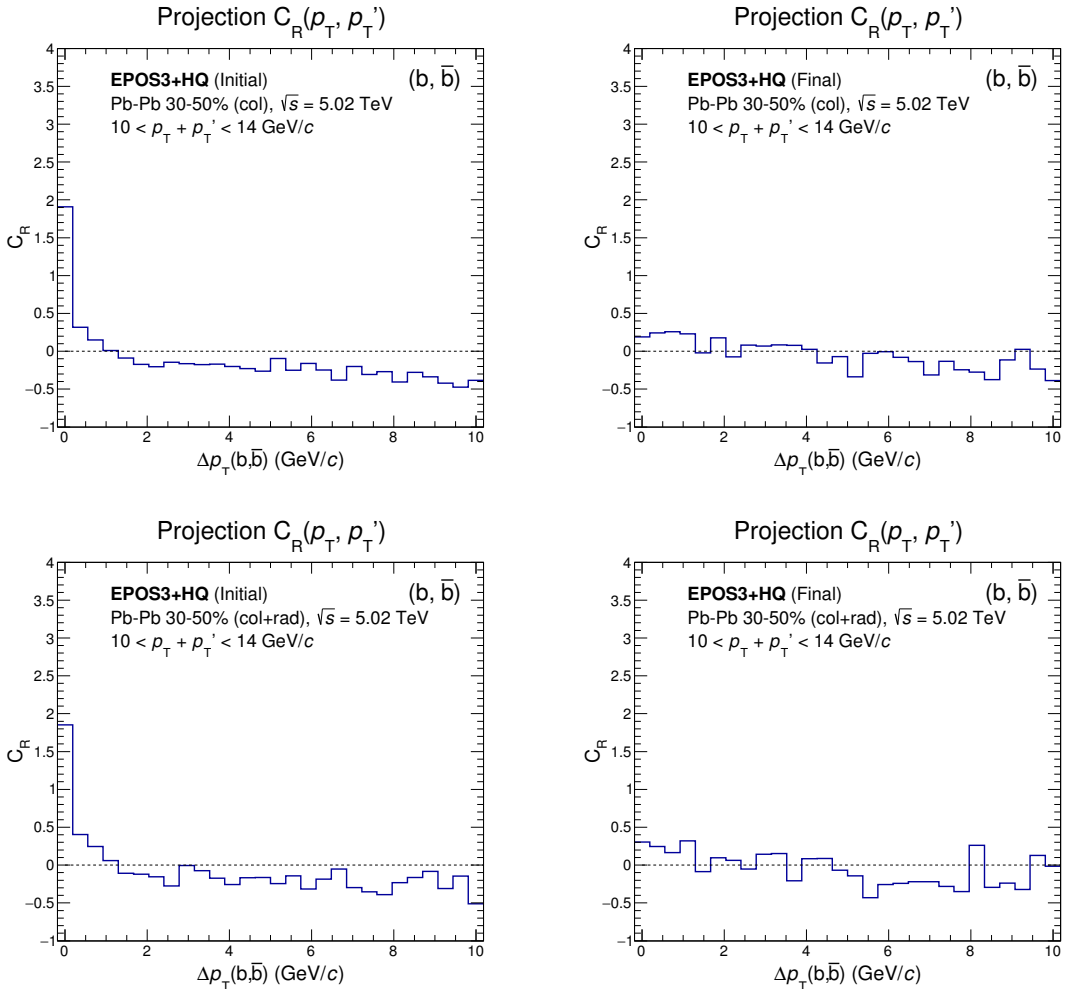

FIGURE A.2: Projections of $C_R(p_\mathrm{T}, p_\mathrm{T}')$ for $b\bar{b}$ pairs with $\Delta\phi > 3/4\pi$ for 30-50% Pb-Pb EPOS3+HQ collisions in the p_T band: $10 < p_\mathrm{T} + p_\mathrm{T}' < 14$ GeV/c. The purely collisional sample is shown in the top row and the collisional+radiative sample in the bottom row. The left plot shows the initial correlation and the right plot the final one.

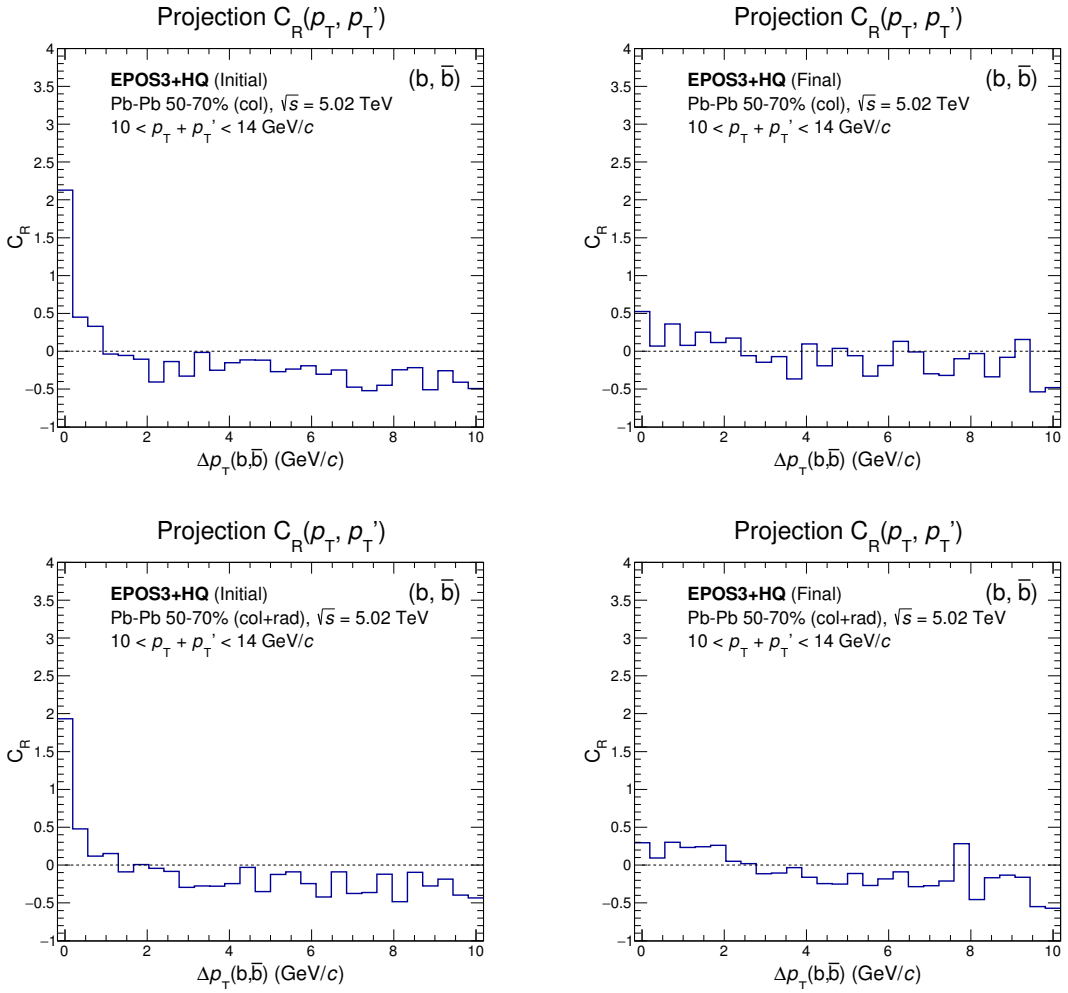

FIGURE A.3: Projections of $C_R(p_\mathrm{T}, p_\mathrm{T}')$ for $b\bar{b}$ pairs with $\Delta\phi > 3/4\pi$ for 50-70% Pb-Pb EPOS3+HQ collisions in the p_T band: $10 < p_\mathrm{T} + p_\mathrm{T}' < 14$ GeV/c. The purely collisional sample is shown in the top row and the collisional+radiative sample in the bottom row. The left plot shows the initial correlation and the right plot the final one.

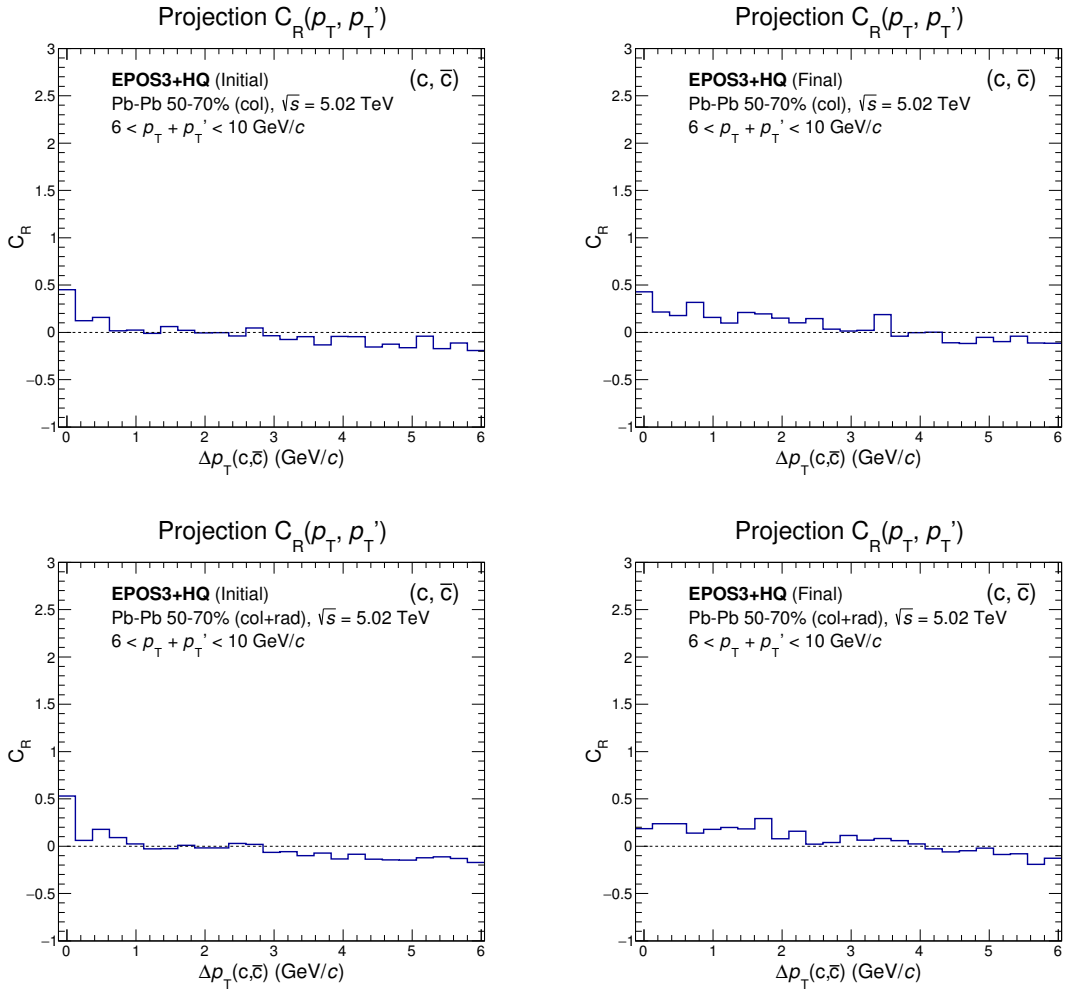

FIGURE A.4: Projections of $C_R(p_\mathrm{T}, p_\mathrm{T}')$ for $c\bar{c}$ pairs with $\Delta\phi > 3/4\pi$ for 50-70% Pb-Pb EPOS3+HQ collisions in the p_T band: $6 < p_\mathrm{T} + p_\mathrm{T}' < 10$ GeV/c. The purely collisional sample is shown in the top row and the collisional+radiative sample in the bottom row. The left plot shows the initial correlation and the right plot the final one.

Bibliography

[1] CMS Collaboration, S. Chatrchyan *et al.*, Phys. Lett. **B716**, 30 (2012), doi: 10.1016/j.physletb.2012.08.021, arXiv: 1207.7235 [hep-ex].

[2] ATLAS Collaboration, G. Aad *et al.*, Phys. Lett. **B716**, 1 (2012), doi: 10.1016/j.physletb.2012.08.020, arXiv: 1207.7214 [hep-ex].

[3] H. Fritzsch, M. Gell-Mann, and H. Leutwyler, Phys. Lett. **47B**, 365 (1973), doi: 10.1016/0370-2693(73)90625-4.

[4] M. E. Peskin and D. V. Schroeder, *An Introduction to Quantum Field Theory* (Westview Press, 1995).

[5] PDG, C. Patrignani *et al.*, Chin. Phys. **C40**, 100001 (2016), doi: 10.1088/1674-1137/40/10/100001.

[6] M. Cacciari, M. Greco, and P. Nason, JHEP **05**, 007 (1998), doi: 10.1088/1126-6708/1998/05/007, arXiv: hep-ph/9803400.

[7] FONLL Heavy Quark Production, URL `http://www.lpthe.jussieu.fr/cacciari/fonll/fonllform.html`, Accessed: 2017-07-02.

[8] B. A. Kniehl *et al.*, Eur. Phys. J. **C41**, 199 (2005), doi: 10.1140/epjc/s2005-02200-7, arXiv: hep-ph/0502194.

[9] B. A. Kniehl *et al.*, Eur. Phys. J. **C72**, 2082 (2012), doi: 10.1140/epjc/s10052-012-2082-2, arXiv: 1202.0439 [hep-ph].

[10] CMS Collaboration, S. Chatrchyan *et al.*, Phys. Lett. **B718**, 795 (2013), doi: 10.1016/j.physletb.2012.11.025, arXiv: 1210.5482 [nucl-ex].

[11] ALICE Collaboration, J. Adam *et al.*, Nature Phys. **13**, 535 (2017), doi: 10.1038/nphys4111, arXiv: 1606.07424 [nucl-ex].

[12] CMS Collaboration, V. Khachatryan *et al.*, Phys. Lett. **B765**, 193 (2017), doi: 10.1016/j.physletb.2016.12.009, arXiv: 1606.06198 [nucl-ex].

[13] S. Mukherjee, Quantum Chromodynamics Phase Diagram, URL `https://deixismagazine.org/2016/06/early-universe-soup/dol_plasma/`, Accessed: 2017-07-08.

[14] T. Bhattacharya *et al.*, Phys. Rev. Lett. **113**, 082001 (2014), doi: 10.1103/PhysRevLett.113.082001, arXiv: 1402.5175 [hep-lat].

[15] X. Zhu *et al.*, Phys. Lett. **B647**, 366 (2007), doi: 10.1016/j.physletb.2007.01.072, arXiv: hep-ph/0604178.

[16] ALICE Collaboration, J. Adam *et al.*, JHEP **03**, 081 (2016), doi: 10.1007/JHEP03(2016)081, arXiv: 1509.06888 [nucl-ex].

[17] CMS Collaboration, A. M. Sirunyan *et al.*, Submitted to Phys. Rev. Lett. (2017), arXiv: 1705.04727 [hep-ex].

[18] J. W. Cronin *et al.*, Phys. Rev. **D11**, 3105 (1975), doi: 10.1103/PhysRevD.11.3105.

[19] ALICE Collaboration, B. Abelev *et al.*, Phys. Rev. Lett. **111**, 102301 (2013), doi: 10.1103/PhysRevLett.111.102301, arXiv: 1305.2707 [nucl-ex].

[20] A. Andronic *et al.*, Eur. Phys. J. **C76**, 107 (2016), doi: 10.1140/epjc/s10052-015-3819-5, arXiv: 1506.03981 [nucl-ex].

[21] ALICE Collaboration, B. Abelev *et al.*, J. Phys. **G41**, 087002 (2014), doi: 10.1088/0954-3899/41/8/087002.

[22] J. Nash and A. Ball, CMS Collaboration, Report No. CERN-LHCC-2011-006, LHCC-P-004, 2011 (unpublished), URL `https://cds.cern.ch/record/1355706`.

[23] G. Aarts *et al.*, Eur. Phys. J. **A53**, 93 (2017), doi: 10.1140/epja/i2017-12282-9, arXiv: 1612.08032 [nucl-th].

[24] G. Tsiledakis and K. Schweda, $D\overline{D}$ momentum correlations versus relative azimuth as a sensitive probe for thermalization, in *Proceedings, 38th International Symposium on Multiparticle Dynamics (ISMD 2008): Hamburg, Germany, September 15-20, 2008*, pp. 217–221, 2009, doi: 10.3204/DESY-PROC-2009-01/80, arXiv: 0901.4296 [nucl-ex].

[25] P. B. Gossiaux, Consequence of absorptive plasma on heavy quark energy loss and jet evolution in ultra-relativistic heavy ion collisions, in *The 30th Winter Workshop on Nuclear Dynamics*, 2014, URL `https://indico.cern.ch/event/275088/contributions/1616825/`.

[26] R. Hambrock and W. A. Horowitz, AdS/CFT predictions for azimuthal and momentum correlations of $b\bar{b}$ pairs in heavy ion collisions, in *8th International Conference on Hard and Electromagnetic Probes of High-energy Nuclear Collisions: Hard Probes 2016 (HP2016) Wuhan, Hubei, China, September 23-27, 2016*, 2017, arXiv: 1703.05845 [hep-ph].

[27] CMS Collaboration, V. Khachatryan *et al.*, JHEP **03**, 136 (2011), doi: 10.1007/JHEP03(2011)136, arXiv: 1102.3194 [hep-ex].

[28] ALICE Collaboration, K. Aamodt *et al.*, JINST **3**, S08002 (2008), doi: 10.1088/1748-0221/3/08/S08002.

[29] A. Tauro, ALICE Collaboration, Report No. ALICE-PHO-SKE-2017-001, 2017 (unpublished), URL `http://cds.cern.ch/record/2263642`.

[30] J. Alme *et al.*, Nucl. Instrum. Meth. **A622**, 316 (2010), doi: 10.1016/j.nima.2010.04.042, arXiv: 1001.1950 [physics.ins-det].

[31] J. Adam *et al.*, ALICE Collaboration, Report No. ALICE-PUBLIC-2015-004, 2015 (unpublished), URL `https://cds.cern.ch/record/2047855`.

[32] I. Antcheva *et al.*, Comput. Phys. Commun. **180**, 2499 (2009), doi: 10.1016/j.cpc.2009.08.005, arXiv: 1508.07749 [physics.data-an].

[33] GEANT, S. Agostinelli *et al.*, Nucl. Instrum. Meth. **A506**, 250 (2003), doi: 10.1016/S0168-9002(03)01368-8.

[34] T. Sjostrand, S. Mrenna, and P. Z. Skands, JHEP **05**, 026 (2006), doi: 10.1088/1126-6708/2006/05/026, arXiv: hep-ph/0603175.

[35] P. Z. Skands, Phys. Rev. **D82**, 074018 (2010), doi: 10.1103/PhysRevD.82.074018, arXiv: 1005.3457 [hep-ph].

[36] L. Vermunt *et al.*, ALICE Collaboration, Report No. ALICE-ANA-2017-3514, 2017 (unpublished), URL `https://aliceinfo.cern.ch/Notes/node/584`.

[37] R. Bala and M. Sharma, QA analysis for MC pp @ 5 TeV in *PWG-HF Physics Analysis Group D2H Meeting, November 25, 2016*, URL `https://indico.cern.ch/event/581288/`.

[38] R. Bala *et al.*, ALICE Collaboration, Report No. ALICE-ANA-2016-3104, 2016 (unpublished), URL `https://aliceinfo.cern.ch/Notes/node/493`.

[39] ALICE Collaboration, B. Abelev *et al.*, JHEP **07**, 191 (2012), doi: 10.1007/JHEP07(2012)191, arXiv: 1205.4007 [hep-ex].

[40] ALICE Collaboration, B. Abelev *et al.*, JHEP **01**, 128 (2012), doi: 10.1007/JHEP01(2012)128, arXiv: 1111.1553 [hep-ex].

[41] LHCb Collaboration, R. Aaij *et al.*, JHEP **08**, 117 (2013), doi: 10.1007/JHEP08(2013)117, arXiv: 1306.3663 [hep-ex].

[42] CMS Collaboration, S. Chatrchyan *et al.*, Phys. Rev. **D84**, 052008 (2011), doi: 10.1103/PhysRevD.84.052008, arXiv: 1106.4048 [hep-ex].

[43] J. Adam *et al.*, ALICE Collaboration, Report No. ALICE-PUBLIC-2016-005, 2016 (unpublished), URL `https://cds.cern.ch/record/2202638`.

[44] A. Barbano *et al.*, ALICE Collaboration, Report No. ALICE-ANA-2016-3352, 2016 (unpublished), URL `https://aliceinfo.cern.ch/Notes/node/537`.

[45] M. Cacciari, M. L. Mangano, and P. Nason, Eur. Phys. J. **C75**, 610 (2015), doi: 10.1140/epjc/s10052-015-3814-x, arXiv: 1507.06197 [hep-ph].

[46] L. Gladilin, Eur. Phys. J. **C75**, 19 (2015), doi: 10.1140/epjc/s10052-014-3250-3, arXiv: 1404.3888 [hep-ex].

[47] CMS Collaboration, Report No. CMS-PAS-HIN-16-001, 2016 (unpublished), URL `http://inspirehep.net/record/1467157`.

[48] ATLAS Collaboration, G. Aad *et al.*, Nucl. Phys. **B907**, 717 (2016), doi: 10.1016/j.nuclphysb.2016.04.032, arXiv: 1512.02913 [hep-ex].

[49] LHCb Collaboration, R. Aaij *et al.*, JHEP **03**, 159 (2016), doi: 10.1007/JHEP03(2016)159,10.1007/JHEP09(2016)013,10.1007/JHEP05(2017)074, arXiv: 1510.01707 [hep-ex].

[50] M. L. Mangano, P. Nason, and G. Ridolfi, Nucl. Phys. **B373**, 295 (1992), doi: 10.1016/0550-3213(92)90435-E.

[51] ALICE Collaboration, J. Adam *et al.*, Phys. Rev. **C94**, 054908 (2016), doi: 10.1103/PhysRevC.94.054908, arXiv: 1605.07569 [nucl-ex].

[52] ALICE Collaboration, B. Abelev *et al.*, Phys. Lett. **B719**, 29 (2013), doi: 10.1016/j.physletb.2013.01.012, arXiv: 1212.2001 [nucl-ex].

[53] ALICE Collaboration, J. Adam *et al.*, Eur. Phys. J. **C77**, 245 (2017), doi: 10.1140/epjc/s10052-017-4779-8, arXiv: 1605.06963 [nucl-ex].

[54] P. B. Gossiaux *et al.*, Global view on coupled dynamics of heavy and light flavor observables from EPOSHQ, in *26th International Conference on Ultrarelativistic Nucleus-Nucleus Collisions (Quark Matter 2017) Chicago, Illinois, USA, February 6-11, 2017*, 2017, arXiv: 1705.02271 [hep-ph].

[55] M. Nahrgang *et al.*, Phys. Rev. **C90**, 024907 (2014), doi: 10.1103/PhysRevC.90.024907, arXiv: 1305.3823 [hep-ph].

[56] T. Sjstrand *et al.*, Comput. Phys. Commun. **191**, 159 (2015), doi: 10.1016/j.cpc.2015.01.024, arXiv: 1410.3012 [hep-ph].

[57] K. Werner *et al.*, Phys. Rev. **C82**, 044904 (2010), doi: 10.1103/PhysRevC.82.044904, arXiv: 1004.0805 [nucl-th].

[58] K. Werner *et al.*, Phys. Rev. **C85**, 064907 (2012), doi: 10.1103/PhysRevC.85.064907, arXiv: 1203.5704 [nucl-th].

[59] P. B. Gossiaux and J. Aichelin, Phys. Rev. **C78**, 014904 (2008), doi: 10.1103/PhysRevC.78.014904, arXiv: 0802.2525 [hep-ph].

[60] H. J. Drescher *et al.*, Phys. Rept. **350**, 93 (2001), doi: 10.1016/S0370-1573(00)00122-8, arXiv: hep-ph/0007198.

[61] K. Werner, Phys. Rev. Lett. **98**, 152301 (2007), doi: 10.1103/PhysRevLett.98.152301, arXiv: 0704.1270 [nucl-th].

[62] K. Werner *et al.*, Phys. Rev. **C89**, 064903 (2014), doi: 10.1103/PhysRevC.89.064903, arXiv: 1312.1233 [nucl-th].

[63] I. Karpenko, P. Huovinen, and M. Bleicher, Comput. Phys. Commun. **185**, 3016 (2014), doi: 10.1016/j.cpc.2014.07.010, arXiv: 1312.4160 [nucl-th].

[64] S. Borsanyi *et al.*, JHEP **11**, 077 (2010), doi: 10.1007/JHEP11(2010)077, arXiv: 1007.2580 [hep-lat].

[65] K. Werner *et al.*, Phys. Rev. **C83**, 044915 (2011), doi: 10.1103/PhysRevC.83.044915, arXiv: 1010.0400 [nucl-th].

[66] M. Bleicher *et al.*, J. Phys. **G25**, 1859 (1999), doi: 10.1088/0954-3899/25/9/308, arXiv: hep-ph/9909407.

[67] H. Petersen *et al.*, Phys. Rev. **C78**, 044901 (2008), doi: 10.1103/PhysRevC.78.044901, arXiv: 0806.1695 [nucl-th].

[68] B. Guiot, *Production de charms et de photons prompts avec le générateur dévénement EPOS*, PhD thesis, University of Nantes, 2014.

[69] A. Donnachie and P. V. Landshoff, Phys. Lett. **B296**, 227 (1992), doi: 10.1016/0370-2693(92)90832-O, arXiv: hep-ph/9209205.

[70] G. A. Schuler and T. Sjostrand, Nucl. Phys. **B407**, 539 (1993), doi: 10.1016/0550-3213(93)90091-3.

[71] G. A. Schuler and T. Sjostrand, Phys. Rev. **D49**, 2257 (1994), doi: 10.1103/PhysRevD.49.2257.

[72] B. Andersson *et al.*, Phys. Rept. **97**, 31 (1983), doi: 10.1016/0370-1573(83)90080-7.

[73] CDF Collaboration, D. Acosta *et al.*, Phys. Rev. **D71**, 092001 (2005), doi: 10.1103/PhysRevD.71.092001, arXiv: hep-ex/0412006.

[74] CMS Collaboration, V. Khachatryan *et al.*, JHEP **03**, 136 (2011), doi: 10.1007/JHEP03(2011)136, arXiv: 1102.3194 [hep-ex].

[75] CMS Collaboration, Report No. CMS-PAS-HIN-16-005, 2016 (unpublished), URL `http://cds.cern.ch/record/2202805`.

[76] V. N. Gribov and L. N. Lipatov, Sov. J. Nucl. Phys. **15**, 438 (1972), [Yad. Fiz.15,781(1972)].

[77] G. Altarelli and G. Parisi, Nucl. Phys. **B126**, 298 (1977), doi: 10.1016/0550-3213(77)90384-4.

[78] Y. L. Dokshitzer, Sov. Phys. JETP **46**, 641 (1977), [Zh. Eksp. Teor. Fiz.73,1216(1977)].

[79] M. Rohrmoser, *Study of correlations of heavy quarks in heavy ion collisions and their role in understanding the mechanisms of energy loss in the quark gluon plasma*, PhD thesis, Bretagne Loire University, 2017.

[80] L. D. Landau and I. Pomeranchuk, Dokl. Akad. Nauk Ser. Fiz. **92**, 535 (1953).

[81] A. B. Migdal, Phys. Rev. **103**, 1811 (1956), doi: 10.1103/PhysRev.103.1811.

[82] J. D. Bjorken, Fermilab, Report No. FERMILAB-PUB-82-059-THY, FERMILAB-PUB-82-059-T, 1982 (unpublished), URL `inspirehep.net/record/181746`.

[83] E. Braaten and M. H. Thoma, Phys. Rev. **D44**, 1298 (1991), doi: 10.1103/PhysRevD.44.1298.

[84] A. Peshier, Phys. Rev. Lett. **97**, 212301 (2006), doi: 10.1103/PhysRevLett.97.212301, arXiv: hep-ph/0605294.

[85] M. Gyulassy and X.-N. Wang, Nucl. Phys. **B420**, 583 (1994), doi: 10.1016/0550-3213(94)90079-5, arXiv: nucl-th/9306003.

[86] X.-N. Wang, M. Gyulassy, and M. Plumer, Phys. Rev. **D51**, 3436 (1995), doi: 10.1103/PhysRevD.51.3436, arXiv: hep-ph/9408344.

[87] Y. L. Dokshitzer and D. E. Kharzeev, Phys. Lett. **B519**, 199 (2001), doi: 10.1016/S0370-2693(01)01130-3, arXiv: hep-ph/0106202.

[88] R. Abir *et al.*, Phys. Lett. **B715**, 183 (2012), doi: 10.1016/j.physletb.2012.07.044, arXiv: 1203.5221 [hep-ph].

[89] P. B. Gossiaux *et al.*, J. Phys. **G37**, 094019 (2010), doi: 10.1088/0954-3899/37/9/094019, arXiv: 1001.4166 [hep-ph].

[90] W. A. Horowitz and M. Gyulassy, Phys. Lett. **B666**, 320 (2008), doi: 10.1016/j.physletb.2008.04.065, arXiv: 0706.2336 [nucl-th].

[91] S. Cao, G.-Y. Qin, and S. A. Bass, Phys. Rev. **C88**, 044907 (2013), doi: 10.1103/PhysRevC.88.044907, arXiv: 1308.0617 [nucl-th].

[92] M. Djordjevic and M. Gyulassy, Nucl. Phys. **A733**, 265 (2004), doi: 10.1016/j.nuclphysa.2003.12.020, arXiv: nucl-th/0310076.

[93] B. G. Zakharov, JETP Lett. **80**, 617 (2004), doi: 10.1134/1.1857266, arXiv: hep-ph/0410321, [Pisma Zh. Eksp. Teor. Fiz.80,721(2004)].

[94] J. Aichelin, P. B. Gossiaux, and T. Gousset, Phys. Rev. **D89**, 074018 (2014), doi: 10.1103/PhysRevD.89.074018, arXiv: 1307.5270 [hep-ph].

[95] J. F. Gunion and G. Bertsch, Phys. Rev. **D25**, 746 (1982), doi: 10.1103/PhysRevD.25.746.

[96] BaBar Collaboration, B. Aubert *et al.*, Phys. Rev. **D67**, 031101 (2003), doi: 10.1103/PhysRevD.67.031101, arXiv: hep-ex/0208018.

[97] C. Peterson *et al.*, Phys. Rev. **D27**, 105 (1983), doi: 10.1103/PhysRevD.27.105.

[98] X. Zhu, N. Xu, and P. Zhuang, Phys. Rev. Lett. **100**, 152301 (2008), doi: 10.1103/PhysRevLett.100.152301, arXiv: 0709.0157 [nucl-th].

[99] B.-P. Gossiaux and R. Katz, Dynamical bottomonium-suppression in a realistic AA background, in *Proceedings, 16th International Conference on Strangeness in Quark Matter (SQM 2016): Berkeley, California, United States* Vol. 779, p. 012041, 2017, doi: 10.1088/1742-6596/779/1/012041, arXiv: 1611.06499 [hep-ph].